



# Strain engineering and mechanical assembly of silicon/germanium nanomembranes

Qinglei Guo<sup>a,d</sup>, Zengfeng Di<sup>b,\*</sup>, Max G. Lagally<sup>c,\*</sup>, Yongfeng Mei<sup>a,\*</sup>

<sup>a</sup> Department of Materials Science, State Key Laboratory of ASIC and Systems, Fudan University, Shanghai, 200433, People's Republic of China

<sup>b</sup> State Key Laboratory of Functional Materials for Informatics, Shanghai Institute of Microsystem and Information Technology, Chinese Academy of Sciences, Shanghai, 200050, People's Republic of China

<sup>c</sup> Department of Materials Science and Engineering, University of Wisconsin-Madison, Madison, WI, 53706, United States

<sup>d</sup> Department of Materials Science and Engineering, Frederick Seitz Materials Research Laboratory, University of Illinois at Urbana-Champaign, Urbana, IL, 61801, United States

## ARTICLE INFO

### Article history:

Received 12 December 2017

Received in revised form 3 February 2018

Accepted 15 February 2018

Available online xxx

### Keywords:

Silicon/germanium nanomembranes

Strain engineering

Mechanical assembly

Micro/nano-architectures

## ABSTRACT

Silicon (Si) and/or germanium (Ge) nanomembranes (NMs) play crucial roles in various applications, including conventional microelectronics, as well as recently emerging high-performance flexible/stretchable electronics. Because of their superior mechanical properties, such as flexibility, strain-ability, and bond-ability, Si/GeNMs can be strain-engineered, functionalized, and assembled into two/three-dimensional (2D/3D) micro/nano-architectures and devices. These features offer significant opportunities in nanoscience and for the development of nanotechnology. Strain engineering of semiconductor NMs enables the modification of their physical properties, in particular those of Si and Ge (e.g., carrier mobility, band structure), thus creating enormous potential for use in high-speed rigid/flexible electronics, optoelectronics, and nanophotonics. The mechanical properties of NMs allow large deformations at the micro/nano-scale, via self-assembly or guided self-assembly, leading to 3D micro/nano-architectures, including tubes, wrinkles, buckles, and mesostructures. The transformation from 2D planar NMs to 3D micro/nano-architectures again strongly influences physical properties (e.g., mechanics, optics, and electronics), providing fascinating applications in sensing, energy harvesting, bio-integration, and flexible/stretchable electronics. In this Review, the recent progress in strain engineering and mechanical assembly of Si/GeNMs is reviewed, ranging from fundamental principles to device applications.

© 2018 Elsevier B.V. All rights reserved.

## Contents

1. Introduction	3
2. Properties of Si/GeNMs	4
2.1. Energy band structures	4
2.2. Electrical conductivity	4
2.3. Opto electronic properties	5
2.4. Thermal conductivities and thermoelectric properties	5
2.5. Mechanical properties	8
3. Strategies to synthesize and assemble Si and GeNMs	8
3.1. Synthesis methods	8
3.2. Assembly approaches	9
4. Strain engineering of Si/GeNMs	11
4.1. Strain engineering of 2D Si/GeNMs	11

\* Corresponding authors.

E-mail addresses: [zfdi@mail.sim.ac.cn](mailto:zfdi@mail.sim.ac.cn) (Z. Di), [lagally@engr.wisc.edu](mailto:lagally@engr.wisc.edu) (M.G. Lagally), [yfm@fudan.edu.cn](mailto:yfm@fudan.edu.cn) (Y. Mei).

<https://doi.org/10.1016/j.mser.2018.02.002>

0927-796X/© 2018 Elsevier B.V. All rights reserved.

4.2.	Strained-Si technology	11
4.3.	Tensilely strained Ge	12
4.3.1.	Energy band structures <i>versus</i> strain	12
4.3.2.	Optoelectronic applications	12
5.	3D assembly by strain engineering	14
5.1.	Rolled-up nanotechnology	14
5.2.	Wrinkled-up nanotechnology	16
5.3.	Principles of rolling or wrinkling?	16
5.4.	Compressive Wrinkling/Buckling	17
5.5.	Popped-up mesostructures	18
6.	Properties and applications for 3D strain-engineered Si/GeNMs	19
6.1.	Properties	19
6.2.	Applications	21
6.2.1.	Sensors and transducers	22
6.2.2.	Micro/nanorobotics	22
6.2.3.	Bio-Platforms	23
6.2.4.	Optoelectronic devices	23
6.2.5.	Energy harvesting	24
6.2.6.	Flexible electronics: from bendable to stretchable, twistable, and foldable	25
7.	Summary and outlook	26
	Acknowledgements	27
	References	27

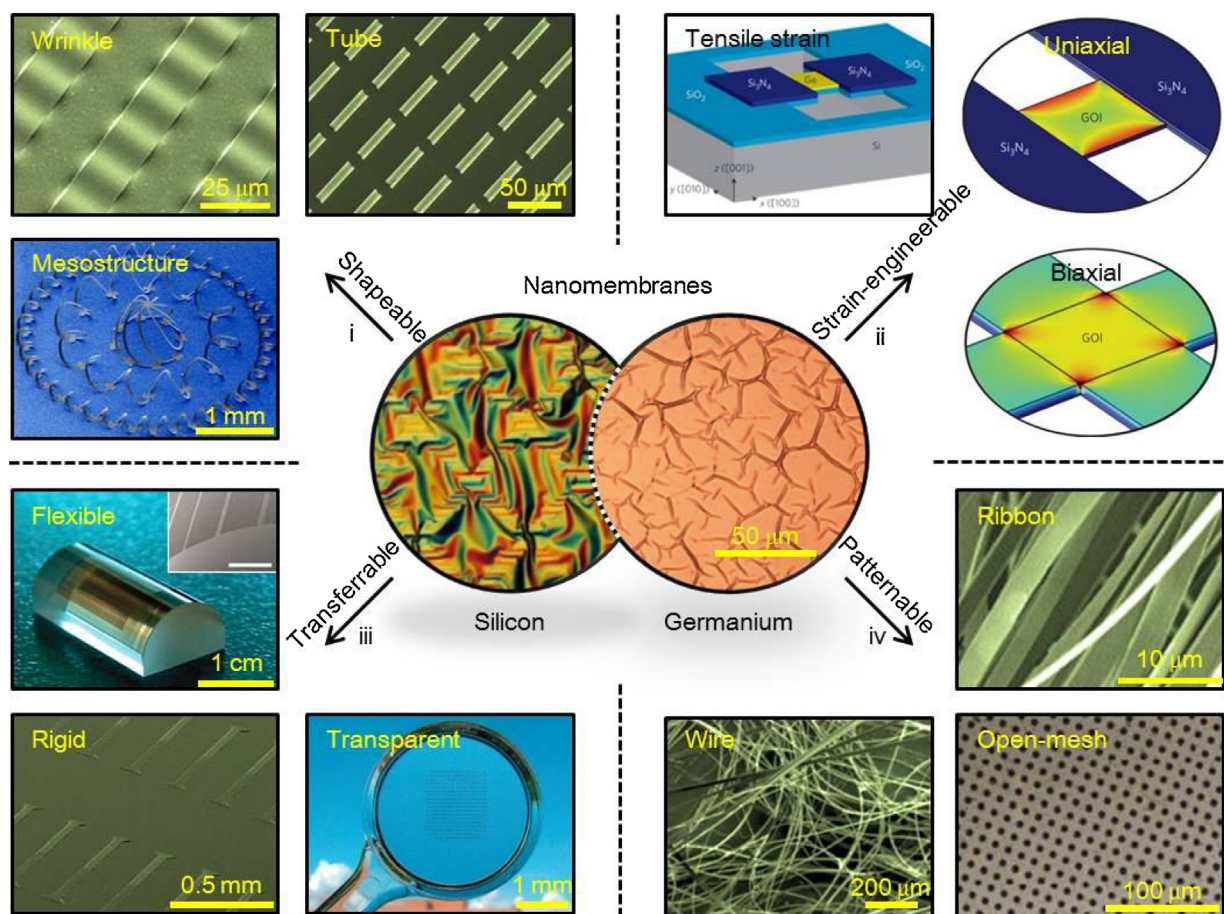


**Fig. 1.** Main features of single-crystalline Si/GeNMs: (i) shapeable: geometry transformation from 2D planar NMs to 3D micro/nano-architectures, including wrinkles/buckles [15], rolled-up tubes/helices [13], and pop-up origami mesostructures [14]; (ii) strain engineerable: tuning the physical properties of Si/GeNMs under tensile uniaxial or biaxial strain for enhanced charge-carrier mobility of Si [12,19,22,23], or energy-band engineering of Ge [20,21]; (iii) transferrable: integration onto either flexible or rigid (including transparent) substrate [18], depending on intended application; a demonstration of a SiNM-based array on a double-convex polycarbonate magnifying glass [18], which demonstrates potential for applications in transparent electronics; (iv) patternable: Si/GeNMs processed into wires [10], ribbons [24], open meshes [12], and other complex structures.

## 1. Introduction

The enormous success in microelectronics or solid-state electronics demonstrated by group IV materials, especially silicon (Si), has led to considerable efforts by both academic and industrial researchers to expand understanding and technical applications. For microelectronics, Moore's law [1], first articulated in 1965, has been regarded as the paradigm that guides advancements in semiconductor technology. In the past decades, the Si-based microelectronics industry has gradually implemented several generations of technology nodes, continuing to extend Moore's law, including the most recent features, such as SOI (silicon-on-insulator) technology, strain engineering, and high-dielectric-constant (high- $k$ ) technology. Each node has exhibited not only economical new fabrication processes, but also improved transistor performance, including higher speeds and integration levels (i.e., field-effect transistors [FET] with smaller channel lengths), and lower power demands. However, as the channel length shrinks, the physical limits of pure Si are becoming significant problems. As a result, non-Si materials with high carrier mobility are being considered to replace or complement Si-transistor channels. To that end, germanium (Ge), which had already been considered and investigated when the first transistors were developed, is now being rediscovered because of its tremendous potential to operate at high speeds with low power requirements. Ge or SiGe alloys may become attractive options for future semiconductor technology not based on pure Si [2].

The remarkable development of the worldwide solid-state semiconductor industry has so far always been able to fulfill the demands of software developers and consumers regarding computational capabilities and desired new commercial devices. Even so, it is recognized that the unavoidable heat generated by the extremely dense integration of circuitry, plus other problems associated with high integration, will soon cause the collapse of the Moore's Law miracle. Many complementary or alternative approaches using novel designs and devices are therefore being implemented to expand the range of applications for the traditional group IV materials (e.g., Si and Ge). These approaches include property modifications through strain engineering, 3D micro/nano-architectures, and flexible/stretchable electronics, among others [3–9].

A significant platform for boosting this evolution is the single-crystalline Si, Ge, or SiGe alloy nanomembrane (NM, a thin sheet with nanometer to sub-micrometer thickness, free of substrate constraints at some stage in its life). The NM offers many superior features, including shapeability, strain-engineerability, transferrability, and patternability [3–23], as summarized in Fig. 1. Because of their compatibility with existing conventional complementary metal-oxide-semiconductor manufacturing technology, Si/GeNMs can be processed like a bulk wafer and shaped into any desired structure, such as micro/nano-wires [10], ribbons [11,24], open meshes [12], or other complex structures. Moreover, owing to their nanoscale thickness, which allows them to be pliable, rollable, and shapeable, Si/GeNMs can be assembled into three-dimensional

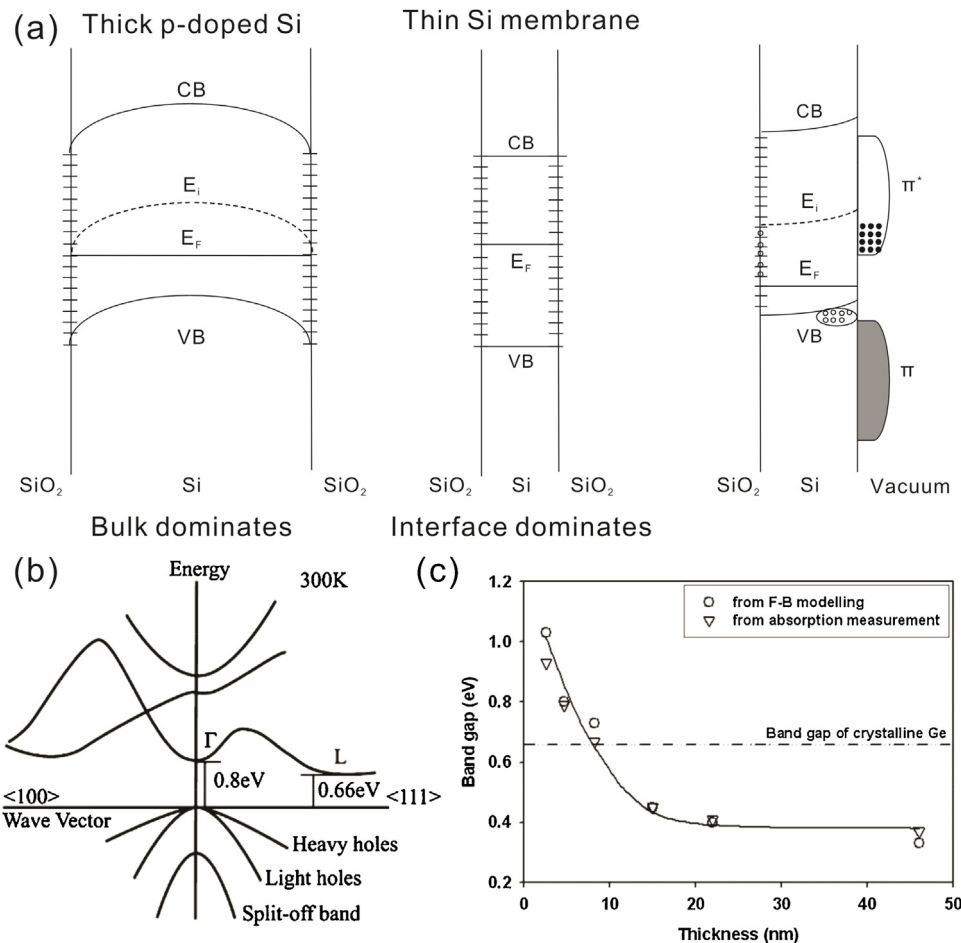


**Fig. 2.** Band structure effects in Si/GeNMs: (a) schematic diagrams of band alignments in bulk Si, ultra-thin SiNMs terminated by oxide layers, and clean ultra-thin Si with a Si/vacuum interface reconstructed into a  $(2 \times 1)$  structure [4]; (b) schematic diagram of the band structure of bulk Ge at room temperature [30]; (c) thickness effect on band-gaps of amorphous-GeNMs [31].

architectures, including tubes [13], 3D origami mesostructures [14], and wrinkles and buckles [15], through proper strain engineering. These features can be exploited for recently emergent inorganic flexible/stretchable electronics [16,17].

It is thus evident, as NMs can be easily transferred and integrated onto flexible, rigid, or transparent substrates of nearly any material, that many opportunities exist in the fields of inorganic flexible/stretchable devices, epitaxy-free hetero-integration, and transparent electronics [18]. In addition to the state-of-the-art doping of Si/GeNMs, their physical properties, especially band structure and charge carrier mobility, are tunable via strain engineering [12,19–23].

Below, we will review the basic properties of single-crystalline Si/GeNMs in Section 2; their synthesis and assembly strategies will be discussed in Section 3; in Section 4, the strain engineering of Si/GeNMs will be comprehensively reviewed, including the technical relevance, strained-Si technology, and tensilely strained Ge; mechanical assembly methods, mechanical principles, and the novel physical properties of 3D Si/GeNM-based micro/nano-architectures will be described in Section 5; in Section 6, various potential applications in sensors and transducers, bio-platforms, optoelectronics, energy harvesting, and flexible/stretchable electronics will be discussed; we will conclude with a brief summary and assessment of potential future developments and challenges.

## 2. Properties of Si/GeNMs

### 2.1. Energy band structures

Unlike in bulk materials, where large numbers of atoms contribute to the energy band structure, quantum confinement effects are induced in any semiconductor material that is sufficiently thin [25,26], with important implications for that material's energy band structure. For instance, the energy bands in SiNMs can be quite different from those of bulk Si because of the influence of interface and/or surface states [4,27–29]. For a sheet of p-doped Si thicker than 100 nm, for example, the bulk arrangement of atoms contributes more to the corresponding band structure than do the interface and surface states, and the band structure is quite similar to that of bulk Si [4], as shown in the left panel of Fig. 2(a). If the thickness of the SiNM decreases to less than 20 nm, the interface states of the oxide layer to which the SiNM is bonded will play a dominant role in trapping charges, and deplete the thin SiNM. Thus, the Fermi level ( $E_F$ ) is pulled closed to the mid-gap, like intrinsic Si [4], as illustrated in the middle panel of Fig. 2(a). The situation will be far different if the SiNM is exposed to the vacuum, and the surface will reconstruct into a  $(2 \times 1)$  structure to minimize the dangling bonds [27]. Calculated results indicate that surface  $\pi$  and  $\pi^*$  bands are also formed due to the charge transfer in tilted dimers, as sketched in the right panel of Fig. 2(a). Also, the Fermi level is pulled down close to the bulk valence band to balance the charges.

Thickness effects on band structures can also be observed in GeNMs. Fig. 2(b) shows, for example, the band alignment of crystalline bulk Ge, which clearly reveals an indirect band-gap feature [30]. The band-gap from the conduction-band minimum to the valence-band maximum is about 0.66 eV. For GeNMs deposited by electron-beam evaporation, thickness has been theoretically and experimentally demonstrated to have a significant influence on the bandgap, as illustrated in Fig. 2(c) [31], a result that to us seems rather puzzling and challenging. The bandgap of deposited Ge films increases as the thickness decreases, and it is much larger than that of the bulk crystal if the thickness is less than 10 nm. The thickness dependence of the band-gap can be attributed to the one-dimensional quantum confinement effect and the amorphous effect in GeNMs [31].

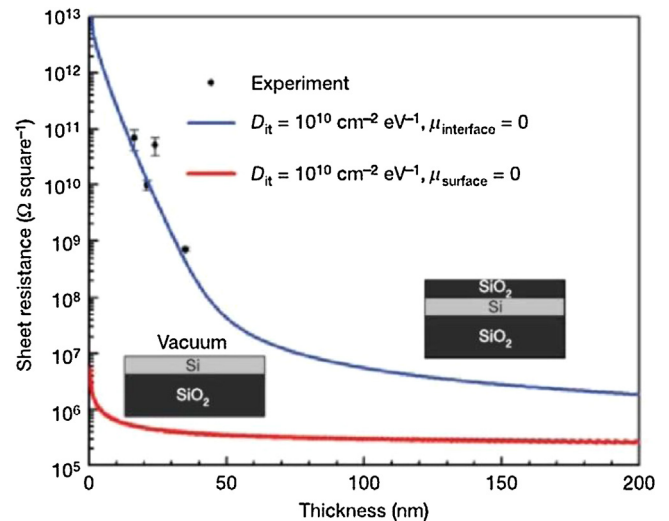


**Fig. 3.** The calculated thickness dependence of the sheet resistances for SiNMs with different bounding layers, with a comparison to an experiment for one case [27]. The diagrams show the respective bounding layers. The red curve assumes the band diagram shown in the right panel of Fig. 2(a), with a  $(2 \times 1)$  surface reconstruction. The oxide/Si interface states are assumed to be the same for both curves. The reason the sheet resistance is so much lower for the red curve is that its charges can be easily transferred from the “bulk” valence band to the surface conduction band, creating mobile charges in the bulk valence band. (For interpretation of the references to colour in this figure legend, the reader is referred to the web version of this article.)

### 2.2. Electrical conductivity

The electronic transport properties of NMs tend to be significantly different from those of bulk material, for several reasons. We use Si to illustrate the mechanisms influencing the transport properties of NMs. Fig. 3 shows the sheet resistances of SiNMs for two conditions: one for which the SiNM is sandwiched by two oxide layers (upper curve, right inset structure) and the other for which the SiNM is directly exposed on one side to vacuum, with a clean reconstructed Si(001) surface (lower curve, left inset structure) [27]. The most fundamental aspect is that as the thickness of the NM decreases, the total number of dopants existing per unit area becomes smaller and smaller. Therefore, the sheet resistance increases with the decrease of thickness for both situations, as shown in Fig. 3.

That alone does not explain the difference between the blue and red curves. That difference depends on the surface and interface states and the possible existence of a surface band structure that is distinct from that of the bulk form. As a NM becomes thinner, surface and/or interface states will gradually come to play the dominant role in the NM conductivity [27–29,32–34]. For instance, for a typical doping level of  $10^{15} \text{ cm}^{-3}$ , the density of dopants for a 100 nm-thick SiNM is only  $10^{10} \text{ cm}^{-2}$ . In contrast, at a Si/oxide interface, the density of interface states, in forms of Si dangling bonds, is about  $10^{11} \text{ cm}^{-2}$  [4,27]. Such states can trap charges at the interface, preventing their participation in conduction. As a result, the SiNM becomes depleted, with the sheet resistance rapidly increasing as the NM gets thin enough, approaching that of intrinsic Si, which indicates that the Fermi level is pinned close to the mid-gap (Fig. 2(a)). Thus, the electrical conductivities of thin oxide covered SiNMs are dependent on the competition between interface traps and dopants.

The electrical conductivity of a NM can therefore be modified by manipulating the interface conditions. In the case used for illustration here, the oxide layer is removed from one side to form a clean surface. For a Si (001) NM with a clean surface, a  $(2 \times 1)$  reconstruction forms to minimize the dangling bonds on

the surface [4,27,29]. This re-bonding forms surface  $\pi$  and  $\pi^*$  bands, which are positioned such that the bandgap between the surface  $\pi^*$  band and the maximum of the “bulk” Si valence band is about 0.35–0.6 eV, which is much less than the bandgap of bulk Si (1.1 eV). Thus, thermally excited electrons can cross this gap much more easily than the bulk band gap, as would be required for the SiNM covered by oxide layers, even though one oxide layer is assumed to be identical in both situations. This excitation of charges from the “bulk” valence band of Si to the surface band, termed “surface transfer doping” shown in the right panel of Fig. 2(a), creates mobile holes in the “bulk” valence band; and the conductivity increases markedly, even if the charges transferred to the surface remain immobile [27,34]. The red curve in Fig. 3 shows the effect on conductivity of introducing a surface band into which charges can be transferred easily. Such surface bands exist in many NM materials or can be introduced artificially via surface modification to manipulate the corresponding electrical conductivities of the thin sheet [34].

### 2.3. Opto electronic properties

Recently, a gate-controlled photovoltaic effect and negative transconductance in ultra-thin SiNM-based Schottky transistors with both asymmetric and symmetric contacts were demonstrated [35,36]. The device was built on a SOI material, with a Si substrate serving as the back gate; an ultra-thin SiNM top with a thickness down to 27 nm was the active channel. The source and drain electrodes, asymmetric (Ti and Cr/Au) and symmetric (Cr/Au and Cr/Au) contacts, were realized by electron-beam evaporation and liftoff. A typical device with asymmetric contacts is sketched in Fig. 4(a). Fig. 4(b) and (c) show currents through the channel versus gate voltage at a fixed drain voltage ( $-0.1$  V) for both types of transistors. Without light illumination, both transistors behaved like Schottky barrier-dominated source and/or drain contacts with ambipolar characteristics. When the middle of the SiNM channel was illuminated with a focused laser spot, unusual current-voltage curves with negative transconductance behaviors were observed for both transistors. As the gate voltage increased, the current firstly increased to a high level, and then decreased before rising again moderately. This unusual negative transconductance can be

attributed to the photovoltaic effect in both transistors, which is extremely sensitive to the Schottky barriers at the source and drain, thickness, and strain fluctuations in ultra-thin SiNM tops (27 nm). Moreover, Schottky barriers can be strongly affected by light illumination and surface states when the SiNM is extremely thin (e.g., 10 nm) [37].

Other novel optoelectronic properties can be achieved in rough SiNM-based transistors, such as giant persistent photoconductivity (GPPC) [38]. The SiNMs were roughened by chemical etching in KOH solution with a Cr layer as the mask. A typical atomic force microscope (AFM) image (Fig. 4(d) inset) demonstrates that the roughening treatment can produce ridges and valleys on the NM surface. The currents ( $I_{DS}$ ) varying with the voltage ( $V_{DS}$ ) of the transistors were measured with and without light, and the gate voltage was set at 0 V. In the dark, when the device was biased at a positive voltage, the rough surfaces suppressed carrier transport, inducing extremely low currents ( $\sim 0.03 \mu\text{A}/\mu\text{m}$ ) compared to those induced when it was biased at a negative voltage ( $-20$  V,  $10.3 \mu\text{A}/\mu\text{m}$ ). However, this suppression was dramatically overcome by illumination, as demonstrated in Fig. 4(d). Additionally, the highly conductive state in a rough SiNM, activated by the light, is able to persist for an extremely long time after the light is removed (more than one day), as shown in Fig. 4(e). This exceptional phenomenon in rough SiNMs is called GPPC. The same tests were performed on smooth SiNMs for comparison; however, no GPPC effect was observed, as shown in Fig. 4(e) (inset). It is thought that the presence of the large amount of ridges and valleys generates barriers for carriers, and localizes them in rough SiNMs. Light can activate the immobilized carriers and thus inducing the GPPC effect [38]. These experimental studies and theoretical investigations may pave the way for fabricating novel Si/GeNM-based optoelectronic devices.

### 2.4. Thermal conductivities and thermoelectric properties

The extreme thinness of Si/GeNMs also strongly influences the thermal conductivity and thermoelectric properties. In order to investigate the thickness effect on the thermal conductivities, suspended SiNMs with different thicknesses were fabricated by back etching a SOI substrate [39], as schematically illustrated in

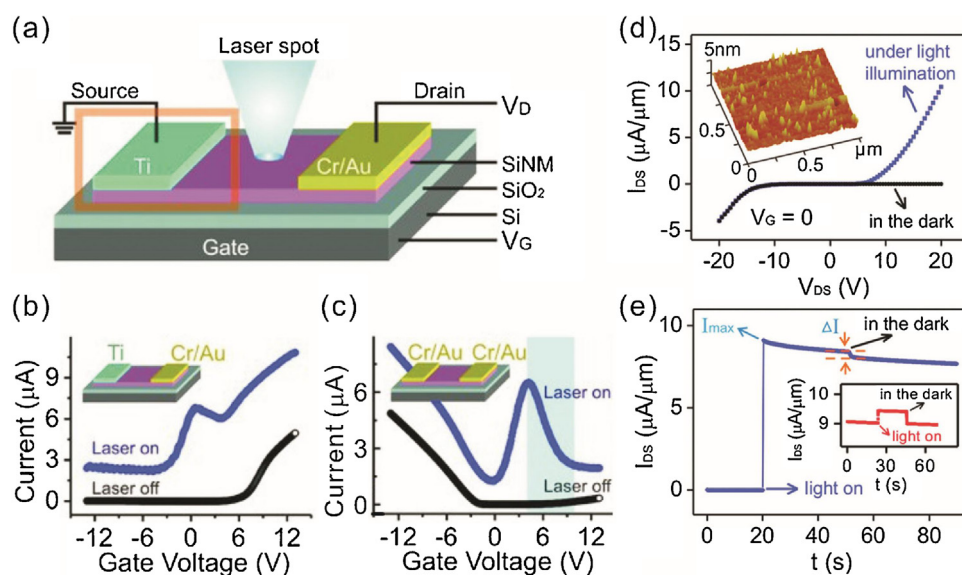


**Fig. 4.** (a) Schematic diagrams of a representative SiNM-based transistor with asymmetric contacts. A laser spot with tunable power and position was utilized to illuminate the SiNM channel.  $I_{DS}$ - $V_G$  properties of SiNM based transistors with asymmetric (b) and symmetric (c) contacts. Both devices were measured with and without laser irradiation [36]. (d)  $I_{DS}$ - $V_{DS}$  properties of a rough SiNM-based transistor in the dark and under light. The inset shows a typical AFM image of a rough SiNM. (e) Typical GPPC results for a rough SiNM-based transistor at  $V_{DS} = 20$  V and  $V_G = 2$  V. The inset shows the normal photoresponse of a smooth SiNM [38].

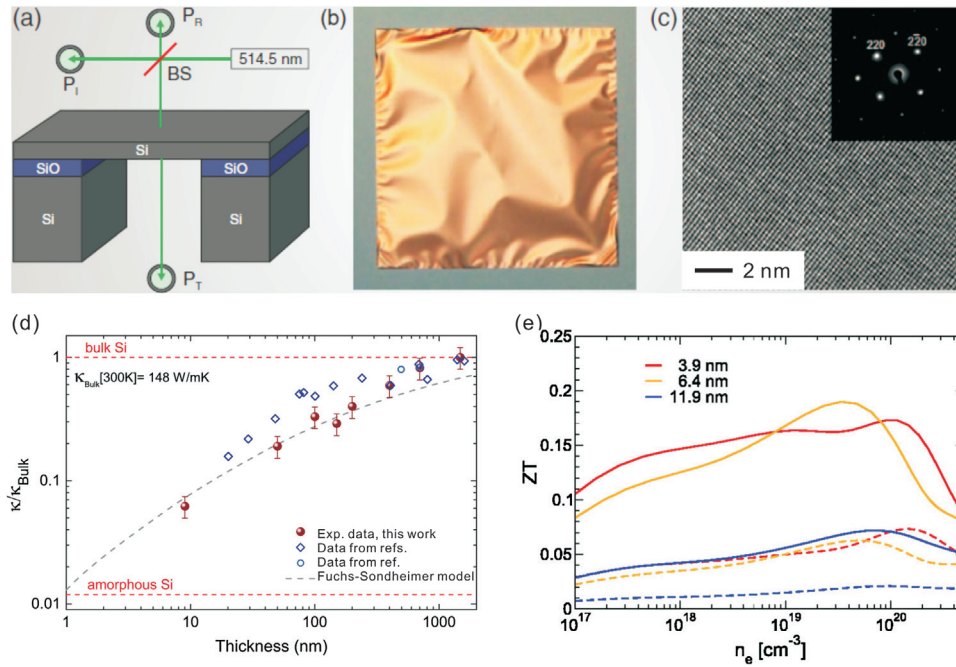


**Fig. 5.** (a) Schematic diagram of a suspended SiNM fabricated by back etching a SOI substrate, and the measurement configuration consisting of an incident laser (514.5 nm wavelength) and power meters ( $P_R$ ,  $P_I$ ,  $P_T$ ). (b) Optical-microscopy image of a representative suspended SiNM. (c) HR-TEM image of a representative single-crystalline SiNM. (d) Thermal conductivities of SiNM normalized to the bulk Si value ( $\kappa/\kappa_{\text{Bulk}}$ ) varying with thickness (solid red balls). The theoretical prediction using the Fuchs-Sonheimer model (gray dashed line), and the experimental results of SOI and membranes are shown for comparison. (For the references in Fig. 5d about the experimental results of SOI and membranes, the reader is referred to Ref. [43] and finds the cited literatures.) (a-d) reprinted from Ref. [39]. (e) The thermoelectric figure of merit,  $ZT$ , of SiNMs as a function of the carrier concentration at 300 K [43]. (For interpretation of the references to colour in this figure legend, the reader is referred to the web version of this article.)

Fig. 5(a). The thicknesses of the SiNM were controlled by gradual thermal oxidation, followed by removal of the oxide layer. Fig. 5(b) shows the optical-microscopy image of a representative as-fabricated suspended SiNM. The wrinkling of the NM results from

the release of compressive strain that was created during the thermal-oxidization process. Fig. 5(c) shows a typical high-resolution transmission electron microscopy (HR-TEM) image of the suspended SiNM, which confirms the single-crystalline nature.

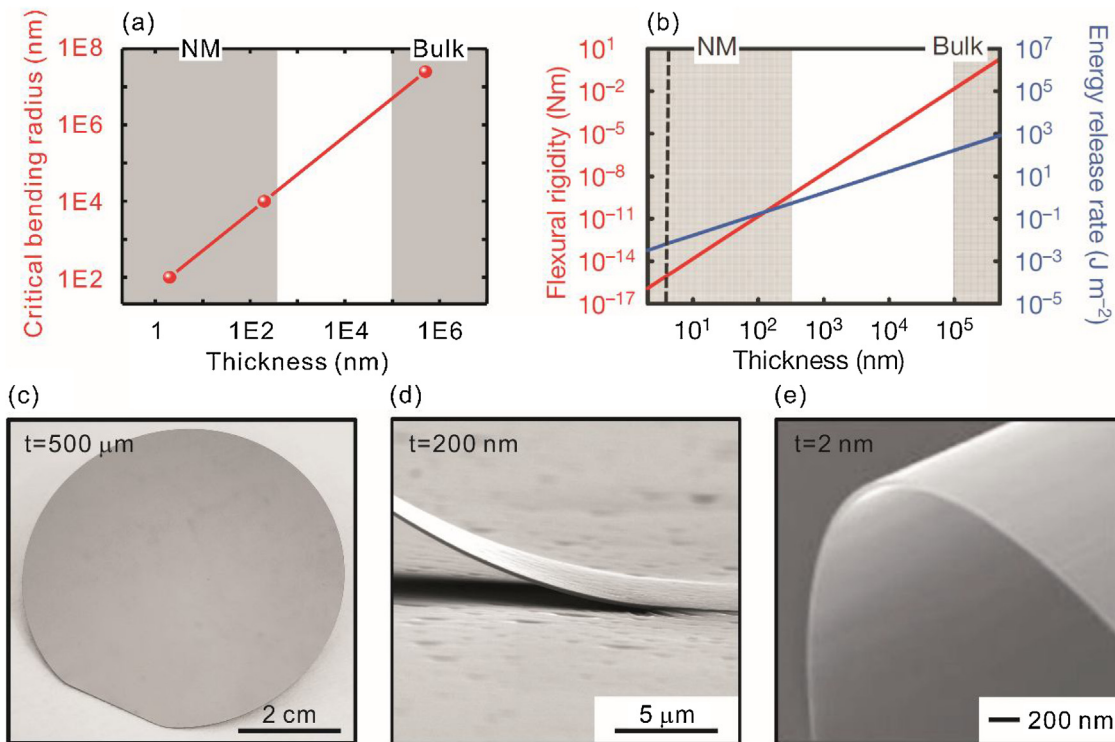


**Fig. 6.** (a) Calculated results of critical bending radii for different Si films with thicknesses ranging from 1 nm to 500  $\mu\text{m}$ . (b) Calculated results of flexural rigidities and energy release rates for SiNMs varying with thickness [3]. (c) Digital image of a Si wafer with a thickness of 500  $\mu\text{m}$ . (d) 200 nm-thick Si membrane on PDMS substrate. (e) SEM image of 2 nm-thick SiNM, showing extreme bendability without fracturing [3].

A series of SiNMs with thicknesses ranging from 9 nm to 1.5  $\mu\text{m}$  were measured by Raman thermometry, a novel contactless technique, to reveal the relationship between the Raman shift and the absorbed power. The thermal conductivity can be extracted from the absorbed power and temperature rise at the spot by solving the 2D heat equation [40,41]. Fig. 5(d) shows the normalized in-plane thermal conductivities ( $\kappa/\kappa_{\text{Bulk}}$ ) of SiNMs with various thicknesses. As the thickness decreases, the thermal conductivity correspondingly decreases, which agrees well with the theoretical model if the shortening of the mean phonon free path caused by phonon scattering at the boundaries is considered. When the thickness decreases to 9 nm, the corresponding thermal conductivity ( $\sim 9 \text{ W/mK}$ ) exhibits a 16-fold reduction with respect to the bulk value ( $\sim 150 \text{ W/mK}$ ) [42].

The interfaces between NMs and their supporting substrates also strongly affect their thermal conductivities. As shown in

Fig. 5(d), the thermal conductivities of SOI are consistently larger than those of suspended SiNMs with the same thickness [43]. D. P. Schroeder et al. indicated that the mechanically van der Waals-bonded interfaces of transferred NMs had extremely low interfacial thermal resistance [44]. Moreover, the surface conditions of mechanically created interfaces between like materials can affect the interfacial thermal resistance up to 300%. By introducing nanoscale surface engineering, including nanostructuring [45], morphology (rough or smooth) and composition (with/without a native oxide layer) [46], the thermal conductivities of NMs can be effectively tuned over 1–2 orders of magnitude. In addition, thermal conduction is also strongly determined by surface orientation and exhibits remarkable in-plane and out-of-plane anisotropy, which are induced by the interplay between boundary scattering and the anisotropy of phonon dispersions [47].

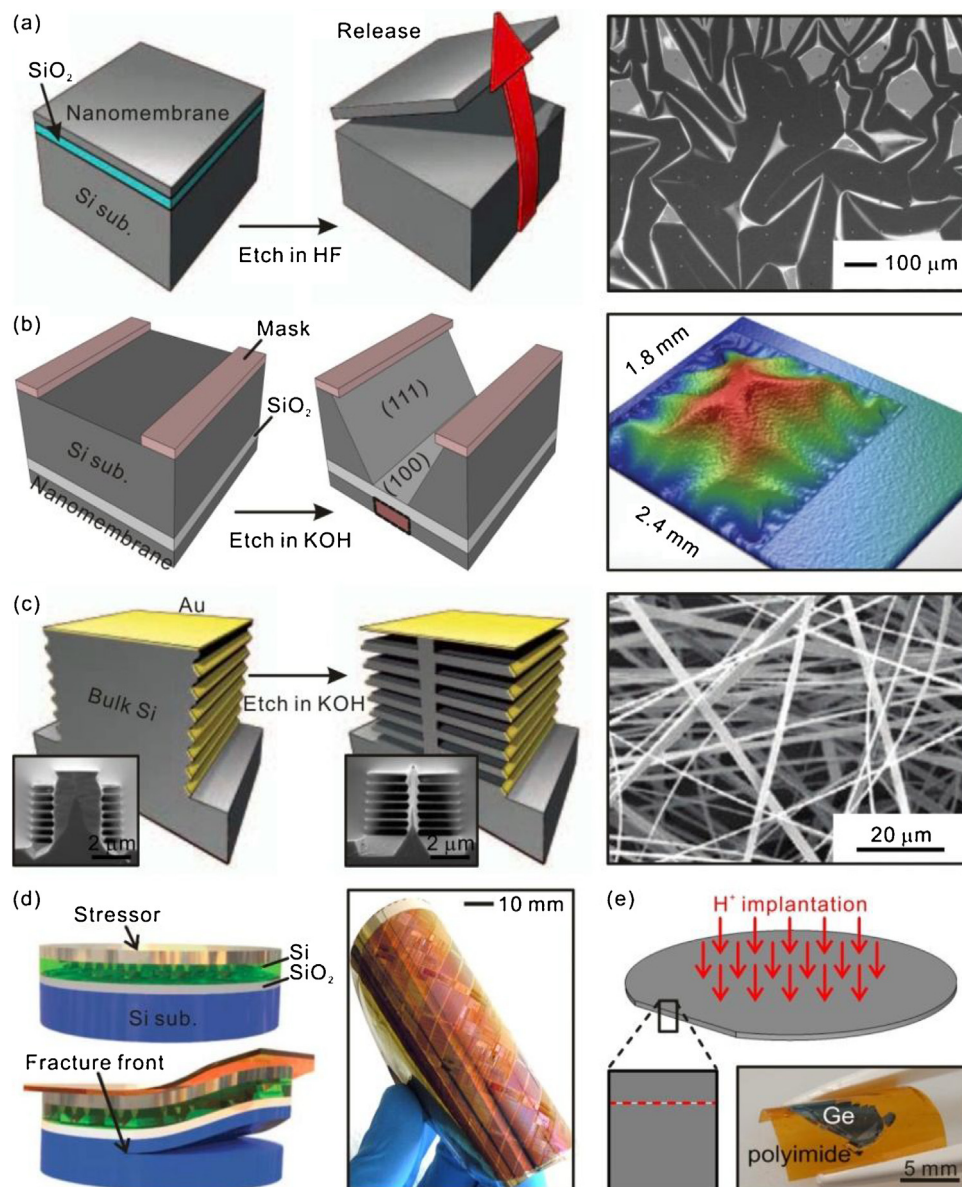


**Fig. 7.** (a) Release of a SiNM from a SOI wafer by selective etching of the underlying SiO<sub>2</sub> layer with HF. Optical-microscopy image of a typical released SiNM with large area [3]. (b) Release of a SiNM from a SOI wafer by back etching of the Si substrate with KOH. Optical-interferometry image of a released 100 nm-thick Si membrane made by back-side etching [59]. (c) Generating multilayer stacks of SiNMs from bulk wafers by anisotropic etching in KOH. The cross-sectional SEM images show two stages of the fabrication of multilayer stacks of SiNMs: etched in KOH for 2 min (left) and 5 min. (middle). SEM image of SiNMs generated from bulk wafer [62]. (d) Controlled spalling to exfoliate pre-fabricated devices and circuit from the rigid SOI wafer. A digital image of a 4-inch flexible ultra-thin-body, Si-on-insulator (UTB-SOI) circuit, prepared by this strategy, is also presented [63]. (e) Release of flexible Ge membranes by smart-cut process using a polyimide support [64].

One of the most promising applications for tuning the thermal conductivity of NMs is thermal management, which is critical in thermoelectric problems, energy harvesting, and the cooling of integrated circuits, as electronic device dimensions continue to shrink [44,48]. To obtain a high thermoelectric figure of merit ( $ZT$ ), two strategies can be followed: (1) reducing the thermal conductivity, and (2) increasing the electronic power factor. The work described above indicates that the thermal conductivity can be remarkably reduced by thinning a Si film into a NM, as well as surface engineering. Fig. 5(e) summarizes the theoretical predictions of the thermoelectric properties of SiNMs with a native oxide layer of various thicknesses and doping levels [43]. Remarkably, the highest  $ZT$ , a value of 0.2 (50 times larger than the bulk value), is achieved for 6.4 nm SiNMs with a high doping level ( $\sim 3 \times 10^{19}$ ). Further reducing or increasing the thickness (or doping level) does not improve the thermoelectric performance. Another approach for improving the thermoelectric performance is enhancing the electronic power factor. H. J. Ryu et al. presented a method for measuring the thermoelectric properties of a Si nanoribbon, and obtained a significantly enhanced power factor for nanoribbons by increasing the carrier density with an integrated back gate [49]. In a practical system, however, carriers can be provided by surface-transfer doping [28,50], which replaces either bulk doping or a metallic gate.

### 2.5. Mechanical properties

Anything thin enough can be flexible. It is difficult to bend conventional Si/Ge wafers (see digital Si wafer image in Fig. 6(c)) or exploit them for applications in flexible/stretchable electronics, because of their rigidity and brittleness. A reduction in thickness creates the possibility for these brittle wafers to become pliable. In particular, the critical bending radius ( $R_c$ ), defined as the bending radius at which a material starts to fracture, can be estimated by  $R_c = t/(2 * \epsilon_{fracture})$  [51], where  $t$  is the thickness, and  $\epsilon_{fracture}$  is the fracture strain. Values for critical strain vary (up to a theoretical elastic limit of 17–20% [52]). If one uses conservatively 1% for Si [15], the critical bending radii for films with different thicknesses can be calculated, and the results are summarized in Fig. 6(a). The critical bending radius decreases linearly as the thickness shrinks. For a NM with a thickness of 200 nm, as shown in Fig. 6(d), for example, the critical bending radius is calculated to be 10  $\mu\text{m}$ , which is far less than the diameter of a human hair ( $\sim 100 \mu\text{m}$ ). For conventional bulk wafers, however, the value of  $R_c$  approaches 0.1 m, which means they are hard to bend. Fig. 6(e) shows a typical scanning electron microscope (SEM) image of SiNMs (2 nm in thickness) exhibiting exceptional pliability [3]. As a corollary to the critical bending radius, the flexural rigidities of extremely thin NMs (down to 2 nm) can be more than fifteen orders of magnitude smaller than those of bulk wafers ( $\sim 500 \mu\text{m}$  in thickness) [3], as shown in Fig. 6(b).

Moreover, the energy release rates, also taken as separation energies for opening of interfaces between NMs and their supporting substrates, a process which plays a dominant role in conformal multilayer stacking by transfer printing, decrease linearly with the thickness of the NM, as shown in Fig. 6(b) [3]. Transfer printed conformal multilayer stacks of Si/SiO<sub>2</sub> are realized by multiple steps of SiNM transfer printing and thermal oxidation [53]. Such stacks can be exploited for photonic components (e.g., distributed Bragg reflectors, DBRs). The combination of decreased critical bending radii, flexural rigidities, and energy release rates for NMs (here specifically SiNMs) provides various possibilities, such as assembly into diverse non-planar 3D micro/nano-architectures, or stacking into multilayer assemblies on surfaces, that cannot be achieved by wafer-bonding techniques or epitaxy systems. Such non-planar constructions and stacks enable

emergent unconventional applications, especially in flexible/stretchable electronics [6,54].

## 3. Strategies to synthesize and assemble Si and GeNMs

The development of approaches to create Si, Ge, or SiGeNMs with precisely controlled thickness, lateral dimension, and doping type/concentration is crucial for their applications in high-performance and reliable electronic and optoelectronic devices. In a route similar to the synthesis of graphene or other 2D materials exfoliated from solids with layered structures, Si/GeNMs can be formed by chemical or mechanical release from bulk materials (e.g., Si from SOI, Ge from GOI (GOI: germanium-on-insulator)). The NMs thus obtained naturally keep the properties of the bulk material, such as crystallinity and doping type/concentration. In order to integrate them into functional devices, as-fabricated free-standing Si/GeNMs should be assembled onto supporting substrates. In the following parts of this paper, various strategies for synthesizing and assembling Si/GeNMs are described in detail.

### 3.1. Synthesis methods

SOI/GOI materials, with unique sandwich structures (i.e., Si/Ge top, oxide middle, and Si substrate), provide ideal platforms for synthesizing Si/GeNMs by the selective removal of the buried SiO<sub>2</sub> layer with hydrofluoric (HF) acid, as shown in Fig. 7(a) [3]. By utilizing photolithography and reactive ion etching (RIE), the top Si/GeNMs can be patterned into various geometries, such as ribbons, wires, etc. It should be noted that to fully undercut or accelerate the etching process of the sacrificial layer, small “etching window” arrays, shown in the right panel of Fig. 7(a), are usually employed. The back side etching of handle wafers (Si substrates) provides an alternative approach for synthesizing larger-area, continuous Si/GeNMs, as displayed in Fig. 7(b). The handle wafer can be selectively removed either by wet chemical etchants (e.g., KOH) [55–59], or by a dry RIE process [60,61], where the buried oxide layer (BOX) acts as an etch-stop for both cases, resulting in the formation of larger-area, continuous Si/GeNMs. The shape and size of the released NMs are determined by the pre-designed etching mask. The right panel of Fig. 7(b) shows a typical released SiNM with a size of 1.8 mm  $\times$  2.4 mm from SOI [59]. The most remarkable advantage of the two methods just given is that the properties of the achieved Si/GeNMs, such as thickness, doping level, crystalline quality, etc., are completely determined by the donor sources, i.e., the SOI and/or GOI materials. Therefore, one can obtain Si/GeNMs on demand by choosing the appropriate SOI/GOI source.

Although release of Si/GeNMs from SOI/GOI materials is simple and convenient, the high cost of such sandwiched donor sources may become a drawback for further applications. A synthetic strategy that involves exfoliating Si/GeNMs from bulk wafers could provide additional choices. For example, defining trenches on bulk (111) Si wafers with sculpted sidewalls, then selectively depositing gold resist on the sidewall by angled electron beam evaporation provides a starting point for an isotropic etching along the  $\langle 110 \rangle$  directions by utilizing KOH. Large quantities of SiNMs can be produced by this strategy, as demonstrated by the SEM image in the right panel of Fig. 7(c) [62]. Single-crystalline GeNMs can also be generated by exfoliating from bulk Ge wafers with another approach [64]. By combining the ion-implantation-based [65–68] smart-cut process and adhesive wafer bonding, a large-area Ge membrane can be transferred onto a flexible polyimide substrate, as shown in the digital image in Fig. 7(e). This combination can be exploited for further applications in flexible Ge-based photo-detectors [64]. Because the surface morphologies of transferred GeNMs are extremely rough after splitting, the surface needs to be

polished chemically and mechanically prior to any subsequent device fabrication. Although the smart-cut process could provide a possible alternative approach for fabricating GeNMs on flexible substrate, post-polishing GeNMs on a flexible substrate can be extremely difficult because of delamination between GeNMs and the flexible substrate. This situation can be significantly improved when the smart-cut GeNMs are transferred and bonded to a rigid substrate (e.g., a SiO<sub>2</sub>/Si wafer) in a manner similar to the Smart-Cut™ technology [69]. The bonding strength between GeNMs and the SiO<sub>2</sub>/Si substrate is sufficient to sustain the mechanical stress during the polishing process, and eventually a wafer-scale GeNM-on-SiO<sub>2</sub>/Si substrate (i.e., a GOI wafer) with a smooth surface is realized [70]. In addition to Si/GeNMs that can be released or exfoliated from bulk wafers, their corresponding devices and circuits can also be transferred from a brittle substrate and assembled onto a flexible substrate by a controlled spalling technique, as shown in Fig. 7(d) [63]. The process begins with depositing a thick nickel stressor layer on a rigid wafer with pre-fabricated complementary metal-oxide-semiconductor (CMOS) integrated circuits. The intrinsic stress level and thickness of the stressor layer should satisfy the conditions for the spalling process. As a result, a single spalling-mode fracture can be mechanically guided across the wafer by applying a polyimide (PI) tape onto the surface, which leads to an extremely flexible UTB-SOI circuit.

Because the thickness of Si/GeNMs plays a crucial role in their electronic/optoelectronic properties, various advanced thickness-control techniques have been explored for use with Si. For example, the Y. Cui group utilized a chemical etching method to thin a Si wafer into free-standing ultra-thin single-crystalline flexible Si by KOH, with uniform and controllable thicknesses ranging from 10 to sub-2 μm [71]. Because SiNMs can be conveniently released from

SOI materials, as discussed above, researchers also pursued efforts to thin the top Si layers of SOI, then release them if needed. In order to obtain SiNMs with desired thickness, the wet-chemical-clean [33], plasma etching [33], or oxidation-selective etching processes [51] are recommended, because of their controllable and stable etching rate. Utilizing a cyclic wet-chemical-clean process in piranha (H<sub>2</sub>SO<sub>4</sub>+H<sub>2</sub>O<sub>2</sub>), AHP (NH<sub>4</sub>OH+H<sub>2</sub>O<sub>2</sub>, 80 °C), and diluted HF (12%), Chen et al. fabricated SiNMs as thin as 1.3 nm [33]. Combining oxidation and selective etching processes, J. A. Rogers and J.-H. Ahn produced larger-area single-crystalline SiNMs with controllable thicknesses ranging from 1.4 to 10 nm [51]. By using the above approach, the A. Javey group successfully thinned a 70 nm SiNM of SOI down to 3.5 nm, and constructed chemical-sensitive 3.5-nm-thin Si transistors for applications in low-power, sensitive, and selective multiplexed gas-sensing technology [72]. Moreover, ultra-thin SiNM-based transistors can be exploited for mimicking biological synapses [73,74] and used in implantable flexible devices [75,76]. These potential for applications are promising for building neuromorphic and other bio-medical systems.

### 3.2. Assembly approaches

Further applications of synthesized free-standing Si/GeNMs are severely challenged by the difficulty of integrating them onto appropriate substrates, depending on the intended use. Various assembly strategies have been developed; these are divided into primarily two categories: wet transfer [5,9] and dry transfer (i.e., transfer printing) [18,77,78]. After selective removal of the buried oxide layer from SOI/GOI, the top Si/GeNMs float to the surface of the solution when slightly agitated, as shown in Fig. 8(a). Then they

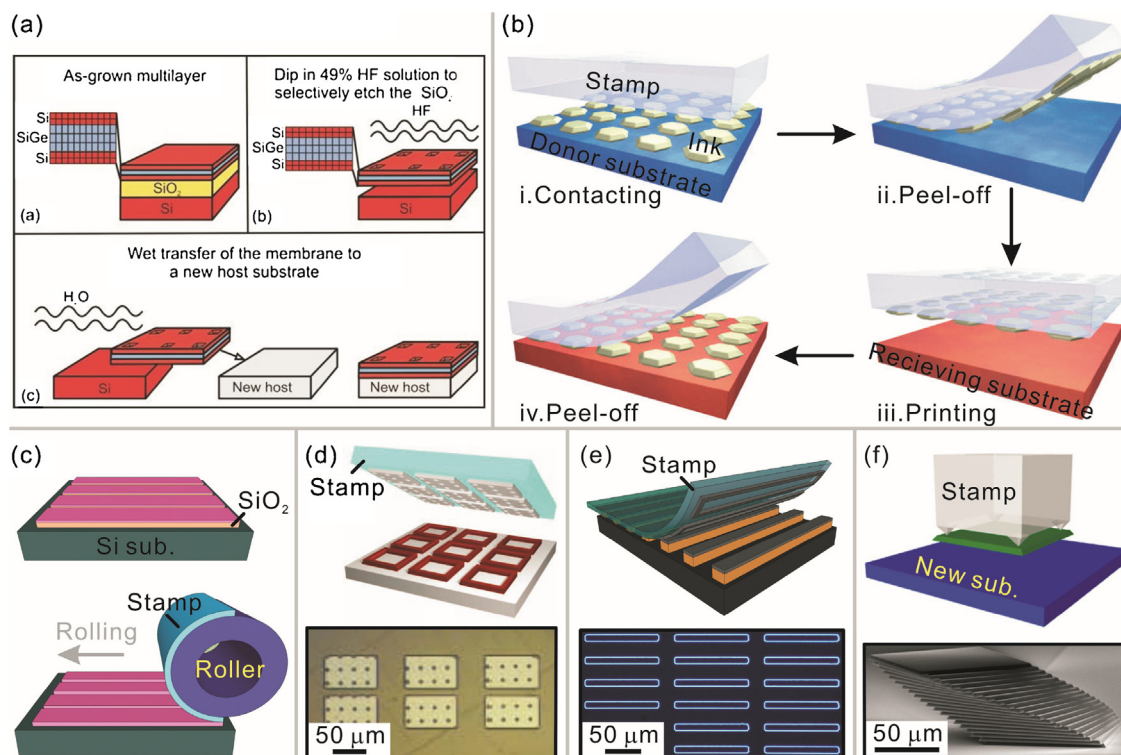


**Fig. 8.** (a) Wet-transfer process involves NM floating on the surface of the solution and being transferred to a new host surface [9]. (b) Schematic illustration of the process flow of the dry-transfer technique (also known as transfer printing) [18]. (c) Schematic illustration of the rolling-transfer technique for roll-to-roll production of flexible functional devices [81]. (d) Deterministic assembly of Si/GeNM array by “photoresist anchor”. The bottom shows an optical-microscopy image of a transferred SiNM array on a PDMS substrate [82]. (e) Deterministic assembly of Si/GeNM array by “edge-cutting transfer”. An optical-microscopy image of a Si (or Ge) nanoribbon array on a PDMS substrate is shown at the bottom; the width of each transferred nanoribbon is in the range of 500–1000 nm [83]. (f) Deterministic assembly of NMs by micro-structured elastomeric surfaces with reversible adhesion. The bottom displays a SEM image of multilayer configurations of SiNMs with small incremental rotations and translations [84].

can be transferred out of the solution by contacting them with a host substrate. Although the uncontrollable alignment and surface morphology may be negative features, this wet-transfer technique offers a simple and rapid strategy for the transfer and integration of NMs as well as 2D materials, such as graphene [79] and MoS<sub>2</sub> [80].

Another strategy, the dry-transfer technique, is proposed to integrate Si/GeNMs onto various substrates in a conformal and controllable manner, as sketched in Fig. 8(b) [18]. The released Si/GeNM array is fast picked up by a polydimethylsiloxane (PDMS) rubber stamp. Then it is integrated on the host substrate by conformal contact and slow peeling-off of the PDMS. The as-proposed adhesion forces between the interfaces of the PDMS/NM and NM/donor, which enable the transfer or printing process, are kinetically controllable by the peeling rate of the stamp. Peeling the stamp off rapidly induces the NM to separate from the donor substrate and transfer onto the PDMS stamp. Peeling it off slowly, however, causes the NM to be released onto the receiving substrate.

One of the best features of dry transfer is that, because of the van der Waals force, the released NMs can preserve the original alignment to a great extent. However, the spatial order may still have a slight shift, on the micro/nanoscale, that could significantly limit further high-precision-device fabrication. In order to deterministically assemble the released Si/GeNM-based array, investigations to modify the transfer-printing technique have been under way, such as a “photoresist anchor” to fix the released array [82], or an “edge-cutting transfer” to transfer flexible Si/Ge nanoribbons [83], as shown in Fig. 8(d) and (e), respectively. Both strategies involve fixing the released Si/GeNMs by pre-designed anchors to exactly preserve the spatial order before and after the transfer-printing process. For the former one, the fixing structure is a photoresist underneath the suspended NM which can anchor it over a large area (up to 10.8 mm × 10.8 mm) [82]. As for the “edge-cutting transfer”, the partly etched buried oxide layer’s edges serve as the anchors for Si/GeNMs with extremely small widths (down to 500 nm) [83]. Other transfer-printing strategies, such as “rolling

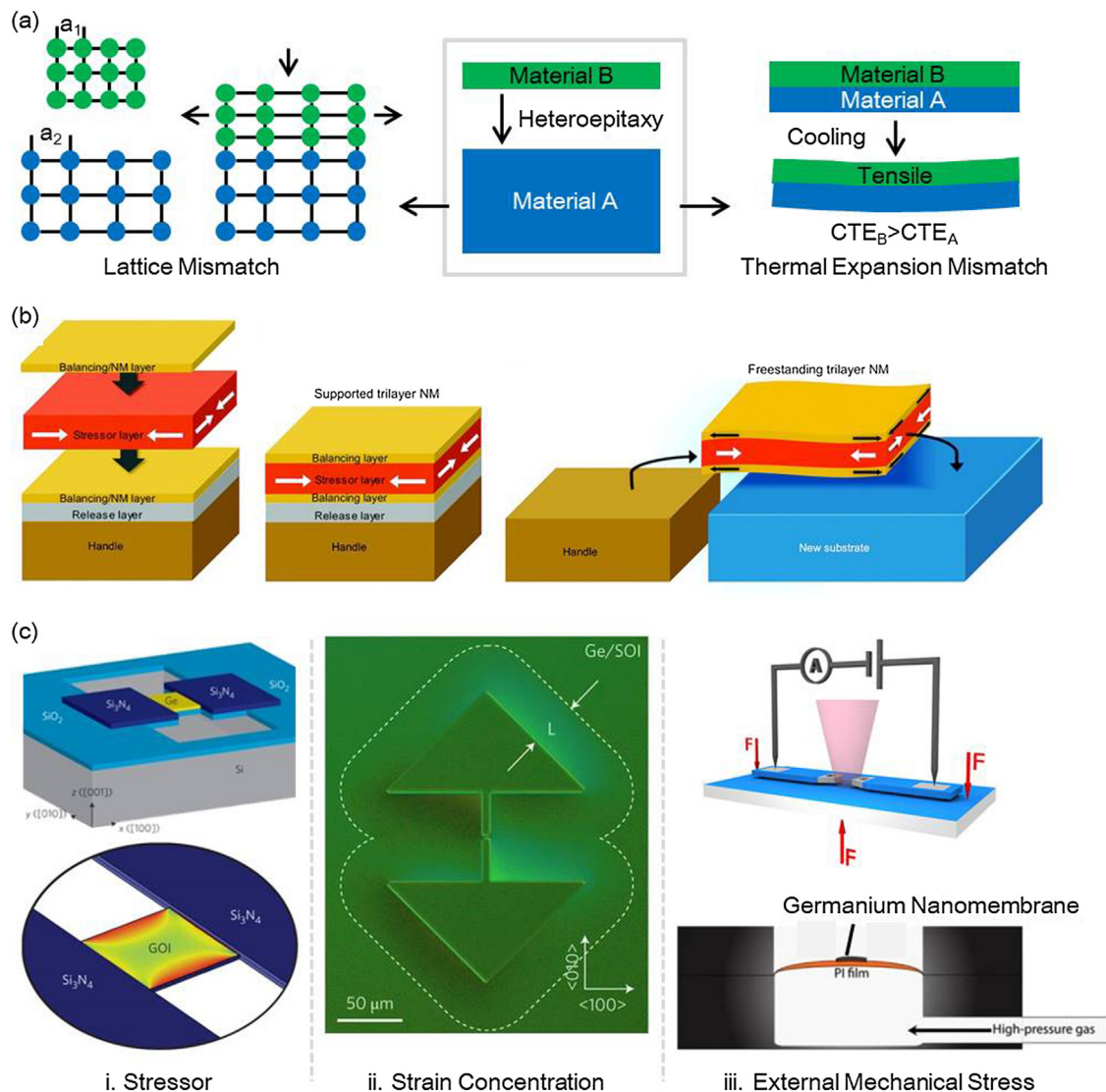


**Fig. 9.** Various strain engineering strategies for Si/GeNMs: (a) strained epitaxial layers of Si/GeNMs resulting from lattice or thermal-expansion mismatches: left: heteroepitaxy; right: thermal expansion mismatch results in bending for thin bilayers. (b) schematic illustration of elastic strain-shearing [91]: left: trilayer heteroepitaxy; right: release causing strain sharing and transfer/bonding to new host. (c) several external mechanical techniques for generating strained Si/GeNMs: (i) external stressor: the suspended GeNM can be stretched by the Si<sub>3</sub>N<sub>4</sub> stressor tying on both sides [21]; (ii) strain concentration by relaxation: strain initially existing in the larger-area pads can be concentrated into the center nano-strip through relaxation [92]; and (iii) external mechanical stress: mechanical bend of the Ge nanowires (up) and expansion of GeNMs (bottom) could induce uniaxial and biaxial tensile strain [20,93], respectively.

transfer”, are proposed to transfer released NMs in a fast and controllable manner by a roller-type stamp (Fig. 8(c)), which can be exploited for roll-to-roll mass production [81,85]. J. A. Rogers and his collaborators presented a special micro-structured elastomeric stamp for tuning the adhesion force between Si membranes and PDMS in a reversible manner, which enables control of the transfer and printing processes, as shown in Fig. 8(f) [84]. H. Ko and his collaborators, inspired by the octopus, demonstrated smart adhesive pads with thermoresponsive actuation of a hydrogel layer on elastomeric microcavity pads, thus inducing switchable adhesion by thermal stimulus [86]. These advanced assembly strategies allow wide possibilities to exploit Si/GeNMs in unconventional flexible/stretchable electronics, 3D stacked hetero-integration, and complex 3D micro/nano-architectonics.

#### 4. Strain engineering of Si/GeNMs

A significant feature of Si/GeNMs is that they can be strain-engineered with the proper stress methods. Two classes of deformation can be realized: (i) *in-plane deformation* that increases or decreases the lattice constant; (ii) *out-of-plane deformation* that transforms the geometry from 2D membranes into 3D micro/nano-architectures. Coexistence can be found within these two types of strain engineering.

##### 4.1. Strain engineering of 2D Si/GeNMs

Some physical properties of Si/GeNMs, including band structure, conductivity effective mass, and scattering rate, can be altered by modifying the lattice constant with proper strain engineering. A variety of strain engineering strategies for modifying the lattice constant has been developed, such as heteroepitaxy, defect-free strain sharing, and external mechanical stressors, as summarized in Fig. 9. For example, tensilely strained Si (or Ge) can be grown heteroepitaxially on a  $\text{Si}_{1-x}\text{Ge}_x$  ( $\text{In}_x\text{Ga}_{1-x}\text{As}$ ) buffer layer [87–89], where the strain value can be tuned by changing the Ge (or In) content. Thermal-expansion mismatch can also be effectively used to create strain. These approaches are shown schematically in Fig. 9(a) and (b). The significant advantage of heteroepitaxy for achieving strained Si/GeNMs is that the sign and magnitude of the strain value can be controlled by changing substrate composition, thickness ratio of the buffer and epitaxial layers (once the NM is released), annealing conditions, and growth conditions. For example, a somewhat tensilely strained layer of Ge can be realized by ultra-high vacuum chemical vapor deposition, where the strain can be adjusted by growing it at different temperatures [90].

Heteroepitaxy by itself has limitations, however, in that the thickness of the film that can be grown before the formation of dislocations is limited. In order to eliminate this problem, the elastic strain-sharing technique was introduced [5,12,91,94], as shown schematically in Fig. 9(b). During growth, the starting balancing layer is held rigidly at its bulk lattice constant by the balancing NM/release layer interface. Therefore, the epitaxial growth of the stressor layer produces a compressively strained film in registry with the underneath balancing layer, if the corresponding lattice constant is larger than that of the balancing layer (or a tensilely strained film if the lattice constant is smaller). Subsequent growth of the same top balancing layer is therefore without strain. Once the sacrificial release layer is removed, the compressive strain will partially transfer into the balancing layers, leading to tensile strain in the top epitaxial layer by elastic strain-sharing (or vice versa if the middle layer is tensilely strained). The strain value is determined by the lattice constant difference and the thickness of the stressor layer, which should be less than its critical thickness to avoid undesirable dislocation defects [5].

In addition to the above two methods, several methods for strain engineering of Si/GeNMs through external mechanical stress/stressors have been developed recently, as summarized in Fig. 9(c). Because no heteroepitaxy is involved, the starting Si/GeNMs can be single-crystalline and defect-free. For example, by stretching a fully released single-crystalline GeNM from a GOI wafer with a suitable  $\text{Si}_3\text{N}_4$  stressor deposited on it, both uniaxially and biaxially tensile-strained GeNMs with enhanced light emission were achieved [21]. Through pre-designed “micro-bridge structures”, strain applied to Si/GeNMs can be concentrated to obtain high strain values [19,92,95]. The approach starts with patterning and under-etching pre-designed micro-bridge structures from a biaxially strained SOI/GOI wafer, as shown in the middle panel of Fig. 9(c). As the releasing process proceeds, strain will be re-distributed and concentrated in the middle of the micro-bridges, while decrease close to the pads. Under such a strain-concentration approach, the strain (uniaxial) value can reach up to 3.1% and 4.5–4.6% for Ge [92] and SiNMs [19,95], respectively. External mechanical stress induced by bending [93,96] and high-pressure expansion [20] are also utilized to generate controllable uniaxial [93] and equi-biaxial [20] strain in Si/GeNMs, leading to substantial alterations of the physical properties.

All the above techniques have their respective advantages in producing strained Si or GeNMs. For the external-mechanical stress/stressors technique, tensilely strained Si/GeNMs can be conveniently generated without introducing any defects, where the strain value can be simply tuned through the geometry design of the stressors. This technique could be carried out on almost any materials to produce tensile strains, such as, but not limited to, graphene [97–99],  $\text{MoS}_2$  [100], ZnO [101], and GaAs [102]. However, the produced tensile strain by most external stressor methods is uniaxial or only a small biaxial strain. In addition, it is really difficult to create compressive strain in NMs and keep the NMs flat and not rippled by this technique. Although tensilely strained GeNMs in which the strain is induced by external mechanical stress provide ideal platforms for fundamental studies of tensile strain and optical properties of GeNMs, exploiting this approach for device applications in a simple and convenient manner is still quite challenging, because the complex setups to create tensile strain in GeNMs are difficult to make completely compatible with current device fabrication processes. Heteroepitaxy can provide complementary advantages, especially in the ability to create either tensile or compressive strains in Si/GeNMs. By utilizing a selective epitaxy of SiGe embedded into Si or a silicon nitride stressor on the top of Si channels, uniaxial compressive or tensile strain, albeit with small value, can be introduced into Si channels, which enables high-performance PMOS or NMOS due to enhanced hole or electron mobility [103]. Though the defects in NMs originating from lattice mismatch may affect the subsequent device performances, this can be significantly improved by the epitaxy-based strain sharing methods.

##### 4.2. Strained-Si technology

One of the great challenges to the further scaling-down of Si-based metal-oxide semiconductor field-effect transistors (MOS-FETs) involves enhancing carrier mobility while maintaining electrostatic integrity [19]. Mobility enhancement in Si can be realized by strain-induced band-structure modification, which further modulates the corresponding effective masses and phonon scattering [5,88]. For an unstrained-Si conduction band, the 6-fold degenerate valleys feature ellipsoidal constant-energy surfaces. The electron effective mass is consequently anisotropic. These subbands will be shifted and split under external stress. For example, in Si (001) uniaxial tension along  $\langle 110 \rangle$  induces shifting down the  $\Delta_2$  energy band and shifting up the  $\Delta_4$  energy band. Electrons will

repopulate from the  $\Delta_4$  valley to the  $\Delta_2$  valley, which causes an average effective mass decrease and a carrier mobility increase.

For the unstrained-Si (001)-valence band, the heavy-hole and light-hole bands are degenerate [88]. Under  $\langle 110 \rangle$  uniaxial compression, for example, the degeneracy is lifted, and band warping occurs. At room temperature, this band warping will induce effective-mass reduction, which is the dominant factor for mobility enhancement in p-type Si, as the splitting energy under uniaxial stress is small compared with the Si optical-phonon energy. Studies have confirmed both experimentally and theoretically that strain enables mobility enhancement of about 4.5 times in Si-based pMOSFETs, and of about 2 times in nMOSFETs without a significant leakage current increase [104,105].

Based on the above analysis, Ma's group developed a flexible strained-SiNM-based device array [23], as shown in Fig. 10(a). The fabrication of strained-SiNM-based flexible electronic devices is complicated by the need to maintain the strain existing in a transferred SiNM after it is fully released from the rigid substrate. As a result, an alternative strategy that creates biaxial compressive strain in SiNMs on a polyimide film has been demonstrated [106]. Because the compressively strain is known to enable the hole mobility enhancement in Si, the ability to fabricate compressive strained SiNMs will broaden the possibilities of flexible electronics, especially for gaining high-performance flexible PMOS devices. Namely, SiNMs transferred on a polyimide substrate were processed successively with heating, annealing, and cooling treatments. The strain in SiNMs transformed from tensile to compressive states, and eventually reached a stable biaxial compressive state, where the compressive strain values (up to 0.54%) can be varied by controlling the thermal annealing temperatures. Another approach that involves a strain-sharing technique [5,12,91,94] was chosen to create self-sustained strain in the SiNMs. By strain-sharing, tuning the thickness ratio of different layers, and adjusting the Ge composition of the alloy layer, about 0.35% biaxial tensile strain is introduced into SiNMs [23]. The typical construction of a transistor is revealed by the optical-microscopy image shown in Fig. 10(b). The transfer curves and calculated transconductance ( $g_m$ ) characteristics of unstrained and strained flexible SiNM-based devices are summarized in Fig. 10(c). By utilizing strained-SiNMs as channels, about 47.3% enhancement in carrier mobility and transconductance can be achieved compared with unstrained devices.

### 4.3. Tensilely strained Ge

#### 4.3.1. Energy band structures versus strain

Ge, which exhibits a pseudo-direct bandgap behavior due to the small energy (136 meV) difference between indirect and direct bandgaps [107], has been playing a critical role in Si-based photonics. Unstrained Ge is known to have an indirect bandgap of 0.664 eV at the L valley, and a direct bandgap of 0.8 eV at the  $\Gamma$  valley, as shown in Fig. 11(a) [108]. When tensile stress is applied,

the band structure can be engineered to reduce the difference between the indirect and direct bandgaps, and Ge is transformed into a direct-gap semiconductor with sufficiently large tensile strain. Theoretical predictions indicate that uniform expansion in all directions could induce the direct bandgap behavior transition at a small strain of about 0.8% [30]. In practical terms, however, tensile strain in a crystal can be generated only uniaxially (along one crystallographic direction) or biaxially (isotropically in a plane). As a result, the corresponding critical strain values for a direct-bandgap transition vary according to the applied strain direction. For example, about a 2% biaxial strain in a  $\{100\}$  plane is expected to realize the transition [107,109]. For uniaxial stress, however, the required strain for a direct bandgap transition is calculated to be more than 4% [30].

The band structure varying with the strain existing in Ge directly determines the light-emission properties, which can be investigated via photoluminescence (PL) characteristics. Fig. 11(b) exhibits the typical room-temperature PL spectra obtained from a 40-nm GeNM under different biaxial strains [20]. As the applied strain is raised, the emitted wavelengths display a significant red-shift with increased integrated intensity, indicating enhanced light-emission efficiency. This behavior can be explained by theoretical predictions about lowering the direct bandgap with increased tensile strain. As shown in Fig. 11(c), the calculated direct and indirect conduction-to-heavy-hole and conduction-to-light-hole bandgaps (solid lines) versus strain agree well with the peak emission energies (symbols). It is obvious that both the  $c\Gamma$ -lh and  $cL$ -lh bandgap energies decrease with the increase of applied strain. However, the shrinkage rate of the direct bandgap is much faster than that of the indirect bandgap. As a result, when the biaxial strain reaches 1.9%, a GeNM will change from indirect to direct bandgap behavior.

In general, all four transitions can participate in the light emission process, as shown by the symbols in Fig. 11(c). When the applied strain is small or zero, the hh and lh band edges are nearly degenerate; therefore the direct and indirect transitions can contribute to light emissions. At the intermediate strain values, e.g., 0.75%, both the direct and indirect transitions into both valence bands will simultaneously appear. At high strains, however, indirect transitions will be suppressed due to the decreased number of electrons in the L valleys. Therefore, only direct transitions into both valence bands will appear.

#### 4.3.2. Optoelectronic applications

Device integration enables a particular characteristic of strain engineering based on tensilely strained GeNMs. Under strain conditions, the bandgap energy of Ge red-shifts into the mid-infrared spectral range, which is critical for the development of efficient mid-IR light sources that can be monolithically integrated with CMOS electronics [110]. Fig. 12(a) shows a schematic cross-section of a strained Ge PN-junction-based photodetector. The strain in the suspended Ge is provided by the back side stressor, i.e.,

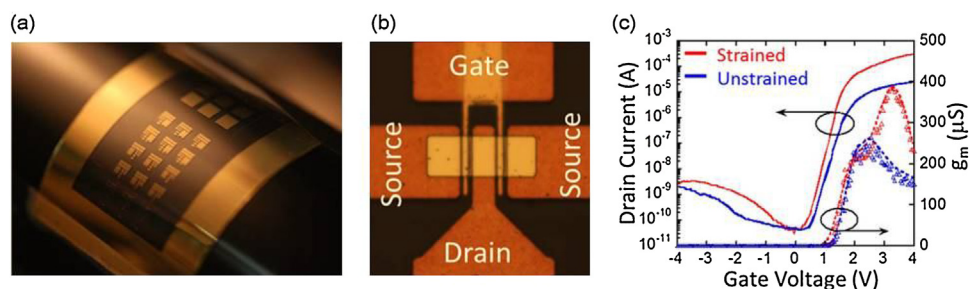


**Fig. 10.** (a) Flexible strained-Si-based device array on a bending fixture. (b) Optical image of a typical strained-Si-based transistor. (c) Transfer curves and calculated transconductance curves of unstrained and strained-Si-based devices. Reprinted from [23].

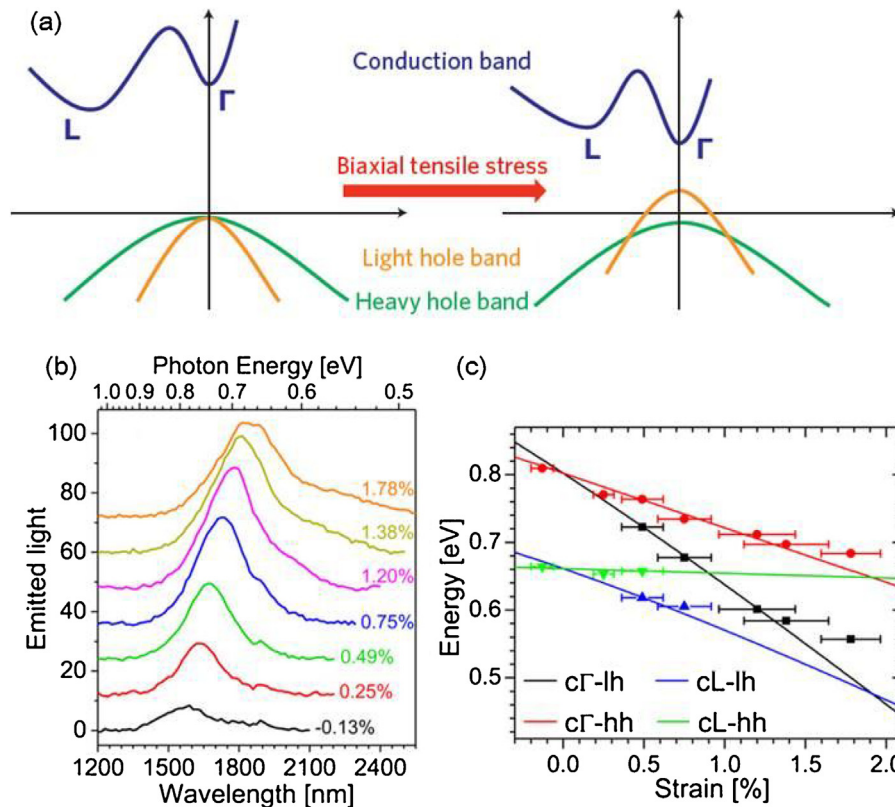


**Fig. 11.** (a) Strain-induced band-gap shrinkage in Ge [108]. (b) PL spectra of a GeNM with a thickness of 40 nm under different strain values. (c) Lines, calculated bandgap energies between the  $\Gamma$  or L conduction-band minima, and the heavy-hole or light-hole valence-band maxima; symbols, experimental peak emission energies extracted from the PL spectra. (b–c) reprinted from [20].

tungsten [111]. An un-doped Ge layer and  $n^+$ -Ge are grown epitaxially without a subsequent annealing to avoid phosphorous dopant diffusion. Dry etching was utilized to form a high mesa, exposing p-type Ge as the supporting layer. After the Si substrate was selectively removed and the tungsten layer was deposited (serving as the stressor layer), both n and p-type contacts were created to form the final device, as revealed by optical-microscopy in the right panel of Fig. 12(a). Based on the normalized photocurrent spectra from different samples under varying strain values (not shown), distinct red-shift behaviors can be observed in the response wavelengths, which can be attributed to the direct bandgap reductions in Ge resulting in enhanced absorption of the longer wavelengths.

In addition to the photoluminescent properties, electroluminescent devices were also demonstrated based on tensilely strained GeNMs [112]. As exhibited in Fig. 12(b), n-doped Ge layers were directly grown on an n-doped GaAs substrate to form a heterojunction at the Ge/GaAs interface that allowed electron injection and carrier confinement in the Ge layer. The Ge layer was patterned into a 9  $\mu\text{m}$ -diameter disk, with a 6  $\mu\text{m}$ -diameter disk-shaped aluminum contact on the top. An annular-shaped Si-nitride layer was introduced to serve as the stressor layer, inducing a tensile strain in the GeNMs underneath. Notably, a 1.5 nm-thick  $\text{Al}_2\text{O}_3$  layer was deposited prior to the aluminum deposition to passivate the interfacial states between Ge and metals, thus leading to significant enhancements in carrier injection and electroluminescent efficiency [113]. According to the room-temperature electroluminescent properties of both unstrained and strained-Ge devices (not shown, and characterized with minimal current injection to avoid thermal heating), a spectral red-shift toward near-infrared light was clearly observed in the strain-engineered devices. The total red-shift was estimated to be 90 nm,

corresponding to an energy reduction of 43 meV, which corresponds to an equivalent transferred biaxial strain of about 0.55%.

Although room temperature photoluminescence [114], electroluminescence [112,113,115], and optical gain [116] have been realized from tensile-strain-engineered GeNMs, the most remarkable potential application for tensilely strained GeNMs could be a GeNM-based laser operating at room temperature for Si photonics. Liu et al. experimentally demonstrated room temperature lasing from a Ge-on-Si laser using an edge-emitting waveguide device [117]. It should be noted that only a 0.24% tensile strain can be thermally introduced into Ge when grown on Si, which shrinks the band gap but still cannot directly reach a direct band gap in Ge. *In situ* n-doping is therefore carried out to further compensate the energy difference between direct and indirect conduction valleys and enhance the light emission. Fabricated from tensile-strained  $n^+$ -Ge, the device consisted of trench-grown multimode Ge waveguides with mirror-polished facets, monolithically integrated on a Si wafer. A typical cross-sectional construction is revealed by SEM, as shown in Fig. 12(c) (inset). Once excited by a 1064 nm Q-switched laser with 1.5 ns pulse duration, pulsed edge emission was observed from the Ge waveguides. With a 1.5  $\mu\text{J}/\text{pulse}$ , the emission displayed a broad band with a maximum of about 1600 nm. When the excitation power increased up to 6.0  $\mu\text{J}/\text{pulse}$ , emission peaks emerged at 1559, 1606, and 1612 nm, with a shoulder appearing at 1594 nm. As the pump power reached 50.0  $\mu\text{J}/\text{pulse}$ , the widths of the emission peaks decreased significantly. Notably, the polarization evolved from a mixed transverse magnetic/transverse electric (TM/TE) mode to a predominantly TE mode due to the increase of optical gain, which was expected as a typical lasing behavior. A high-resolution scan of the emission line was performed at 1593.6 nm, as shown in the

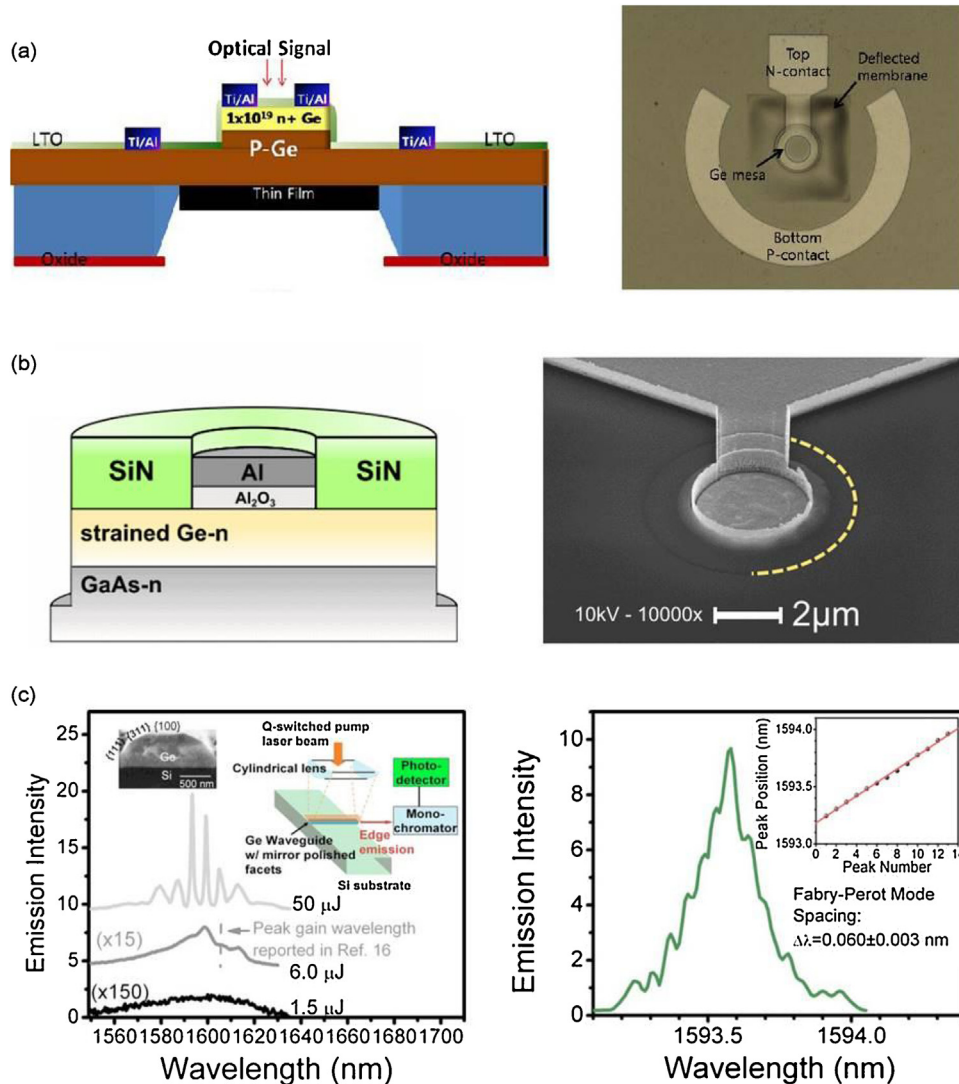


**Fig. 12.** (a) Schematic diagram and optical-microscopy image of strained-Ge membrane-based PN photodetector [111]. (b) Schematic diagram and SEM image of the tensile-strained Ge microdisk diode with disk-shaped contacts [112]. (c) Left: edge-emission spectra of a Ge waveguide with mirror polished facets from a Q-switched laser with 1.5, 6.0, and 50  $\mu$ J/pulse pumping power. A cross-sectional SEM image of the device and a schematic drawing of the experimental setup for optical pumping are shown in the inset. Right: high-resolution scan of the emission line at 1593.6 nm, indicating the existing of longitudinal Fabry-Perot modes. (c) reprinted from [117].

right panel of Fig. 12(c). Periodic peaks corresponding to longitudinal Fabry-Perot modes were clearly observed, which is consistent with related works on III-V semiconductor lasers [118,119]. The inset with a linear fit indicates a longitudinal mode spacing of  $0.060 \pm 0.003$  nm, agreeing well with the calculated mode spacing of 0.063 nm. Considering Ge has been widely exploited in Si-based CMOS electronics and integrated photonic devices, tensile-strained-GeNMs are surely desirable for high-performance optoelectronic devices.

### 5. 3D assembly by strain engineering

In the last section, we reviewed strategies and applications for strain-engineered 2D Si/GeNMs, which involve *in-plane deformation* induced by lattice constant variations. In this section, we discuss another type of strain engineering of Si/GeNMs, called *out-of-plane deformation*, which leads to a geometric transformation from 2D NMs into 3D micro/nano-structures. It is possible to force a NM to deflect vertically if the boundary conditions limit its lateral deformation. The driving force for geometry transformation can be provided from either internal strains existing in multilayers of NMs

or external mechanical stress. The release of the internal strains or external stress under certain conditions will induce bending, rolling, wrinkling, folding, or buckling of these flexible Si/GeNMs, thus forming shape-controllable 3D micro/nano-architectures. Driven by the release of internal strains, 2D Si/GeNMs can, for example, be shaped into 3D micro/nano-tubes, helices, or wrinkles, which may be referred to as rolled-up [120–122] or wrinkled-up [123], depending on the geometry, orientation, and thickness of the bi/multi-layers [124–127]. In addition, after integrating unstressed Si/GeNMs with pre-stressed flexible elastic support substrates, NM-based 3D micro/nano-architectures, including wrinkles [15,81,128], buckles [16,17], and mesostructures [14], can be achieved by releasing the external stress of the substrates. The principles and controllability for shaping planar NMs into micro/nano-structures will provide great opportunities for the development of nanoscience and nanotechnology.

#### 5.1. Rolled-up nanotechnology

Rolled-up nanotechnology has proven to be a convenient and controllable approach for rearranging NMs into micro/nanoscale

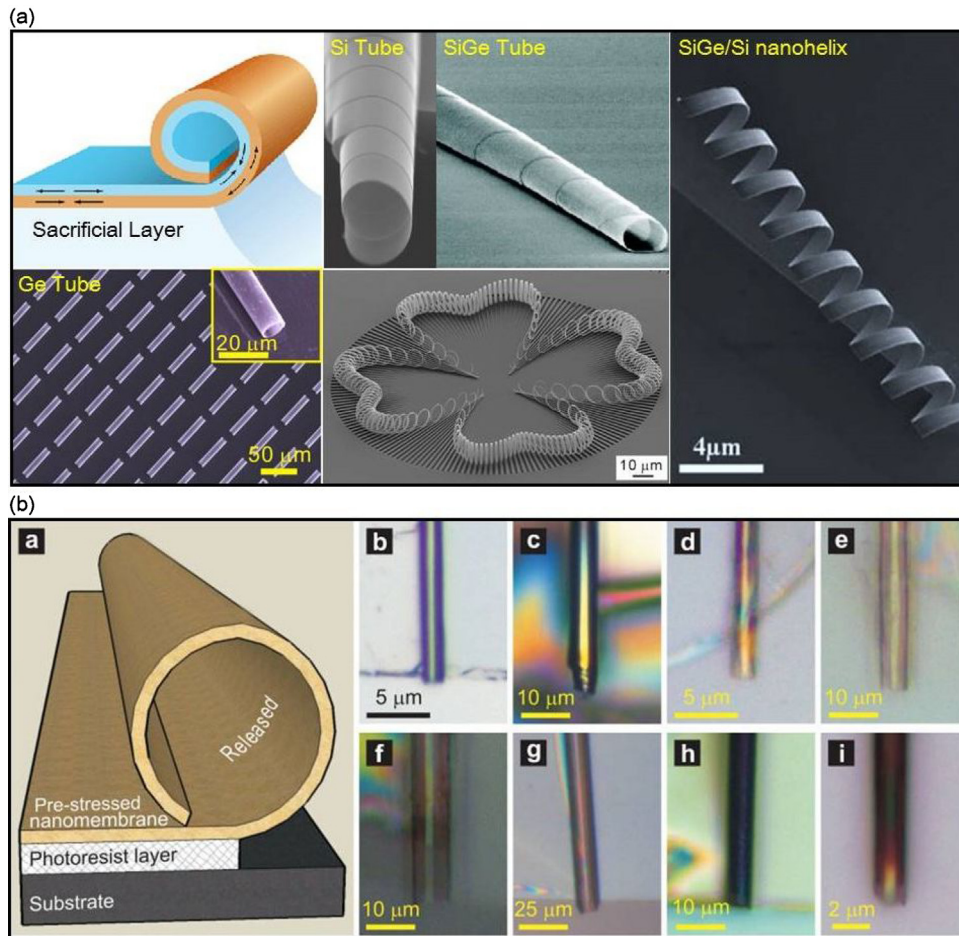


**Fig. 13.** (a) Schematic diagram of rolled-up nanotechnology. State-of-the-art Si/GeNM-based 3D micro/nano-architectures realized via rolled-up nanotechnology. SEM images from Refs. [140,143,144,135,153]. (b) Schematic diagram of the rolling-up process of a NM on a polymer sacrificial layer. Optical images of rolled-up microtubes made of Pt, Pd/Fe/Pd, TiO<sub>2</sub>, ZnO, Al<sub>2</sub>O<sub>3</sub>, Si<sub>x</sub>N<sub>y</sub>, Si<sub>x</sub>N<sub>y</sub>/Ag, and diamond-like carbon NMs, respectively [13].

tubes, helices or other complex structures [120–122]. In order to obtain rolled-up micro/nano-tubes or -helices, it is necessary to build a strain gradient perpendicular to the NM. As shown by the schematic diagram in Fig. 13(a) [129], a pre-strained bi-layer with opposing strain direction (top, tensile; bottom, compressive) is grown on a sacrificial layer. Selective etching of the sacrificial layer will release the pre-strained bi-layer. Driven by the built-in forces, the released part of the bi-layer will self-roll into a tubular structure. For Si/GeNMs, the strain gradient can be generated by utilizing a lattice mismatch in the epitaxial bi-/multi-layers [124,130–135], or by introducing another stressor layer on the top, e.g., chromium (Cr) [134–141], or tungsten (W) [142]. The strain gradient is tunable by the experimental parameters during deposition, i.e., composition, thickness, rate, temperature, etc. As a result, the diameter of the tubes can be manipulated. By constructing a bi-/multi-layer with the proper strain gradient, single-crystalline Ge tubes [140], Si tubes [143], and their composite (SiGe) tubes [144] have been demonstrated, as shown by the SEM images in Fig. 13(a).

Recently, researchers further developed roll-up nanotechnology by exploring a versatile approach for fabricating rolled-up micro/nano-tubes consisting of a number of inorganic materials and their combinations, ranging from conductors and semiconductors to insulators. As exhibited in Fig. 13(b), a pre-stressed NM was deposited on a photoresist sacrificial layer. Notably, the pre-stress in deposited NMs could be introduced and influenced by thermal expansion mismatch between NMs and sacrificial layers,

deposition rate, and stress evolution during deposition [13]. After selective removal of the sacrificial layer with acetone or other organic solvent, the pre-stressed NM released and rolled up to form tubular structures [13]. The significant advantage here is that the sacrificial photoresist layer can be removed by acetone over any inorganic NM with a selectivity of almost 100%. Therefore, various inorganic-material-based micro/nano-tubes can be realized by this versatile roll-up approach, for example, Pt, Pd/Fe/Pd, TiO<sub>2</sub>, ZnO, Al<sub>2</sub>O<sub>3</sub>, Si<sub>x</sub>N<sub>y</sub>, Si<sub>x</sub>N<sub>y</sub>/Ag, and diamond-like carbon, as demonstrated in Fig. 13(b). In addition, the patterning of photoresist can be performed with conventional photolithography to provide convenience in the geometric design of precursors (here: pre-stressed NMs) and module integration on a single chip [13]. This universal approach can also be exploited for fabricating Si/GeNM-based tubular structures [145,146]. For instance, Yan et al. constructed hybrid multilayer Ge/Ti NMs on a photoresist sacrificial layer where the Ti acted as the stressor [146]. Removal of the polymer layer in acetone induced self-rolling of the hybrid multilayer, thus forming GeNM-based tubes, which were further explored for highly efficient lithium-ion batteries. Other recently emerging materials/structures, such as graphene [147,148], diamond [149], rocket-inspired tube [150], and 2D transition-metal dichalcogenide (e.g., MoS<sub>2</sub>, WS<sub>2-x</sub>, and WSe<sub>2-x</sub>) [151,152] based nanotubes have also been theoretically and experimentally demonstrated by rolled-up nanotechnology.

It is worth noting that the features of rolled-up micro/nano-structures are strongly determined by the dimensions and/or

orientations of the pre-stressed layers [124–127]. Si and GeNMs, having cubic crystal structures, will self-roll along the  $\langle 100 \rangle$  direction where the Young's modulus is small [135,140]. Taking advantage of the crystalline-orientation dependence and geometric-aspect ratio, various complex rolled-up nanostructures like tubes, rings, helices, and spirals can be realized by tailoring the shapes and alignment relative to the  $\langle 100 \rangle$  direction of the pre-stressed precursors [125]. For instance, if the pre-stressed Si/GeNMs are shaped into strips along the compliant  $\langle 100 \rangle$  direction, micro/nano-rings or tubes will be formed by rolling-up [124,140]. However, if the shaped strips are misaligned with the  $\langle 100 \rangle$  direction, the NM will form helical structures, as shown in the right panel of Fig. 13(a). This rolling principle can break down when the width of the shaped strips is sufficiently small. Zhang et al. have developed a theoretical model to predict the rolling direction depending on strip line or compliant orientation in SiGe/Si/Cr and SiGe/Si systems [135]. It is known that part of the stress existing in strained strips will relax at the edges [154]. Due to this relaxation effect, strips with isotropic pre-strain that are narrow enough can be considered uniaxially strained along the longitudinal axis. Therefore, the stress along the longitudinal axis will become dominant, with the rolling direction near the strip longitudinal axis instead of the  $\langle 100 \rangle$  direction, as depicted in middle-bottom panel in Fig. 13(a) with the initial wagon-wheel pattern [135].

### 5.2. Wrinkled-up nanotechnology

By properly designing the strain gradient, average strain value, and the etching depth for the selective release of pre-stressed NMs, another type of 3D micro/nano-structures can be realized, i.e., wrinkles [155–157]. This approach is here termed as “wrinkled-up nanotechnology,” and consists of partial release, wrinkling, and bonding back onto the substrate surface [123], as schematically demonstrated in the top panel of Fig. 14(a). After the selective removal of the sacrificial layer in a proper chemical solvent, morphological variations observed in the pre-stressed NMs can be attributed to liquid surface tension-driven bonding-back effects during the drying process. As a demonstration, the surface of SiGe on a  $\text{SiO}_2$ -Si (001) substrate was exposed to hydrofluoric acid. The oxide layer was partially removed through pre-defined trenches until a certain lateral distance was reached. Driven by compressive strain, the SiGe layer detached from the substrate, wrinkled, and finally formed into a linear nanochannel network. A typical optical-microscopy image of this is shown in the bottom panel of Fig. 14(a). Moreover, the size of SiGe wrinkles is easily scalable to form nanoscale channel networks, which have been demonstrated to act as efficient fluid suppliers and injectors [123]. Wrinkled  $\text{Si}_{1-x}\text{Ge}_x$  bilayer NMs can also be realized on Si substrates [158–161], where the Si buffer layer is selectively removed by a standard semiconductor process.

It is known that for a given SiGeNM, the size (e.g., wavelength and amplitude) of the strain-induced wrinkle is determined by the initial strain value and lateral length [162]. An initial biaxial compressive strain in SiGeNMs can be tuned by the Ge content during growth, while the lateral length can be controlled by the etching time. Increasing the lateral length of the NM increases both wavelength and amplitude due to the increase of the total strain energy. Increasing the initial strain in the NM, however, decreases the wavelength and increases the amplitude for a fixed lateral length.

In addition to dimensions, the order and position of wrinkled-up structures can be deterministically assembled. By specially designed patterns of pre-stressed NMs, the etching front can be started at pre-determined points to lead to designed wrinkling behavior. As demonstrated in the top panel of Fig. 14(b), the number of wrinkles formed in circular networks is set by well-defined patterns in pre-

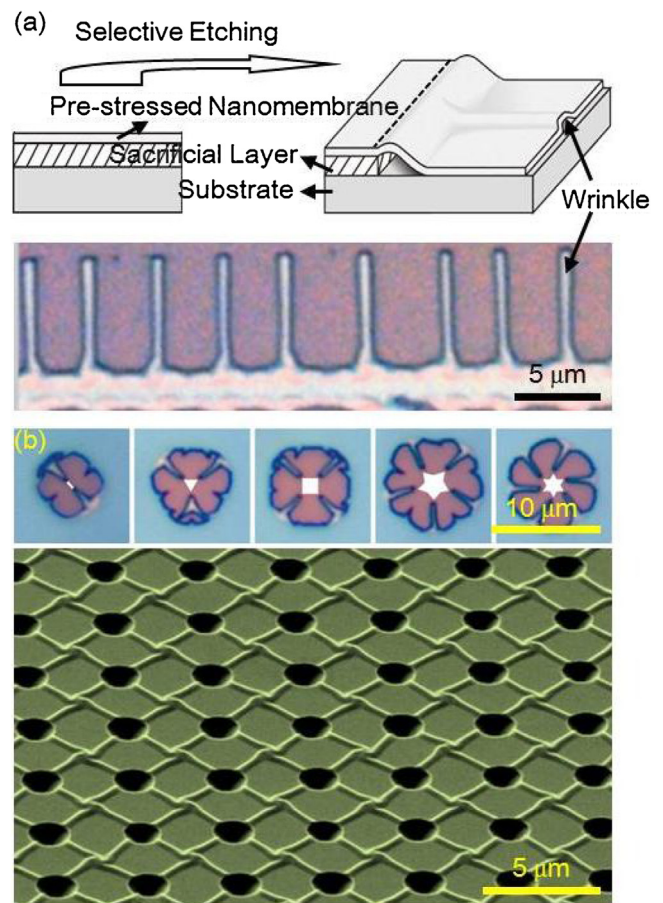


**Fig. 14.** (a) Schematic illustration of the formation of the wrinkle/nanochannel structure by selective removal of the sacrificial layer [123]. A typical optical-microscopy image of a SiGeNM-based linear nanochannel network is displayed at the bottom [123]. (b) Top panel: optical images of circular networks with 2–6 well-positioned branch channels. They are transformed from lithographically defined patterns from left to right: short line, triangle, square, and five- and six-pointed stars [123]. Bottom: large-area wrinkle-based nanochannel networks [163].

stressed NMs, such as short line, triangle, square, and five- and six-pointed stars [123]. Accordingly, the position of the wrinkle is exactly confined to the corners of the initial shapes. Based on this concept, large-area wrinkle-based nanochannel networks with uniform spatial arrangements are created by introducing small squares into pre-stressed NMs [163], as shown in the bottom panel of Fig. 14(b). Besides Si, Ge, and SiGe-alloy NMs, this wrinkled-up nanotechnology can also be used to fabricate other inorganic-semiconductor NM-based wrinkles, especially for III-V materials, as the in-plane strain value and thickness can be easily tuned during the deposition [164]. As a demonstration of the power of wrinkling to influence useful properties, a quantum well of InGaAs NMs sandwiched between two GaAs barrier layers was released and formed into wrinkled nanostructures, with significant light-emission enhancement [165].

### 5.3. Principles of rolling or wrinkling?

As we discussed in last two subsections, both rolled-up and wrinkled-up micro/nano-structures can be realized according to pre-defined strain engineering, which involves the releasing and self-assembly of pre-stressed NMs. The built-in strain gradient across the NM vertical direction sensitively determines whether a NM rolls up or wrinkles up [127]. In general, if the strain gradient is large, the NM initially bends and finally forms into a rolled-up tube.

For small or zero strain gradients, however, wrinkled-up structures are prone to form. The particular shapes formed by releasing pre-stressed NMs by minimizing the total strain energy, can be theoretically predicted. An equilibrium-phase diagram for the shape as a function of etching depth ( $h$ ) and strain gradient ( $\Delta\epsilon$ ) has been developed and shown in Fig. 15 [127]. For a small strain gradient of 0.2% and average strain ( $\bar{\epsilon}$ ) of  $-0.36\%$ , bending is only favored until the etching depth ( $h$ ) reaches 700 nm. Further increasing the etching depth makes wrinkling dominant in the releasing process. In large average-strain conditions, e.g.,  $\bar{\epsilon} = -1\%$ , the boundary between bending and wrinkling will move upwards, leading to an enlarged wrinkling area. Additionally, the radius of the curved shape decreases when the strain gradient increases; no obvious relationship with the etching depth can be found. The opposite conclusion can be found with wrinkling regions, where the wavelength of the wrinkles can be significantly affected only by the etching depth.

In fact, the rolled-up and wrinkled-up states of pre-stressed semiconductor NMs after their elastic relaxation may be independent as mentioned above, or also correlated. More recently, the coexistence of rolled-up and wrinkled-up morphologies has been achieved in semiconductor NMs with proper strain engineering [164]. Additionally, preferential rolling directions of strain-relaxed NMs with initially designed wrinkles have been demonstrated to be strongly dependent on the wrinkle geometry (e.g., amplitude) and strain gradient [166]. In brief, by utilizing the rolled-up or wrinkled-up nanotechnologies that involve the strain relaxation of pre-stressed Si/GeNMs, various micro/nano-architectures, such as tubes [130–132,138,139,167], rings [137,167,168], coils [124,133], springs [169], helices [134,136,153,167,170], wrinkles [123,155,165], and wrinkle-based nanochannels [163], can be achieved. Compared with their initial 2D forms, 3D NMs possess remarkable mechanical, electrical, optical, and thermal conductivity properties, which will be reviewed later.

#### 5.4. Compressive Wrinkling/Buckling

As we discussed in the last three subsections, Si/GeNMs can form into 3D micro/nano-architectures by rolled-up or wrinkled-up nanotechnology, which is driven by the releasing of built-in

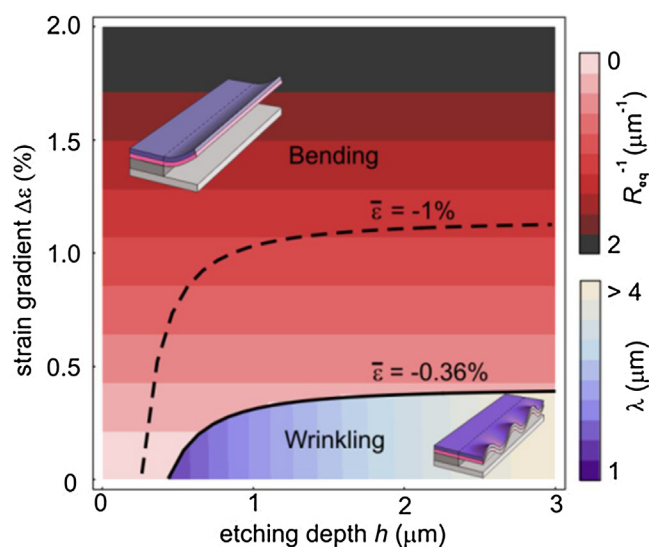


**Fig. 15.** Phase diagram of favored shapes based on energy comparisons between bent and wrinkled structures. The radius  $R_{eq}$  and wavelength  $\lambda$  are shown for rolled-up and wrinkled-up structures, respectively. Solid and dashed curves show the phase boundaries between bending and wrinkling under different average-strain conditions. Reprinted from Ref. [127].

strain. In the following subsections, 3D Si/GeNM-based structures induced by external mechanical compressive stress will be reviewed. Owing to their superior flexibility, as we discussed in Subsection 2.5, Si/GeNMs can be shaped into wrinkles or wavy structures [15,81,128], buckles [16,17,171], and mesostructures [14,172,173], by external mechanical compressive stress, mainly generated by the releasing of the pre-stressed flexible substrate. The primary motivation for developing compressive 3D buckles based on Si/GeNMs is to enable and extend the flexibility of electrical devices and systems from bendable to stretchable [54,174]. These buckled or wrinkled structures occur to accommodate the external compressive or tensile strain through changing buckle or wrinkle wavelengths or amplitudes [6,175].

As shown in Fig. 16(a), the top Si (or Ge) NM of a SOI (GOI) mother wafer is defined, patterned and released by photolithography, RIE, and selective chemical wet etching, respectively [15]. Then a tensilely pre-stressed elastomeric substrate (e.g., PDMS) is put onto the top of the released Si (Ge) NM to form intimate contact. Rapidly peeling back the elastomer will induce the detachment of NMs from the mother wafer, and transfer them onto a pre-stressed elastomeric substrate. Finally, 3D wrinkled Si/GeNMs are formed by releasing the substrate, as exhibited in the bottom panel of Fig. 16(a) (sketched) and 16(b) (SEM image).

One can see from the schematic diagram in Fig. 16(a), the elastomeric substrate is uniaxially pre-stressed; therefore, the Si/GeNMs uniaxially wrinkle along the stress direction of the substrate. Another stretchable form of large-area Si/GeNMs (e.g., 3–5 mm square) that consists of two-dimensional buckles or wrinkles on elastomeric supports is achieved [176], as demonstrated in Fig. 16(c). Unlike the aforementioned one-dimensional wrinkling geometry, the two-dimensional wrinkling geometry discussed here can provide full 2D stretchability. In addition, large-area 2D Si/GeNMs can be pre-designed with specific patterns, and then transferred onto pre-stressed elastomeric substrates to form controllable and uniform 3D structures. As proven in Fig. 16(d), uniformly distributed buckles are localized and interconnected in a near-checker board SiNM-based pattern [177], which was achieved by pre-designing and releasing.

One of the most prominent advantages of the compressive buckling technique in fabricating 3D Si/GeNM-based wavy structures (with a fixed thickness) is that the dimensions (e.g., wavelength and amplitude) can be specified simply by changing the original strain values of the elastomeric substrates, which can be realized by thermal stretching [176,178], mechanical stretching [179–183], swelling [177], or electrical stimulation [184]. Other materials, such as dielectric elastomers [185], or polystyrene, can also serve as the substrates for the formation of wrinkles. Taking polystyrene film as an example, when the temperature increases beyond the glass transition point ( $95^\circ\text{C}$ ) but below the melting temperature ( $240^\circ\text{C}$ ), its dimensions will shrink, except for the thickness, which increases [156]. Therefore, a variety of wrinkles can be directly generated by depositing electronic thin films on polystyrene substrates [186–188].

Of course, this compressive buckling technique is not limited to fabrication with Si/Ge-based NMs. Other materials, either in 1D wire form or 2D planar thin films with flexibility can also be shaped into wrinkled or buckled structures, including conductors, semiconductors, and dielectrics, such as 1D Si nanowires [189,190] or carbon nanotubes [191,192]; 2D planar ultra-thin membranes of GaAs [102], InGaAs [193], ZnO [194,195],  $\text{ReSe}_2$  [196], lead zirconatetitanate (PZT) [197], indium-tin-oxide (ITO) [198], Au [184,199], Ag [200], Pt [201], and  $\text{Al}_2\text{O}_3$  [202]. In addition, recently burgeoning 2D layered materials such as graphene [203–206] and  $\text{MoS}_2/\text{WS}_2$  [190,207] have also been shaped into wrinkles, which exhibit great potential for applications in strain sensors, optoelectronics, and band structure strain engineering [208].

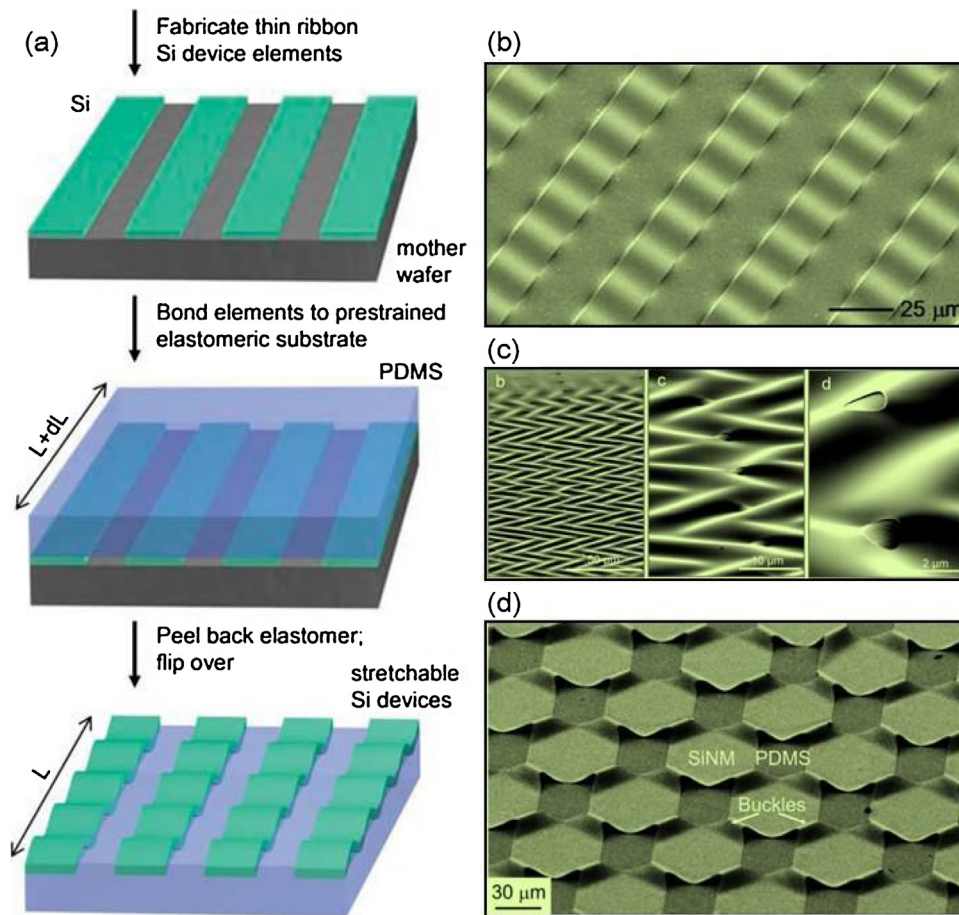


**Fig. 16.** (a) Schematic illustration of the fabrication process for stretchable single-crystalline Si devices on elastomeric substrates [15]. (b) SEM image of four uniaxial wavy Si ribbons with highly uniform wavelengths and amplitudes [15]. (c) SEM images of biaxial wavy SiNMs on PDMS. The thickness of the NMs and the pre-strain of the PDMS are 100 nm and 3.8%, respectively [176]. (d) SEM image of the delaminated buckle array interconnected in a near-checker board pattern [177].

### 5.5. Popped-up mesostructures

For the conventional compressive wrinkling/buckling process, the vertical deformations are normally in a bending manner (e.g., wrinkles or buckles in Subsection 5.4), and the deformation dimensions are generally within several or tens of micrometers. Recently, Si micro/nanomembrane-based complex architectures with more tri-dimensional geometries, regarded as popped-up mesostructures, have been widely developed [14,172,209–216]. As shown in Fig. 17(a), the popping-up process begins with integrating 2D serpentine-shaped Si membranes onto an extremely stretched silicone substrate (e.g., Dragon Skin; Smooth-On, Easton, PA; the pre-strain of silicone is about 70% for the case shown here). Except for the bonding sites that involve strong, spatially selective bonding via covalent linkages, the interactions at all other locations are dominated by weak van der Waals forces. Once the substrate returns to its original length, a large compressive strain will be induced and applied to the serpentine precursors. Therefore, a controlled popping-up process that lifts the weakly bonded regions of the serpentine SiNM off contact with the surface will be initiated, leading to spatially dependent twisting/bending deformations and in-/out-of-plane translations [14]. A representative example of a popped-up helical mesostructure is presented at the lower right of Fig. 17(a).

In principle, the mechanically guided, deterministic popping-up process that involves geometric transformations from 2D to 3D is dominated by (i) the 2D layout dimensions and mechanical properties of the precursor materials; (ii) the locations of the

covalent bonding sites; and (iii) the nature and magnitude of the pre-strain in the elastic target substrate [14]. With this scheme, widely ranging feature sizes (from sub-micrometer to meter scales) and diverse 3D mesostructures can be realized by designing the 2D precursor geometries, bonding sites, and stretching configurations. Several examples of interconnected 3D mesoscale networks are shown in Fig. 17(b), which may be referred to as an array of tents with a spatial gradient in the height, mixed array of tents and tables, double-floor helixes, and three-layer flower, from top to bottom.

Recently, J. A. Rogers, Y. G. Huang and their collaborators pointed out that these 3D mesostructures induced by releasing the stress of pre-strained elastomer substrates can be regarded as pop-up origamis, possessing some similarities to the mechanisms in pop-up books [210]. The classes of 3D mesostructures can be further broadened by patterning the 2D precursor in a form of kirigami, an ancient aesthetic pursuit that involves strategically designed shapes and patterns of cuts to guide the pop-up process [209]. In particular, the use of multilayer 2D precursors gives more possibilities for obtaining complex 3D multilayer mesostructures [213]. Other strategies for the guided assembly of complex 3D mesostructures have been pursued, including varying the thickness of the 2D precursors [212], spatially and non-uniformly popping-up processes [217], residual stress-assisted deterministic assemblies [218], pre-patterned 1D or 2D elastomer substrates [171,219], and the capillary-driven self-folding of single-crystalline Si membranes [220]. Owing to the material's unique physical and chemical properties, Si/Ge micro/nanomembrane-based 3D

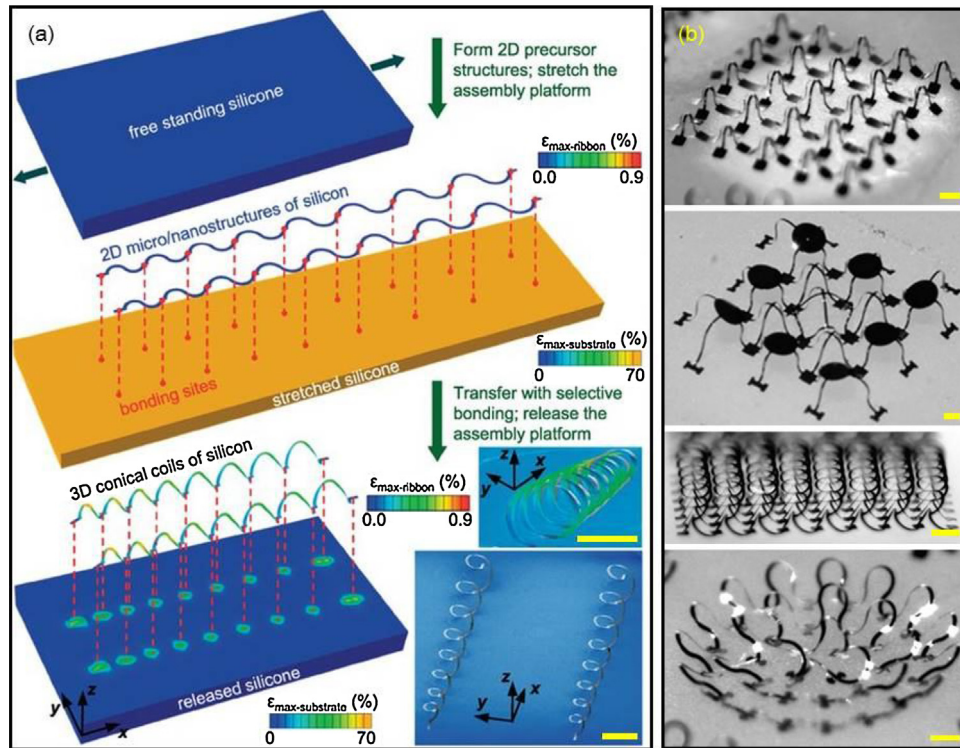


**Fig. 17.** (a) Process for assembly of 3D Si membrane-based mesostructures from 2D precursors. Finite element analysis (FEA) results of 3D conical helices formed from 2D Si filamentary serpentine ribbons, which bond selectively (red dots) with a stretched silicone elastomer. 3D Si membrane-based mesostructures that involve coordinated out-of-plane buckling, twisting, and translational motions are formed by compressive forces induced by relaxing the strain in the elastomer. SEM images at the lower right show typical experimental results. (b) Demonstrations of 3D mesostructures with multilevel configurations and/or extended network architectures. Optical micrographs of an array of tents, mixed array of tents and tables, double-floor helices, and three-layer flower, from top to bottom. Scale bars, 200  $\mu\text{m}$  (a), 400  $\mu\text{m}$  (b). Reprinted from Ref. [14]. (For interpretation of the references to colour in this figure legend, the reader is referred to the web version of this article.)

origami/kirigami can be pursued to make building blocks for applications in actuators, sensors, energy storage, light manipulation, flexible/stretchable electronics, bio-platforms, and biomedical devices.

## 6. Properties and applications for 3D strain-engineered Si/GeNMs

### 6.1. Properties

Si/GeNMs in 3D strain-engineered micro/nano-architectures, induced by the release of internal strain or external stress, offer opportunities in both basic science and advanced applications, owing to their unique and engineerable features, which are unavailable with 2D planar geometries. Fig. 18 summarizes representative examples of the physical properties of 3D rolled-up Si/GeNMs in mechanics, thermoelectrics, electronics, and optics. For instance, a mechanical property of a SiGe/Si/Cr nanohelix is estimated by stretching it between an AFM tip and a tungsten probe. The sequential elastic deformation and recovery processes under tensile loading and unloading are captured by SEM. Corresponding micrograph illustrations are found in Fig. 18(a) [153]. The nanohelix can be elongated to more than 170% of its initial length without any plastic deformation, as demonstrated by the recovery process. The dependence of the elongation of a nanohelix on the tensile load is investigated experimentally and theoretically, as shown in the top right panel of Fig. 18(a). The linear relation between the load and elongation can still be observed as the helix is stretched to approximately 189%, indicating the superior elastic properties of the 3D nanohelix, which is unavailable for its 2D planar precursor. The spring

constant versus elongation within the entire stretching region of the nanohelix is calculated and shown in the bottom right panel of Fig. 18(a), in which the spring constant  $k$  is a constant in the linear region with the average value of  $5.5 \times 10^{-3}$  N/m, and reaching a critical value of  $1.4 \times 10^{-1}$  N/m in the high-loading region before fracture.

3D rolled-up microtubes offer distinct advantages in fabricating 3D stacked multilayer systems by the mechanical compression technique [223], which involves vertical pressing on the rolled-up tube, leading to the formation of a 3D stacked superlattice. Its mechanical interfaces have weak bonding and imperfect contact; therefore, the thermal conductivity is distinctly affected [224]. For a Si superlattice formed by pressing back the rolled-up SiNM, a visible reduction in thermal transport of more than 2 orders of magnitude can be observed compared with either the handle wafer (bulk Si) or planar NMs (unreleased single layers of Si), as demonstrated in Fig. 18(b) [221]. This technique allows the convenient integration of single layers of Si/Ge into 3D stacked superlattice constructions, which could exhibit significant potential for thermoelectric generators.

The geometry transformations from 2D NMs to 3D rolled-up tubular structures also strongly affect their electronic properties, as shown in Fig. 18(c) [141]. In contrast to unreleased Si/GeNMs, where the bottom surfaces are passivated by the sacrificial layer, a high density of surface states will be formed at both the outer and inner surfaces of the tube wall after releasing [131,141]. Therefore, the effective conducting layer will shrink due to surface-charge trapping, resulting in decreased electrical conductivity. In addition, the unique tubular structure is expected to be an optically resonant microcavity, where light efficiently couples out perpendicular to the substrate surface [222,225–227]. Taking rolled-up SiO/SiO<sub>2</sub>

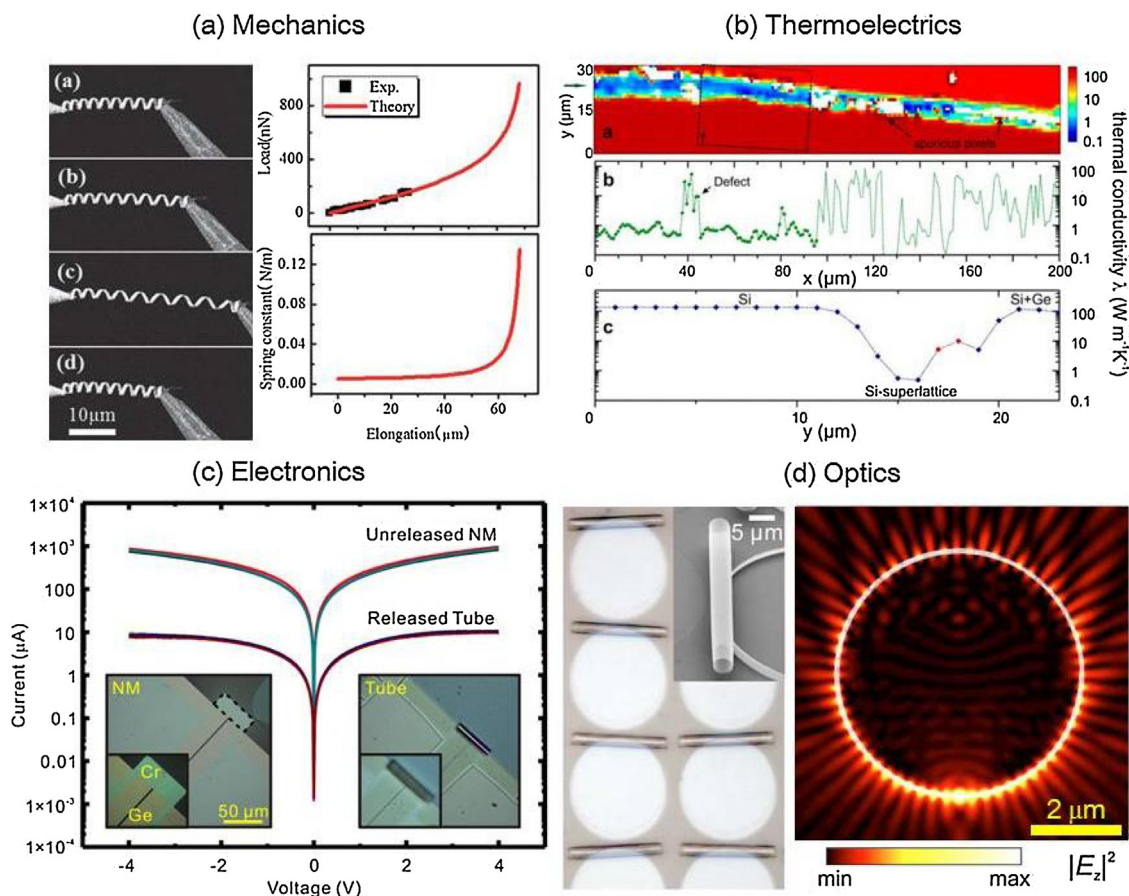


**Fig. 18.** Unique physical properties of Si/GeNMs in rolled-up 3D structures: (a) mechanical property of a SiGe/Si/Cr nanohelix between an AFM cantilever and tungsten probe [153]; (b) time-domain thermoreflectance (TDTR) maps of a Si superlattice obtained by applying vertical pressure onto a rolled-up Si tube [221]; (c) electrical characteristics of unreleased GeNMs and released Ge tubular resistors [141]; (d) optical-microscopy and SEM (inset) images of ordered Si-based ( $\text{SiO}/\text{SiO}_2$  NMs) microtubes, and the intensity pattern of the electric field for a typical rolled-up tube in the mode  $M = 30$  [222].

microtubes as an example, the electric field intensity pattern for a representative mode ( $M = 30$ ) is shown in Fig. 18(d) [222], indicating the strong localization of light in the tube wall as whisper gallery modes (WGM) [228–231]. The superior optical properties of rolled-up Si/GeNM-based tubular microcavities [232], which are tunable by the geometries, rotations, thicknesses, and materials, offer opportunities for applications in the areas of optofluidics [233] and nanophotonics [234], as well as bio/chem-sensitics [226].

3D Si/GeNM-based micro/nano-architectures (wrinkles, buckles, and popped-up mesostructures), induced by external mechanical compression, possess remarkable features such as being strain-engineerable, stretchable, and tunable by light manipulation, as summarized in Fig. 19. Because 3D micro/nano-architectures, transformed from 2D planar precursors, experience the movements of bending, twisting, and/or folding, it is obvious that strain can be engineered into them in a self-assembly manner due to the general bending effect [235,236]. As a demonstration, Fig. 19(a) shows the color-coded Raman-peak positions (Si–Si TO phonons) extracted from the mapping measurements of a Si wrinkle with two different excitation lasers (514 nm and 325 nm in wavelength) [81]. The peak positions exhibit periodic alternation (equal with the wavelength of the wrinkle) along the x direction while keeping constant along the y direction, which indicates that a periodic strain distribution was engineered into them. Similar results are also demonstrated in rolled-up Ge tubes [140], III–V semiconductors [237–239], and

wrinkled III–V NMs [102,165], where the engineered strains are recorded by polarized Raman scattering spectroscopy, x-ray micro diffraction, or photoluminescence.

A remarkable feature of wrinkled NMs (including, but not limited to, Si/Ge) is mechanical stretchability, which accommodates external compression and tensile strain through changing wavelengths and amplitudes [180,240]. Fig. 19(b) provides experimental results and theoretical predictions for the relationships between the geometry (including wavelength and amplitude) and the applied strain for a buckled Si-membrane/PDMS system. Increasing the applied strain increases the wavelength. In contrast, the amplitude decreases, even reaching zero once the applied strain reaches a critical value (here 16.2%, equal with the pre-strain for fabricating Si buckles) [180]. Continuously increasing the tension in SiNMs will result in fracture, typically at about the 1%-level for active materials under bending [15]. Therefore, the superior stretchability of 3D Si/Ge wrinkles/buckles, which is unavailable to the 2D planar forms, can be exploited as building blocks for applications in flexible/stretchable electronics.

The wrinkled/buckled geometry also strongly influences and manipulates light absorption in the NM, enhancing the light-extraction efficiency [241] or reducing reflectivity by light-trapping [242] or scattering effects [243]. Light absorption in GeNMs and wrinkles, for example, can be simulated by the finite element method [128]. Fig. 19(c) shows a cross-sectional view of the electric-field distributions in a 2D flat GeNM and a 3D Ge wrinkle on a PDMS substrate. Typical scattering is demonstrated

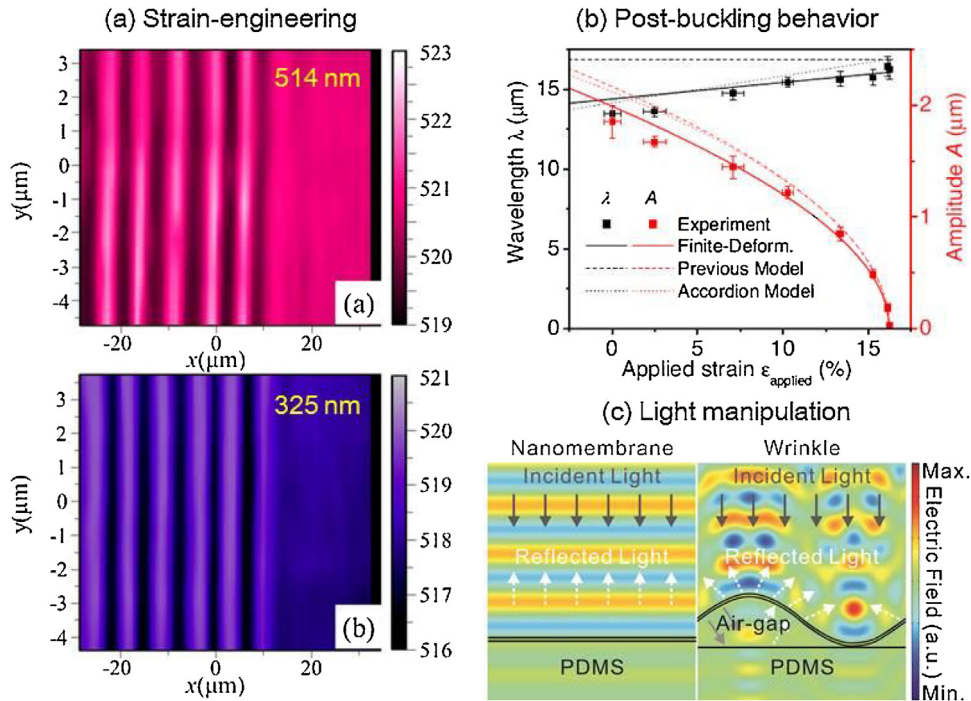


**Fig. 19.** (a) Investigation of strain engineering into wrinkled SiNMs through micro-Raman mapping. Raman-peak position distributions obtained by two excitation lasers with different wavelengths (top: 514 nm; bottom: 325 nm) [81]. (b) Experimental and theoretical results for the post-buckling behavior of wrinkled SiNMs exhibited by the geometries (wavelength and amplitude of the wrinkles), varying with the applied strain values [180]. (c) Simulated results of the electric field distributions for planar and wrinkled GeNMs [128].

by the Ge wrinkle, which can be attributed to the wavy surface, thus inducing significant changes in the propagation directions of the light [128,243]. Therefore, the light path in the wrinkles' active material is extended, leading to more light absorption than the planar NM.

## 6.2. Applications

3D strain-engineered Si/GeNMs open up opportunities for practical applications that would be unavailable with conventional 2D planar Si/GeNMs. The unique 3D geometries, coupled with their

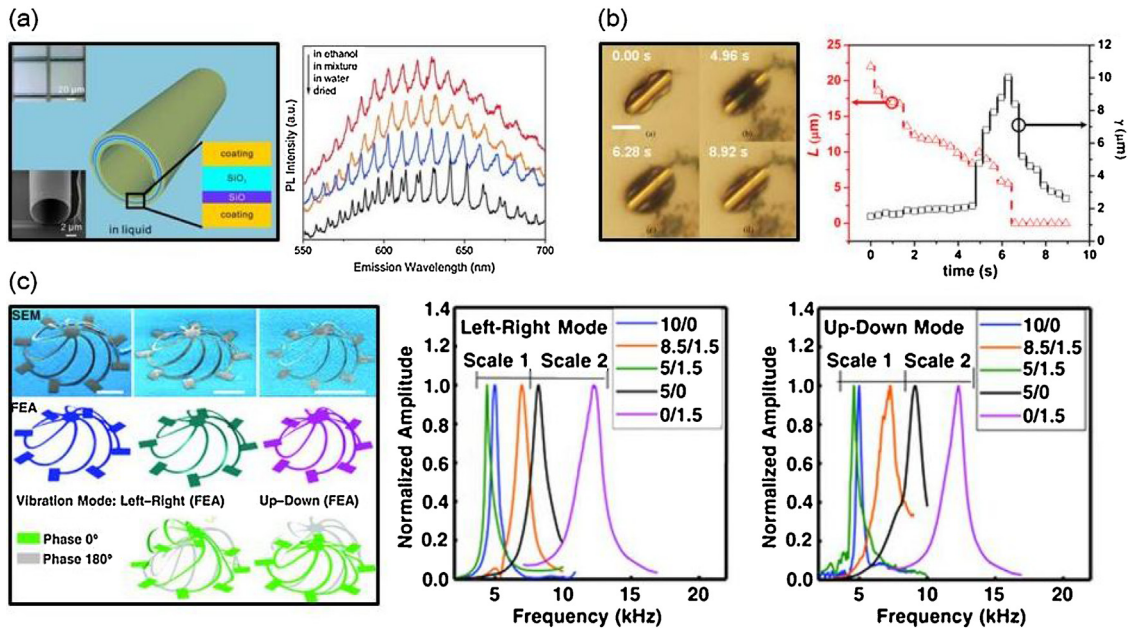


**Fig. 20.** (a) Schematic diagram of a rolled-up tubular structure in liquid. The bottom-right inset illustrates the multilayer structure of the tube wall; the top-left and bottom-left insets show the optical-microscope and SEM images of the rolled-up tube. On the right, the PL spectra are shown of a rolled-up microcavity in different surrounding conditions, including air, water, ethanol, and a water/ethanol mixture (1:1 in volume). Reprinted from Ref. [248]. (b) Optical images of a rolled-up tube with different acetone-evaporation periods and acetone wetting lengths.  $L$ , inside the tube, and the tube opening gap  $\gamma$ . Scale bar is 10  $\mu\text{m}$ . Reprinted from Ref. [132]. (c) Left: SEM images and finite element analysis (FEA) simulations of popped-up cage mesostructures comprised of SU-8 photoresist, SU-8/Si bilayer, and Si. Two vibrational modes of left-right and up-down are inserted in the bottom. Scale bar is 500  $\mu\text{m}$ . Middle and right: amplitude-frequency responses in two types of vibrational modes (i.e., left-right and up-down) for popped-up cage mesostructures with various combinations of SU8 and Si thicknesses. All scale bars are 500  $\mu\text{m}$ . Reprinted from Ref. [216].

superior mechanical, electrical, and optical properties, provided by Si/Ge-based micro/nano-architectures, imply potential for dramatic areas of application in various fields. Therefore, various demonstrations of advanced devices have been reported in the format of 3D NMs. In the following parts, we will summarize the most intriguing application areas of 3D Si/Ge micro/nano-architectures.

### 6.2.1. Sensors and transducers

Emerging applications available to 3D Si/Ge micro/nano-architectures are as sensors and transducers, in which their responses to changes in surrounding conditions are demonstrated by changes in the architecture/topography or properties of the NM that can be measured. The capability of an optofluidics sensor to distinguish the fluids inside a tubular microchannel according to the optical resonance spectral-peak position shifts [244–247] is shown schematically in Fig. 20(a) [248]. Si-based tubular optical microcavities were fabricated via the rolled-up technique, coated with an additional oxide layer on both the inner and outer surfaces, and immersed in liquid. Their PL spectra were obtained under different ambient-liquid conditions, including air, water, ethanol, and a water/ethanol mixture (1:1 in volume). The respective results are summarized in the right panel of Fig. 20(a), indicating obvious whispering-gallery mode (WGM) behavior. The spectrum of the microcavity in air reveals two peaks, which are identified as the TM and TE modes [249], respectively. When the optical microcavity is immersed in liquids with different refractive indices, however, light loss is observed for both the TM and TE modes. Moreover, the loss for the TE mode is more prominent than that of TM, making the TE mode disappear in the liquids. In addition, the mode positions in different liquids exhibit remarkable shifts, which make them especially suitable as a reflectometer.

The chemical sensing capability of rolled-up tubes is also evidenced by their mechanical response to the surrounding conditions. Particularly interesting efforts were pursued via a rolled-up tube that was partially open [132]. Elastic deformation can be observed from these 3D rolled-up tubes under even a small load, due to their ultra-elastic mechanical properties. Fig. 20(b) shows a time-lapse sequence of a partly closed Si/SiGe tube opening and closing, where a changing surface-tension load on the tube was provided by acetone evaporation. It is obvious that acetone underneath the tube has a slower evaporation rate than when it is inside the tube. As the acetone inside the tube evaporates (wetting length  $L$  decreases), the tube opens more and more until the gap is adequately open. After a threshold is reached, the tube begins to close, finally returning to its original shape. Such partially open tubes can be implanted for applications in remote chemical sensing through absorbing and desorbing molecules, where the selectivity can be achieved by chemical reactions with specific chemicals.

The three-dimensional geometries, coupled with the superior mechanical flexibility of 3D Si-based mesostructures made by the popped-up method, offer promising opportunities in complex microelectromechanical systems (MEMS), like multiscale vibration transducers able to operate in 3D space. Recently, a SiNM-based 3D vibrational microplatform that was tunable, multiscale, and multistable was demonstrated [216]. As shown in the left panel of Fig. 20(c), cage-like mesostructures with different material compositions (pure SU-8 photoresist, a SU-8/Si composite, and pure Si, from left to right) were generated by the popped-up technique [216]. Two representative vibrational modes of the cage structures, i.e., left-right and up-down, were obtained by FEA. The structures were excited by a 3D-printing testing stage with integrated piezoelectric actuators. A laser measurement system that captured the time dependence of light scattering was utilized to monitor the dynamic behavior of the 3D structures. The middle

and right panels of Fig. 20(c) presents the obtained amplitude-frequency responses of several cage structures (distinguished by the thickness ratios of the SU-8 and Si bilayers) under the two vibrational modes. Because Si has a much higher modulus (130 GPa) than SU-8 (4.02 GPa), the 3D cage structure composed of a bilayer of SU-8 (8.5  $\mu\text{m}$ ) and Si (1.5  $\mu\text{m}$ ) has a much higher resonant frequency than the pure SU-8 (10  $\mu\text{m}$ ) one. This modulus dependence of the resonant frequency becomes more pronounced for the cage structure made of a single layer of Si, which exhibits the largest resonant frequency of a pure SiNM-based 3D cage structure. From the experimental results displayed in Fig. 20(c), it is concluded that the detection limits for mass sensing by the proposed multiscale vibration transducers can be improved by tuning the lateral dimension and ribbon stiffness. 3D popped-up mesostructures provide a new concept in 3D MEMS with capabilities that could be exploited for applications in mechanical sensing, bio/chem-sensing, and other fields.

### 6.2.2. Micro/nanorobotics

One of the most promising applications for 3D thin films especially with tubular structures is micro/nanorobotics. This field of research provides enormous opportunities for environmental science, biomedicine, and biosensors [250–254]. Rolled-up nanotechnology, as discussed in Section 5.1, has the advantage of being able to tune the size and component shape of the tubular structures, thus offering the most convenient strategies to fabricate micro/nanorobots. For example, B. J. Nelson et al., inspired by the monotrichous bacteria flagella, demonstrated helical artificial bacterial flagella (ABF) by rolled-up nanotechnology, where the swimming behaviors in solutions can be precisely controlled [255,256]. Typically, an ABF consists of two parts: a helical tail and a soft-magnetic metal head, which is driven and controlled by electromagnetic fields. Facilitated by the unique rolled-up helical structures, an ABF can convert rotary motion to linear motion, and forward or backward motion can be simply realized by reversing the rotation direction, i.e., rotating the magnetic field clockwise [255].

On the other hand, rolled-up micro/nanorobots can be activated in a self-driven manner via a catalytic reaction of a fuel solution (e.g.,  $\text{H}_2\text{O}_2$ ). By incorporating catalytic materials (such as Ag or Pt that can decompose  $\text{H}_2\text{O}_2$  into  $\text{O}_2$  and  $\text{H}_2\text{O}$ ) on the inner wall of a microtube,  $\text{O}_2$  will be produced inside the cavity of the microtube when it is put into the  $\text{H}_2\text{O}_2$  fuel. Then, the accumulated  $\text{O}_2$  will form into bubbles and eject from a much larger end of a tube, causing the propulsion of the tube in the opposite direction. Based on the above self-driving principles, micro/nanorobots composed of various materials and their combinations, including metals [253], oxides [257], semiconductors [258] and organics [259,260] have been realized. To achieve a Si based catalytic microjet, Harazim et al. demonstrated SiO/SiO<sub>2</sub> microtubes coated with a thin Au layer via rolled-up nanotechnology. These tubes acquired a speed of about 150  $\mu\text{m}/\text{s}$  when immersed in 2%  $\text{H}_2\text{O}_2$  and 0.05% sodium dodecyl sulfate (SDS) [261].

Using Si/Ge based materials in micro/nanorobotics may provide several advantages, which are summarized in the three following aspects, i) compatibility: Si/GeNMs are completely compatible with current Si-based fabrication and can thus be conveniently processed into the as-designed geometries and components for micro/nanorobots; also, the superior bio-compatibilities of Si/Ge would offer great potentials in various bio-applications. ii) Ease of surface bio-functionalization: Si/Ge or their oxide materials can be modified with various functionalities [262,263], providing a strong capability of cargo loading or physical adsorption which is suitable for fundamental studies or biosensing applications [261,264]. iii) Biodegradability: Si/Ge or their alloy materials are demonstrated as biodegradable materials that provide a transient feature

[265,266], which can disappear when no longer needed. Considering all the above positive attributes, greater efforts are needed to create and fabricate Si/GeNM based micro/nanorobotics either for fundamental studies or for bioapplications.

### 6.2.3. Bio-Platforms

The 3D Si/Ge-based micro/nano-architectures, which are naturally closed, as well as well-positioned arrays, for example, rolled-up tubes or compressive buckles, provide ideal bio-platforms for the three-dimensional confinement of controlled cell cultures [267], neurite outgrowths [268,269], and drug delivery by tubular micro/nano-engines [270]. For instance, a rolled-up SiO/SiO<sub>2</sub> microtube with optical transparency has been investigated as a two-dimensional confined culture scaffold for yeast cells [267], as shown in Fig. 21(a). If the mother cell occupies a spacious rolled-up microtube with a diameter larger than itself, the grown offspring yeast cells will reach a zigzag arrangement in the tube, due to the confinement of the tubular channel. When the tube diameter is similar to or smaller than the mother cell size, however, the mother and/or daughter cells are more restricted in movement and align parallel to the tube axis. Such rolled-up microtubes can also be exploited as ideal culturing capsules for larger-size cells like neuron cells. As schematically described in Fig. 21(b), three-dimensional confinement for controlled neurite outgrowth, resulting in single-axon outgrowth through rolled-up Si/SiGe microtubes, is realized by selectively seeding individual neurons [268]. Because of the good compatibility with Si-based CMOS fabrication technology, well-designed arrays of microtubes can easily be made to guide neurites, thus forming predefined neuronal networks. Similar bio-platforms involving strong guidance for neurite outgrowth have also been demonstrated in a SiNM-based compression-buckled structure [269], where the microchannel is formed by buckled SiNMs and the PDMS substrate, as shown in Fig. 21(c).

Compared with conventional cell-culturing techniques, which largely take place *in vitro* on 2D tissue-culture plates, Petri dishes, or slides [271], these 3D bio-platforms based on strain-engineered 3D Si/Ge micro/nano-architectures offer several exciting

advantages, including: 1) small enough to confine a single cell for picking up isolated signals [268]; 2) able to supply controllable and orderable cell growth behaviors by state-of-the-art CMOS fabrication technology [267]; 3) able to provide a physiological microenvironment that mimics the natural extracellular matrix *in vivo* [272]; 4) able to add electrical or optical functionalities to the Si/Ge-based bio-platforms for stimulation or physiological measurement [269]; 5) convenient for modifying the surfaces of the bio-platforms, to tune the surface resistance or capacitance for optimized neuronal signaling [268]. With these unique features, 3D Si/GeNM-based micro/nano-architectures show themselves to be emerging bio-platforms for controllable cell culturing, hybrid neural-electronic systems, and bio-analysis.

### 6.2.4. Optoelectronic devices

Owing to their superior electronic and optical properties, Si and GeNMs have attracted considerable attention for applications in optoelectronic devices, for example photodetectors [273–275], solar cells [276], lasers [277], and light emitting diodes [278]. However, such benefits are compromised by lower efficiencies due to limited light-absorption thickness [273]. Among the various strategies for achieving efficient optical absorption, 3D architectures may provide a practical and convenient design. Fig. 22 illustrates an example of a 3D Si-based solar cell [220] whose fabrication begins with the formation of a flower-shaped planar PN-junction device. After releasing the flower-shaped planar device layer by selective etching of the buried oxide layer, a spherical Si shell can be formed by a capillary-driven, self-assembly method [220]. Then, a direct-writing-assisted metallization process utilized to make silver electrodes finishes the 3D spherical Si-based solar-cell fabrication, as displayed in Fig. 22(b) and (c). Current density-voltage characteristics recorded from a typical spherical solar cell are exhibited in Fig. 22(d). One can conclude that by adding a thin metal layer (aluminum) as a diffuse white reflector, the performances of the short-current density, open-circuit voltage, fill factor, as well as the conversion efficiency for spherical devices, are significantly improved.

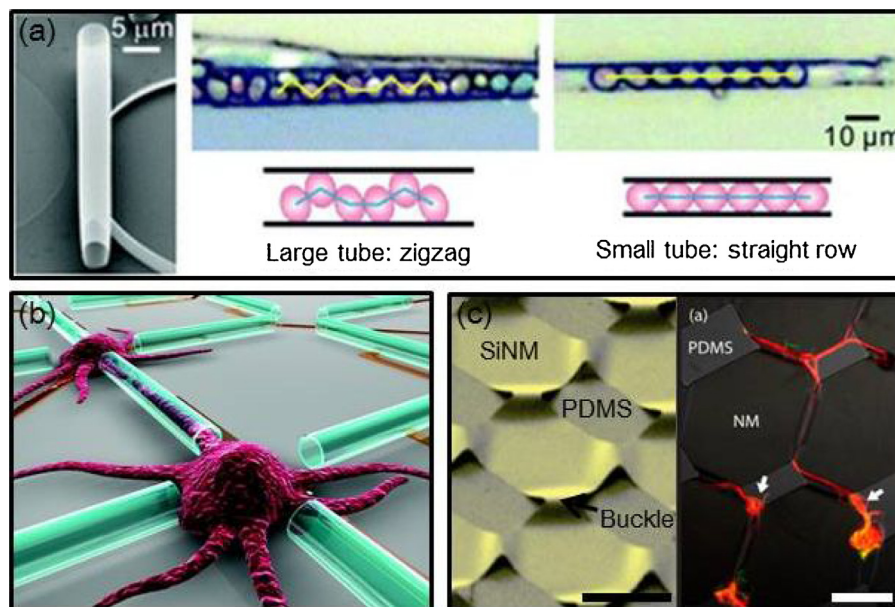


**Fig. 21.** (a) Left: SEM image of a typical rolled-up microtube. Right: optical images and schematic diagrams explaining different yeast-cell arrangements in a large microtube and a small microtube. Reprinted from Ref. [267]. (b) Schematic diagram of cortical neurons cultured in rolled-up Si/SiGe tubes [268]. (c) Left: optical image of microchannel array formed by the closed space between buckled SiNMs and a PDMS substrate. Right: confocal-fluorescent-microscopy image of strongly guided neuronal outgrowths within buckle delaminated microchannel array. All scale bars are 50  $\mu\text{m}$ . Reprinted from Ref. [269].

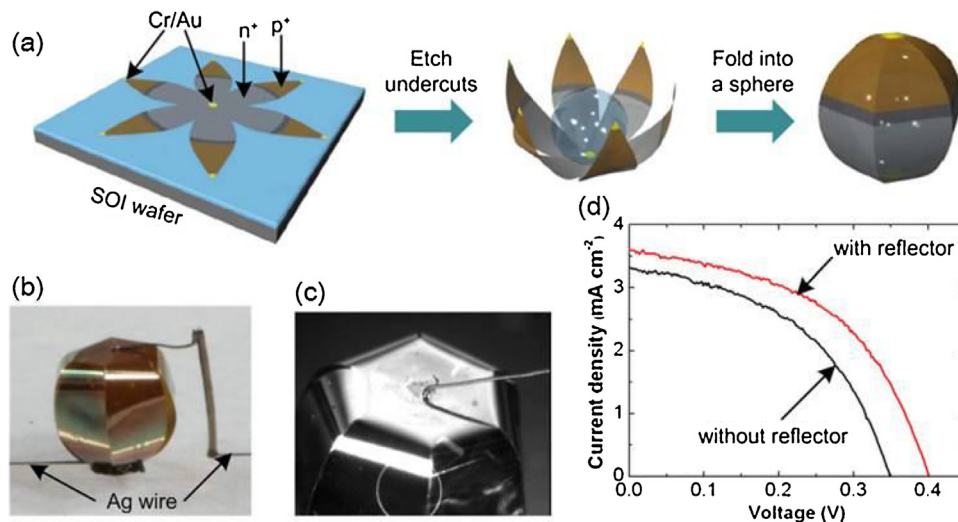


**Fig. 22.** (a) Schematic diagrams of the steps for fabricating a 3D Si membrane-based spherical solar cell. (b–c) Optical images of a complete 3D solar cell consisting of spherical Si, printed silver electrode, and an inner glass bead (not shown). (d) Current density–voltage characteristics of a 3D solar cell with (red curve) and without (black curve) a white diffuse reflector. Reprinted from Ref. [220]. (For interpretation of the references to colour in this figure legend, the reader is referred to the web version of this article.)

The spherical structures for optoelectronic devices (here, a solar cell) are extremely attractive, because of their intrinsic light-trapping enhancement [279]. Light-trapping behavior, which facilitates the performance of 3D optoelectronic devices, has also been demonstrated in 3D wrinkles [128,205,243], and tubular and cylindrical structures [220,280,281]. In addition, these 3D optical structures enable efficient light absorption when irradiated from a wide range of incident directions. With these superior advantages, extensions can be made to other exemplary forms of 3D

optoelectronics, electronic and photonic devices including photo-detectors [128,280], lasers [282,283], transistors [284], inductors [285,286], resonators [233,287], and optical couplers [288], which are not limited to Si/GeNMs.

#### 6.2.5. Energy harvesting

It is well known that Si and Ge are promising anode materials for the next-generation lithium-ion batteries (LIBs), holding high energy and power densities (about 4200 mAh/g for Si, and 1600

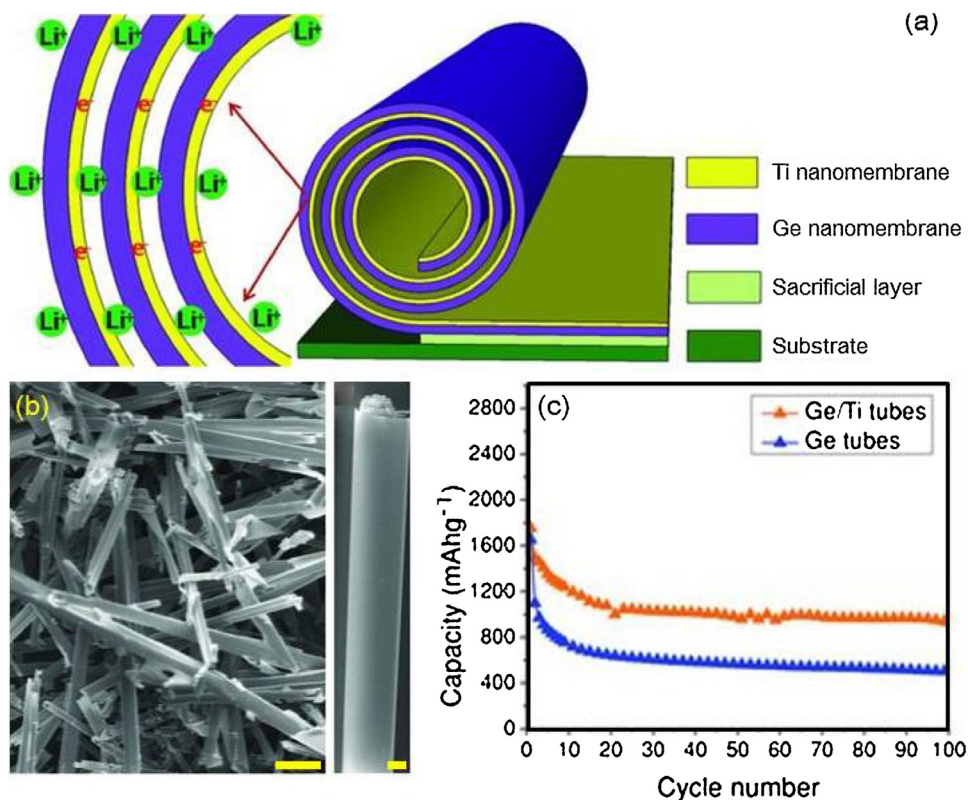


**Fig. 23.** (a) Schematic illustration of the rolled-up bilayer Ge/Ti tubular lithium-ion storage device, where the middle Ti layer is utilized for charge storage and delivery due to its high electrical conductivity. (b) SEM images of the hybrid bilayer Ge/Ti microtubes (left panel) and a magnified single Ge/Ti microtube with a cylindrical hollow structure composed of multilayer stacks (right). Scale bars: 10  $\mu\text{m}$  (left); 2  $\mu\text{m}$  (right). (c) Cycling performance of the discharge capacity for the hybrid Ge/Ti and Ge tubular lithium-ion batteries. Reprinted from Ref. [146].

mAh/g for Ge) [289,290]. However, these high-capacity electrode materials experience drastic volume changes ( $\sim 280\%$  for  $\text{Li}_{15}\text{Si}_4$ , and  $250\%$  for  $\text{Li}_{15}\text{Ge}_4$  [291]) during the lithiation/de-lithiation processes, leading to enormous mechanical stress, rapid cracking, electrode pulverization, and damage in the solid-electrolyte interphase [292–296]. Therefore, Si/Ge anodes degrade during the performance cycle. As researchers have addressed these critical issues, various Si/Ge nanostructures, such as nanoparticles, nanowires, nanotubes, and nanosheets, have shown greatly improved performance, which can be attributed to facile strain accommodation and accelerated electron and Li-ion diffusion kinetics [289,290].

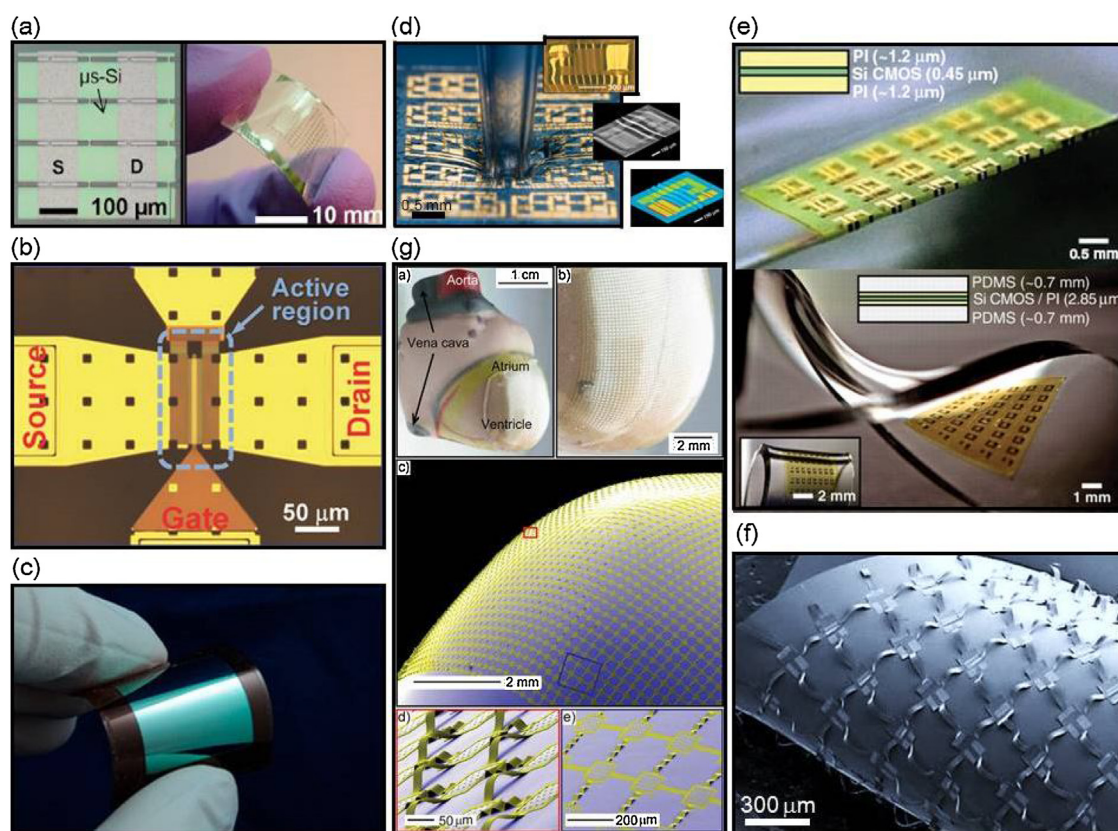
An alternative strategy for LIBs that utilizes 3D tubular Si/GeNMs made by the rolled-up technique and full relaxation of strain energy offers promise for accommodating the stresses induced by Li-ion insertion/extraction [146,297,298] and for preventing pulverization of the electrodes. In addition, projected areas of tubular LIBs can reach almost two orders smaller than their planar counterparts, thus leading to a highly integrated energy-storage system [7,299]. Yan et al. [146] utilized strain-released, hybrid bilayer Ge/Ti NMs to fabricate a 3D tubular Ge-based LIB by the rolled-up technique, as schematically illustrated in Fig. 23(a). Because Ti has outstanding electrical conductivity [300], it can act as electron “superhighways” for charge storage and delivery. It should be noted that gaps between adjacent bilayers (sketched in Fig. 23(a)), which are induced by the natural roughness of the deposited films as well as the imperfect roll-up process, have several advantages: (1) providing hollow channels for electrochemical reactions; (2) facilitating fast diffusion rates for Li ions; and (3) possessing good tolerance for volume variations.

Fig. 23(b) shows SEM images of the rolled-up microtubes, featuring two open ends, a smooth surface, and a cylindrical hollow structure composed of multilayer stacks.

The discharging and charging capacities of the hybrid Ge/Ti tubular LIBs have been evaluated to be 1753 mAh/g and 1490 mAh/g (Fig. 23(c)), respectively, for the first-cycle at a rate of C/16. Compared with other Ge nanostructure-based anodes, the rolled-up tubular Ge/Ti NMs reveal outstanding coulombic efficiencies (85%), much higher than those for Ge-based nanowire arrays (33%) [301], nanotubes (76%) [302], or composites with graphene (52%) [303]. In addition, the hybrid Ge/Ti microtube electrode shows a straightforwardly higher capacity than a pure Ge microtube does for all investigated current densities, which can be attributed to enhanced surface electrochemical reactivity attained by adding Ti layers. Of course, the concept of fabricating energy-storage devices by utilizing 3D strain-released NMs is not limited to Ge. Si and its composites, such as a C/Si/C trilayer [297], Si/reduced-graphene-oxide bilayer [298],  $\text{SiO}_x/\text{SiO}_y$  bilayer [304], and graphene/ $\text{GeO}_2$  multilayer [305], are being investigated for tubular LIBs, demonstrating a promising future for next-generation energy storage devices.

#### 6.2.6. Flexible electronics: from bendable to stretchable, twistable, and foldable

The compatibility with state-of-the-art CMOS fabrication techniques, as well as the superior and stable physical properties, especially in unique flexible configurations, provided by Si/GeNMs offers significant opportunities in advanced electronics. The most remarkable demonstration is in the high-performance flexible/stretchable electronics domain that cannot be addressed by their



**Fig. 24.** Mechanical principles and fundamentals of flexible electronics. Examples of the first generation of flexible electronics: (a) flexible transistors [306]; (b) flexible photodetector in a transistor structure [273]; (c) flexible photonic microcavity [313]; (d) stretchable SiNM-based circuit with a wavy design, its center being compressed by a glass capillary tube. The insets show typical optical, SEM, and simulation results for a wavy logic gate. Reprinted from Ref. [325]. (e) Images of foldable and twistable wavy Si-based CMOS circuits that use a neutral-mechanical-plane concept [325]. (f) SEM image of a deformed CMOS inverter array with a non-coplanar mesh design [326]. (g) Optical and magnified SEM images of a Si-based CMOS array with a mesh design on the surface of a plastic model of the human heart [327].

bulk counterparts. By utilizing the well-developed assembly techniques discussed above, flexible Si/GeNMs can be released from bulk materials, then integrated with flexible substrates, which can be further explored for the new generation of flexible electrical and optical devices, including transistors (Fig. 24(a) [306], [307,308]), photodetectors (Fig. 24(b) [273], or others that can be found in refs. [309–312]), photonic microcavities (Fig. 24(c)) [313], optical waveguide/photonic circuits [314–319], photodiodes [320–322], and radio-frequency switches [323,324]. Although such flexible electronics exhibit a certain degree of mechanical pliability, they are limited by the critical fracture point of the Si/GeNMs (or devices). Hence, the requirement for super-flexibility for functional devices that involve stretching, twisting, and even folding cannot be realized, and super-flexibility needs to be developed in a smart way.

More and more effort has recently been invested in moving on from the first generation of Si/GeNM-based flexible electronics to the second generation of stretchable electronics, which have distinct mechanical requirements, including stretchability, compressibility, twistability, and foldability. Si/Ge wrinkles and wavy structures formed by compressive buckling have been demonstrated to be able to tolerate stretching/compressive stress in a manner similar to an accordion [6]. As discussed above, devices/circuits constructed on these 3D structures become one of the most feasible schemes for accomplishing the technological goal. Fig. 24(d) shows a Si-based circuit on an elastic substrate in a 3D wavy structure [325]. Optical, SEM, and FEA-simulation results of a typical wavy inverter with two transistors are shown in the insets. Guided by elaborate mechanical principles, the ultra-thin device/support system with unique wavy designs can be optimized to provide impressive mechanical properties, with a stretchability of about 10% and a bendability of about 0.05 mm [325]. However, further stretching or bending will induce fractures and/or delamination of the device layers, resulting in device/circuit failure as well.

A simple design that involves placing the device layer at the neutral mechanical plane can address these failures [235,328]. As illustrated at the top of Fig. 24(e), the ultra-thin Si CMOS layer is sandwiched within two PI films ( $\sim 1.2 \mu\text{m}$ ) to form a PI/Si-CMOS/PI system, which is so foldable that it tightly wraps around a microscope cover slip [325]. The PI encapsulation layer could firstly ensure good adhesion strength with the sandwiched underlying device layer, thus preventing delamination to a large degree. Moreover, this unique sandwich design will place the device layer within the neutral mechanical plane where strain induced by bending could reach zero under ideal conditions. Incorporating such foldable designs with wavy configurations could achieve stretchable Si-CMOS circuits with twistability. As illustrated in the bottom panel of Fig. 24(e), dual neutral mechanical plane design, i.e., PDMS/PI/Si-CMOS/PI/PDMS, enables twisting and bending [325].

More complex stretchable circuits, involving very large-scale integration of individual electrical components, can be realized with non-coplanar mesh designs using buckled electrical/mechanical interconnections [326]. The overall process begins with fabricating a CMOS circuit on an ultra-thin plastic substrate, e.g., PI ( $1.2 \mu\text{m}$ )/poly(methylmethacrylate) (PMMA, 100 nm)/Si. After that, a thin top layer of PI ( $1.2 \mu\text{m}$ ) is introduced to protect the circuit and place it near the neutral mechanical plane. Then, the circuit is patterned into a segmented mesh by removing certain regions of the PI/PMMA between the electronic components of the system, leaving the active devices connected electrically and/or mechanically. Immersion in acetone will release the system. Finally, the non-coplanar CMOS mesh is achieved by transferring it to a stretched PDMS, followed by the release of the PDMS pre-strain [326], as shown in Fig. 24(f). With an optimized mechanical

design, the stretchable CMOS circuit with a non-coplanar mesh structure as described can offer extremely high stretchability (e.g., up to 140%) and the capability of complex twisting, shearing, and other classes of deformation. Such increased stretchability enables more application possibilities, especially in intimately integrated electronics on substrates with complex, non-planar/curvilinear surfaces [326]. Fig. 24(g) demonstrates an example of the intimate integration of a stretchable Si-CMOS circuit with a mesh design on a scale model of the heart, which contains a complex, irregular surface [327]. Here, the initially buckled interconnects adopt various spatially distributed configurations to accommodate the strains produced by the irregular surfaces, as illustrated in the two bottom SEM images in Fig. 24(g). It is predictable that with the rapid development of NM science and technology, high-performance Si/Ge-based stretchable electronics, integratable with the soft, curvilinear surfaces of living organisms, will be highly demanded for purposes of human health monitoring and therapeutics, including bio-inspired electronic eyes [329], cardiac/cerebral monitors [330–332], epidermal electrical sensors [333,334], and implantable long-term/transient electronics [60,335,336].

## 7. Summary and outlook

In this review, we have summarized the recent progress in the strain engineering and mechanical assembly of Si/GeNMs, with a special emphasis on their modified physical properties and potential applications. Typically, the strain engineering of Si/GeNMs is implemented in a plane, leading to the altering of lattice parameters. Therefore, the corresponding physical properties can be well regulated, which implies tremendous potential in electronics, photonics, and optoelectronics, for example, in high-performance flexible transistors, CMOS circuits, sensors, photodetectors, and on-chip light emitters. Additionally, the strain engineering of Si/GeNMs can also be carried out macroscopically with large-scale out-of-plane deformations, owing to their superior mechanical flexibility. Accordingly, 2D planar Si/GeNMs transform into 3D architectures of various shapes (e.g., tubes, rings, helices, wrinkles, buckles, and origami/kirigami-based mesostructures) through appropriate approaches and mechanical principles. The advanced assembly concepts for unique Si/GeNM-based 3D architectures provide new possibilities in both fundamental investigations and application-level devices/systems. Functional devices/systems based on a variety of 3D Si/Ge structures can be achieved for applications such as highly stretchable devices/circuits, highly integrated energy harvesters, novel sensing/detecting devices, and bio-medical diagnosis and/or therapy setups.

For strain-engineered Si/GeNMs, although it is quite difficult to find a universal strategy that is capable of fabricating strained Si/GeNMs for arbitrary strain value or form of integration (e.g., on rigid or flexible substrates), one can anticipate solutions coming from the available methods outlined in this review. Although external mechanical stress induced strain in Si/GeNMs may be a powerful method for fundamental studies, strained Si/GeNMs achieved via epitaxy are more compatible with current Si-based micro/nanofabrication technology; therefore high-performance strained Si/GeNM-based devices can be conveniently realized. However, the small achievable strain values and reduced materials quality will significantly affect its further development. Strain obtained by mechanically applied external stress may bypass these limitations, although compatibility with device fabrication is currently challenging. The combination of epitaxy and external stress application may provide opportunities to solve the above issues. Future research efforts in this field will likely focus on further exploiting convenient strategies for enhancing strain

values and modulating the band structures of Si/GeNMs in a controllable manner; heterogeneously integrating these highly strained NMs on rigid/flexible substrates with high-quality interfaces; fabricating high-performance, strained SiNM-based flexible electronics (high-speed, low power consumption); and fabricating tensilely strained GeNM-based, on-chip light sources. Other efforts will concentrate on fundamental studies of the physical properties of “modified” Si/GeNMs via surface modification and thinning (even silicene [337] and germanene [338]), and on the heterogeneous integration of Si/GeNMs with other thin-film materials, such as organic/inorganic NMs [339], and newly emerging layered materials (graphene, MoS<sub>2</sub>, MoSe<sub>2</sub>, WS<sub>2</sub>, etc.) [340–347].

For strain-engineered Si/Ge micro/nano-architectures, the future lies in many aspects of science, engineering, and practical applications, including the following: (i) the mechanical assembly of Si/GeNMs into 3D architectures always involves large structure-shaping deformations and atom-scale lattice deformations. This indeed opens possibilities for macroscopic property modification induced by the 3D geometry (e.g., light absorption, mechanical properties, etc.), and microscopic-property modification induced by the lattice deformations (e.g., carrier mobility, band-structure modulation, light emission, etc.). Additional fundamental studies are needed to reveal more basic properties governed by 3D-geometry transformations. (ii) From an engineering viewpoint, more complex Si/GeNM-based 3D configurations should be fabricated by optimizing the assembly approaches (e.g., the origami and kirigami concepts) and designing the appropriate 2D precursors. Also, the capability to design bi-stable or multi-stable 3D configurations, which could simply achieve geometry transformations in controllable manners, may create great opportunities for microelectronic and biomedical applications. (iii) From a practical point of view, the most compelling possibility for 3D Si/Ge configurations is bio-integratable and implantable electronics for health monitoring, diagnosis, and curing, which demand highly stretchable devices to conform to the complex surfaces of organ tissues. The fascinating physical properties of strain-engineered 2D and 3D Si/GeNMs, well-developed strategies for their synthesis, assembly, and strain engineering, and broad prospects for applications in electronics, photonics, mechanics, robotics, and biomedicine, promise a bright future for strain engineering and self-assembly of Si/GeNMs.

## Acknowledgements

This work is supported by the National Natural Science Foundation of China (51711540298, 61628401, U1632115, 51602056), the Program of National Science and Technology Major Project (2016ZX02301003), Shanghai Academic/Technology Research Leader (16XD1404200), Key Research Project of Frontier Science, Chinese Academy of Sciences (QYZDB-SSW-JSC021), Science and Technology Commission of Shanghai Municipality (17JC1401700), the National Key Technologies R&D Program of China (2015ZX02102-003) and the Changjiang Young Scholars Program of China. MGL's effort in the preparation of this review was supported by the US Department of Energy, Office of Science, Basic Energy Sciences, Award #DEFG02-03ER46028. Q. L. Guo acknowledges China Postdoctoral Science Foundation No. 2015M581523 and the International Postdoctoral Exchange Fellowship Program supported by the Office of China Postdoctoral Council.

## References

- [1] G.E. Moore, *Electronics* 38 (1965) 114–117.
- [2] R. Pillarisetty, *Nature* 479 (2011) 324–328.
- [3] J.A. Rogers, M.G. Lagally, R.G. Nuzzo, *Nature* 477 (2011) 45–53.
- [4] M.G. Lagally, *MRS Bull.* 32 (2007) 57–63.
- [5] S.A. Scott, M.G. Lagally, *J. Phys. D: Appl. Phys.* 40 (2007) R75–R92.
- [6] J.A. Rogers, T. Someya, Y. Huang, *Science* 327 (2010) 1603–1607.
- [7] G. Huang, Y. Mei, *Adv. Mater.* 24 (2012) 2517–2546.
- [8] F. Cavallo, M.G. Lagally, *Soft Matter* 6 (2010) 439–455.
- [9] F. Cavallo, M.G. Lagally, *Nanoscale Res. Lett.* 7 (2012) 628.
- [10] A.J. Baca, M.A. Meitl, H.C. Ko, S. Mack, H.S. Kim, J. Dong, P.M. Ferreira, J.A. Rogers, *Adv. Funct. Mater.* 17 (2007) 3051–3062.
- [11] A.J. Baca, J.-H. Ahn, Y. Sun, M.A. Meitl, E. Menard, H.-S. Kim, W.M. Choi, D.-H. Kim, Y. Huang, J.A. Rogers, *Angew. Chem. Int. Ed.* 47 (2008) 5524–5542.
- [12] M.M. Roberts, L.J. Klein, D.E. Savage, K.A. Slinker, M. Friesen, G. Celler, M.A. Eriksson, M.G. Lagally, *Nat. Mater.* 5 (2006) 388–393.
- [13] Y. Mei, G. Huang, A.A. Solovev, E.B. Ureña, I. Mönch, F. Ding, T. Reindl, R.K.Y. Fu, P.K. Chu, O.G. Schmidt, *Adv. Mater.* 20 (2008) 4085–4090.
- [14] S. Xu, Z. Yan, K.-I. Jang, W. Huang, H. Fu, J. Kim, Z. Wei, M. Flavin, J. McCracken, R. Wang, A. Badae, Y. Liu, D. Xiao, G. Zhou, J. Lee, H.U. Chung, H. Cheng, W. Ren, A. Banks, X. Li, U. Paik, R.G. Nuzzo, Y. Huang, Y. Zhang, J.A. Rogers, *Science* 347 (2015) 154–159.
- [15] D.-Y. Khang, H. Jiang, Y. Huang, J.A. Rogers, *Science* 311 (2006) 208–212.
- [16] Y. Sun, W.M. Choi, H. Jiang, Y.Y. Huang, J.A. Rogers, *Nat. Nanotechnol.* 1 (2006) 201–207.
- [17] Y. Sun, V. Kumar, I. Adesida, J.A. Rogers, *Adv. Mater.* 18 (2006) 2857–2862.
- [18] M.A. Meitl, Z.-T. Zhu, V. Kumar, K.J. Lee, X. Feng, Y.Y. Huang, I. Adesida, R.G. Nuzzo, J.A. Rogers, *Nat. Mater.* 5 (2006) 33–38.
- [19] R.A. Minamisawa, M.J. Süess, R. Spolenak, J. Faist, C. David, J. Gobrecht, K.K. Bourdelle, H. Sigg, *Nat. Commun.* 3 (2012) 1096.
- [20] J.R. Sánchez-Pérez, C. Boztug, F. Chen, F.F. Sudradjat, D.M. Paskiewicz, R.B. Jacobson, M.G. Lagally, R. Paiella, *Proc. Natl. Acad. Sci. U. S. A.* 108 (2011) 18893–18898.
- [21] J.R. Jain, A. Hryciw, T.M. Baer, A.B. MillerDavid, M.L. Brongersma, R.T. Howe, *Nat. Photonics* 6 (2012) 398–405.
- [22] H.-C. Yuan, Z. Ma, M.M. Roberts, D.E. Savage, M.G. Lagally, *J. Appl. Phys.* 100 (2006)013708.
- [23] H. Zhou, J.-H. Seo, D.M. Paskiewicz, Y. Zhu, G.K. Celler, P.M. Voyles, W. Zhou, M.G. Lagally, Z. Ma, *Sci. Rep.* 3 (2013) 1291.
- [24] J.-H. Ahn, H.-S. Kim, K.J. Lee, S. Jeon, S.J. Kang, Y. Sun, R.G. Nuzzo, J.A. Rogers, *Science* 314 (2006) 1754–1757.
- [25] K. Koyama, R. Petre, E.V. Gotthelf, U. Hwang, M. Matsuura, M. Ozaki, S.S. Holt, *Nature* 378 (1995) 255–258.
- [26] W. Liu, M. Asheghi, *Appl. Phys. Lett.* 84 (2004) 3819–3821.
- [27] P. Zhang, E. Tevaarwerk, B.-N. Park, D.E. Savage, G.K. Celler, I. Knezevic, P.G. Evans, M.A. Eriksson, M.G. Lagally, *Nature* 439 (2006) 703–706.
- [28] S.A. Scott, W. Peng, A.M. Kiefer, H. Jiang, I. Knezevic, D.E. Savage, M.A. Eriksson, M.G. Lagally, *ACS Nano* 3 (2009) 1683–1692.
- [29] P. Zhang, E.P. Nordberg, B.N. Park, G.K. Celler, I. Knezevic, P.G. Evans, M.A. Eriksson, M.G. Lagally, *New J. Phys.* 8 (2006) 200.
- [30] C. Boztug, J.R. Sánchez-Pérez, F. Cavallo, M.G. Lagally, R. Paiella, *ACS Nano* 8 (2014) 3136–3151.
- [31] E.S.M. Goh, T.P. Chen, C.Q. Sun, Y.C. Liu, *J. Appl. Phys.* 107 (2010)024305.
- [32] W. Peng, Z. Aksamija, S.A. Scott, J.J. Endres, D.E. Savage, I. Knezevic, M.A. Eriksson, M.G. Lagally, *Nat. Commun.* 4 (2013)1339.
- [33] F. Chen, E.B. Ramayya, C. Euaruksakul, F.J. Himpfel, G.K. Celler, B. Ding, I. Knezevic, M.G. Lagally, *ACS Nano* 4 (2010) 2466–2474.
- [34] J. Ristein, *Science* 313 (2006) 1057–1058.
- [35] P. Feng, G. Wu, O.G. Schmidt, Y. Mei, *Appl. Phys. Lett.* 105 (2014)121101.
- [36] P. Feng, I. Mönch, G. Huang, S. Harazim, E.J. Smith, Y. Mei, O.G. Schmidt, *Adv. Mater.* 22 (2010) 3667–3671.
- [37] E. Song, W. Si, R. Cao, P. Feng, I. Mönch, G. Huang, Z. Di, O.G. Schmidt, Y. Mei, *Nanotechnology* 25 (2014)485201.
- [38] P. Feng, I. Mönch, S. Harazim, G. Huang, Y. Mei, O.G. Schmidt, *Nano Lett.* 9 (2009) 3453–3459.
- [39] E. Chavez-Angel, J.S. Reparaz, J. Gomis-Bresco, M.R. Wagner, J. Cuffe, B. Graczykowski, A. Shchepetov, H. Jiang, M. Prunnila, J. Ahopelto, F. Alzina, C.M. S. Torres, *APL Mater.* 2 (2014)012113.
- [40] S. Chen, Q. Wu, C. Mishra, J. Kang, H. Zhang, K. Cho, W. Cai, A.A. Balandin, R.S. Ruoff, *Nat. Mater.* 11 (2012) 203–207.
- [41] J.-U. Lee, D. Yoon, H. Kim, S.W. Lee, H. Cheong, *Phys. Rev. B* 83 (2011)081419.
- [42] C.J. Glassbrenner, G.A. Slack, *Phys. Rev.* 134 (1964) A1058–A1069.
- [43] C. Mangold, S. Neogi, D. Donadio, *Appl. Phys. Lett.* 109 (2016)053902.
- [44] D.P. Schroeder, Z. Aksamija, A. Rath, P.M. Voyles, M.G. Lagally, M.A. Eriksson, *Phys. Rev. Lett.* 115 (2015)256101.
- [45] J.-K. Yu, S. Mitrovic, D. Tham, J. Varghese, J.R. Heath, *Nat. Nanotechnol.* 5 (2010) 718–721.
- [46] S. Neogi, J.S. Reparaz, L.F.C. Pereira, B. Graczykowski, M.R. Wagner, M. Sledzinska, A. Shchepetov, M. Prunnila, J. Ahopelto, C.M. Sotomayor-Torres, D. Donadio, *ACS Nano* 9 (2015) 3820–3828.
- [47] Z. Aksamija, I. Knezevic, *Phys. Rev. B* 82 (2010)045319.
- [48] G.J. Snyder, E.S. Toberer, *Nat. Mater.* 7 (2008) 105–114.
- [49] H.J. Ryu, Z. Aksamija, D.M. Paskiewicz, S.A. Scott, M.G. Lagally, I. Knezevic, M. A. Eriksson, *Phys. Rev. Lett.* 105 (2010)256601.
- [50] T. He, J. He, M. Lu, B. Chen, H. Pang, W.F. Reus, W.M. Nolte, D.P. Nackashi, P.D. Franzon, J.M. Tour, *J. Am. Chem. Soc.* 128 (2006) 14537–14541.
- [51] H. Jang, W. Lee, S.M. Won, S.Y. Ryu, D. Lee, J.B. Koo, S.-D. Ahn, C.-W. Yang, M.-H. Jo, J.H. Cho, J.A. Rogers, J.-H. Ahn, *Nano Lett.* 13 (2013) 5600–5607.
- [52] H. Zhang, J. Tersoff, S. Xu, H. Chen, Q. Zhang, K. Zhang, Y. Yang, C.-S. Lee, K.-N. Tu, J. Li, Y. Lu, *Sci. Adv.* 2 (2016).

- [53] M. Cho, J.-H. Seo, J. Lee, D. Zhao, H. Mi, X. Yin, M. Kim, X. Wang, W. Zhou, Z. Ma, *Appl. Phys. Lett.* 106 (2015) 181107.
- [54] D.-Y. Khang, J.A. Rogers, H.H. Lee, *Adv. Funct. Mater.* 19 (2009) 1526–1536.
- [55] G. Gopalakrishnan, D.A. Czaplewski, K.M. McElhinny, M.V. Holt, J.C. Silva-Martínez, P.G. Evans, *Appl. Phys. Lett.* 102 (2013) 033113.
- [56] A. Shchepetov, M. Prunnila, F. Alzina, L. Schneider, J. Cuffe, H. Jiang, E.I. Kauppinen, C.M.S. Torres, J. Ahopelto, *Appl. Phys. Lett.* 102 (2013) 192108.
- [57] S. Juodkazis, Y. Nishi, H. Misawa, V. Mizeikis, O. Schecker, R. Waitz, P. Leiderer, E. Scheer, *Opt. Express* 17 (2009) 15308–15317.
- [58] Z.Y. Dang, M. Motapothula, Y.S. Ow, T. Venkatesan, M.B.H. Breese, M.A. Rana, A. Osman, *Appl. Phys. Lett.* 99 (2011) 223105.
- [59] F. Delachat, C. ConstanCIAS, F. Fournel, C. Morales, B. Le Drogoff, M. Chaker, J. Margot, *ACS Nano* 9 (2015) 3654–3663.
- [60] H. Fang, K.J. Yu, C. Gloschat, Z. Yang, E. Song, C.-H. Chiang, J. Zhao, S.M. Won, S. Xu, M. Trumppis, Y. Zhong, S.W. Han, Y. Xue, D. Xu, S.W. Choi, G. Cauwenberghs, M. Kay, Y. Huang, J. Viventi, I.R. Efimov, J.A. Rogers, *Nat. Biomed. Eng.* 1 (2017) 0038.
- [61] H. Fang, J. Zhao, K.J. Yu, E. Song, A.B. Farimani, C.-H. Chiang, X. Jin, Y. Xue, D. Xu, W. Du, K.J. Seo, Y. Zhong, Z. Yang, S.M. Won, G. Fang, S.W. Choi, S. Chaudhuri, Y. Huang, M.A. Alam, J. Viventi, N.R. Aluru, J.A. Rogers, *Proc. Natl. Acad. Sci. U. S. A.* 113 (2016) 11682–11687.
- [62] H.C. Ko, A.J. Baca, J.A. Rogers, *Nano Lett.* 6 (2006) 2318–2324.
- [63] D. Shahjerdi, S.W. Bedell, *Nano Lett.* 13 (2013) 315–320.
- [64] W.S. Ho, Y.-H. Dai, Y. Deng, C.-H. Lin, Y.-Y. Chen, C.-H. Lee, C.W. Liu, *Appl. Phys. Lett.* 94 (2009) 261107.
- [65] D. Chen, N. Zhang, B. Wang, A. Xu, Y. Li, S. Yang, G. Wang, Q. Guo, *Appl. Phys. Lett.* 111 (2017) 062104.
- [66] D. Chen, D. Wang, Y. Chang, Y. Li, R. Ding, J. Li, X. Chen, G. Wang, Q. Guo, *Appl. Phys. Express* 11 (2018) 011301.
- [67] D. Chen, Q. Guo, N. Zhang, B. Wang, A. Xu, Y. Li, S. Yang, G. Wang, *J. Vac. Sci. Technol. B* 35 (2017) 041203.
- [68] D. Chen, Z. Xue, G. Wang, Q. Guo, L. Liu, M. Zhang, S. Liu, X. Wei, *Appl. Phys. Express* 7 (2014) 061302.
- [69] G.K. Celler, S. Cristoloveanu, *J. Appl. Phys.* 93 (2003) 4955–4978.
- [70] K. Munho, C. Sang June, D. Yash Jayeshbhai, M. Hongyi, M. Solomon, S. Jung-Hun, U.Y. Jung, M. Zhenqiang, *Semicond. Sci. Technol.* 33 (2018) 015017.
- [71] S. Wang, B.D. Weil, Y. Li, K.X. Wang, E. Garnett, S. Fan, Y. Cui, *Nano Lett.* 13 (2013) 4393–4398.
- [72] H.M. Fahad, H. Shiraki, M. Amani, C. Zhang, V.S. Hebbur, W. Gao, H. Ota, M. Hettick, D. Kiriya, Y.-Z. Chen, Y.-L. Chueh, A. Javey, *Sci. Adv.* 3 (2017).
- [73] M.J. Liu, G.S. Huang, P. Feng, Q.L. Guo, F. Shao, Z.A. Tian, G.J. Li, Q. Wan, Y.F. Mei, *Appl. Phys. Lett.* 108 (2016) 253503.
- [74] M. Liu, G. Huang, P. Feng, Q. Guo, F. Shao, Z. Tian, G. Li, Q. Wan, Y. Mei, *J. Semicond.* 38 (2017) 064006.
- [75] E. Song, H. Fang, X. Jin, J. Zhao, C. Jiang, K.J. Yu, Y. Zhong, D. Xu, J. Li, G. Fang, H. Du, J. Zhang, J.M. Park, Y. Huang, M.A. Alam, Y. Mei, J.A. Rogers, *Adv. Electron. Mater.* 3 (2017) 1700077.
- [76] E. Song, Y.K. Lee, R. Li, J. Li, X. Jin, K.J. Yu, Z. Xie, H. Fang, Y. Zhong, H. Du, J. Zhang, G. Fang, Y. Kim, Y. Yoon, M.A. Alam, Y. Mei, Y. Huang, J.A. Rogers, *Adv. Funct. Mater.* (2018), doi: <http://dx.doi.org/10.1002/adfm.201702284>.
- [77] X. Feng, M.A. Meitl, A.M. Bowen, Y. Huang, R.G. Nuzzo, J.A. Rogers, *Langmuir* 23 (2007) 12555–12560.
- [78] A. Carlson, A.M. Bowen, Y. Huang, R.G. Nuzzo, J.A. Rogers, *Adv. Mater.* 24 (2012) 5284–5318.
- [79] K.S. Kim, Y. Zhao, H. Jang, S.Y. Lee, J.M. Kim, K.S. Kim, J.-H. Ahn, P. Kim, J.-Y. Choi, B.H. Hong, *Nature* 457 (2009) 706–710.
- [80] M.-Y. Tsai, A. Tarasov, Z.R. Hesabi, H. Taghinejad, P.M. Campbell, C.A. Joiner, A. Adibi, E.M. Vogel, *ACS Appl. Mater. Inter.* 7 (2015) 12850–12855.
- [81] Q. Guo, M. Zhang, Z. Xue, L. Ye, G. Wang, G. Huang, Y. Mei, X. Wang, Z. Di, *Appl. Phys. Lett.* 103 (2013) 264102.
- [82] Y. Yang, Y. Hwang, H.A. Cho, J.-H. Song, S.-J. Park, J.A. Rogers, H.C. Ko, *Small* 7 (2011) 484–491.
- [83] Q. Guo, M. Zhang, Z. Xue, G. Wang, D. Chen, R. Cao, G. Huang, Y. Mei, Z. Di, X. Wang, *Small* 11 (2015) 4140–4148.
- [84] S. Kim, J. Wu, A. Carlson, S.H. Jin, A. Kovalsky, P. Glass, Z. Liu, N. Ahmed, S.L. Elgan, W. Chen, P.M. Ferreira, M. Sitti, Y. Huang, J.A. Rogers, *Proc. Natl. Acad. Sci. U. S. A.* 107 (2010) 17095–17100.
- [85] D.S. Grierson, F.S. Flack, M.G. Lagally, K.T. Turner, *J. Appl. Phys.* 120 (2016) 093103.
- [86] H. Lee, D.-S. Um, Y. Lee, S. Lim, H.-j. Kim, H. Ko, *Adv. Mater.* 28 (2016) 7457–7465.
- [87] J. Welsler, J.L. Hoyt, J.F. Gibbons, NMOS and PMOS transistors fabricated in strained silicon/relaxed silicon-germanium structures, *International Technical Digest on Electron Devices Meeting*, 1992 (1992) 1000–1002.
- [88] M. Chu, Y. Sun, U. Aghoram, S.E. Thompson, *Annu. Rev. Mater. Res.* 39 (2009) 203–229.
- [89] Y. Huo, H. Lin, R. Chen, M. Makarova, Y. Rong, M. Li, T.I. Kamins, J. Vuckovic, J.S. Harris, *Appl. Phys. Lett.* 98 (2011) 011111.
- [90] J. Liu, D.D. Cannon, K. Wada, Y. Ishikawa, D.T. Danielson, S. Jongthammanurak, J. Michel, L.C. Kimerling, *Phys. Rev. B* 70 (2004) 155309.
- [91] D.M. Paskiewicz, B. Tanto, D.E. Savage, M.G. Lagally, *ACS Nano* 5 (2011) 5814–5822.
- [92] M.J. Suess, R. Geiger, R.A. Minamisawa, G. Schiefler, J. Frigerio, D. Christina, G. Isella, R. Spolenak, J. Faist, H. Sigg, *Nat. Photonics* 7 (2013) 466–472.
- [93] J. Greil, A. Lugstein, C. Zeiner, G. Strasser, E. Bertagnolli, *Nano Lett.* 12 (2012) 6230–6234.
- [94] D.M. Paskiewicz, S.A. Scott, D.E. Savage, G.K. Celler, M.G. Lagally, *ACS Nano* 5 (2011) 5532–5542.
- [95] G. Sun, M. Zhang, Z. Xue, Q. Guo, D. Chen, Z. Mu, L. Dong, X. Wang, Z. Di, *Appl. Phys. Lett.* 105 (2014) 193505.
- [96] C. Feng, E. Chanan, L. Zheng, F.J. Himpel, L. Feng, G.L. Max, *J. Phys. D: Appl. Phys.* 44 (2011) 325107.
- [97] X.-W. Fu, Z.-M. Liao, J.-X. Zhou, Y.-B. Zhou, H.-C. Wu, R. Zhang, G. Jing, J. Xu, X. Wu, W. Guo, D. Yu, *Appl. Phys. Lett.* 99 (2011) 213107.
- [98] M.A. Bissett, M. Tsuji, H. Ago, *PCCP* 16 (2014) 11124–11138.
- [99] M.A. Bissett, W. Izumida, R. Saito, H. Ago, *ACS Nano* 6 (2012) 10229–10238.
- [100] H.J. Conley, B. Wang, J.I. Ziegler, R.F. Haglund, S.T. Pantelides, K.I. Bolotin, *Nano Lett.* 13 (2013) 3626–3630.
- [101] X.-W. Fu, Z.-M. Liao, R. Liu, J. Xu, D. Yu, *ACS Nano* 7 (2013) 8891–8898.
- [102] Y. Wang, Y. Chen, H. Li, X. Li, H. Chen, H. Su, Y. Lin, Y. Xu, G. Song, X. Feng, *ACS Nano* 10 (2016) 8199–8206.
- [103] T. Ghani, M. Armstrong, C. Auth, M. Bost, P. Charvat, G. Glass, T. Hoffmann, K. Johnson, C. Kenyon, J. Klaus, B. McIntyre, K. Mistry, A. Murthy, J. Sandford, M. Silberstein, S. Sivakumar, P. Smith, K. Zawadzki, S. Thompson, M. Bohr, A 90 nm high volume manufacturing logic technology featuring novel 45 nm gate length strained silicon CMOS transistors, *IEEE International Electron Devices Meeting 2003* (2003) pp. 11.16. 11–11.16.13.
- [104] G. Sun, Y. Sun, T. Nishida, S.E. Thompson, *J. Appl. Phys.* 102 (2007) 084501.
- [105] S. Suthram, J.C. Ziegler, T. Nishida, S.E. Thompson, *IEEE Electron Device Lett.* 28 (2007) 58–61.
- [106] M. Kim, H. Mi, M. Cho, J.-H. Seo, W. Zhou, S. Gong, Z. Ma, *Appl. Phys. Lett.* 106 (2015) 212107.
- [107] J. Liu, X. Sun, D. Pan, X. Wang, L.C. Kimerling, T.L. Koch, J. Michel, *Opt. Express* 15 (2007) 11272–11277.
- [108] J. Michel, J. Liu, L.C. Kimerling, *Nat. Photonics* 4 (2010) 527–534.
- [109] P.H. Lim, S. Park, Y. Ishikawa, K. Wada, *Opt. Express* 17 (2009) 16358–16365.
- [110] C. Boztug, J.R. Sánchez-Pérez, F.F. Sudrajat, R.B. Jacobson, D.M. Paskiewicz, M.G. Lagally, R. Paiella, *Small* 9 (2013) 622–630.
- [111] D. Nam, D. Sukhdeo, A. Roy, K. Balram, S.-L. Cheng, K.C.-Y. Huang, Z. Yuan, M. Brongersma, Y. Nishi, D. Miller, K. Saraswat, *Opt. Express* 19 (2011) 25866–25872.
- [112] M. Prost, M. El Kurdi, A. Ghrib, S. Sauvage, X. Checoury, N. Zerounian, F. Aniel, G. Beaudoin, I. Sagnes, F. Boeuf, P. Boucaud, *Opt. Express* 23 (2015) 6722–6730.
- [113] M. Prost, M.E. Kurdi, A. Ghrib, X. Checoury, N. Zerounian, F. Aniel, G. Beaudoin, I. Sagnes, C. Baudot, F. Boeuf, P. Boucaud, *Appl. Phys. Lett.* 104 (2014) 241104.
- [114] J. Petykiewicz, D. Nam, D.S. Sukhdeo, S. Gupta, S. Buckley, A.Y. Piggott, J. Vučković, K.C. Saraswat, *Nano Lett.* 16 (2016) 2168–2173.
- [115] X. Sun, J. Liu, L.C. Kimerling, J. Michel, *Opt. Lett.* 34 (2009) 1198–1200.
- [116] J. Liu, X. Sun, L.C. Kimerling, J. Michel, *Opt. Lett.* 34 (2009) 1738–1740.
- [117] J. Liu, X. Sun, R. Camacho-Aguilera, L.C. Kimerling, J. Michel, *Opt. Lett.* 35 (2010) 679–681.
- [118] D. Botez, L. Figueroa, S. Wang, *Appl. Phys. Lett.* 29 (1976) 502–504.
- [119] F.A. Blum, K.L. Lawley, W.C. Scott, W.C. Holton, *Appl. Phys. Lett.* 24 (1974) 430–432.
- [120] O.G. Schmidt, K. Eberl, *Nature* 410 (2001) 168.
- [121] V.Y. Prinz, V.A. Seleznev, A.K. Gutakovskiy, A.V. Chehovskiy, V.V. Preobrazhenskii, M.A. Putyato, T.A. Gavrilova, *Physica E* 6 (2000) 828–831.
- [122] X. Li, *J. Phys. D: Appl. Phys.* 41 (2008) 193001.
- [123] Y. Mei, D.J. Thurmer, F. Cavallo, S. Kiravittaya, O.G. Schmidt, *Adv. Mater.* 19 (2007) 2124–2128.
- [124] M. Huang, C. Boone, M. Roberts, D.E. Savage, M.G. Lagally, N. Shaji, H. Qin, R. Blick, J.A. Nairn, F. Liu, *Adv. Mater.* 17 (2005) 2860–2864.
- [125] I.S. Chun, A. Challa, B. Derickson, K.J. Hsia, X. Li, *Nano Lett.* 10 (2010) 3927–3932.
- [126] M. Huang, F. Cavallo, F. Liu, M.G. Lagally, *Nanoscale* 3 (2011) 96–120.
- [127] P. Cendula, S. Kiravittaya, Y.F. Mei, C. Deneke, O.G. Schmidt, *Phys. Rev. B* 79 (2009) 085429.
- [128] Q. Guo, Y. Fang, M. Zhang, G. Huang, P.K. Chu, Y. Mei, Z. Di, X. Wang, *IEEE Trans. Electron Dev.* 64 (2016) 1985–1990.
- [129] A. Cho, *Science* 313 (2006) 164–165.
- [130] N.V. Demarina, D.A. Grützmacher, *Appl. Phys. Lett.* 98 (2011) 192109.
- [131] F. Cavallo, R. Songmuang, O.G. Schmidt, *Appl. Phys. Lett.* 93 (2008) 143113.
- [132] M. Yu, M. Huang, D.E. Savage, M.G. Lagally, R.H. Blick, *IEEE Trans. Nanotechnol.* 10 (2011) 21–25.
- [133] S.V. Golod, V.Y. Prinz, V.I. Mashanov, A.K. Gutakovskiy, *Semicond. Sci. Technol.* 16 (2001) 181.
- [134] L. Zhang, E. Deckhardt, A. Weber, C. Schönenberger, D. Grützmacher, *Nanotechnology* 16 (2005) 655.
- [135] L. Zhang, E. Ruh, D. Grützmacher, Dong, D.J. Bell, B.J. Nelson, C. Schönenberger, *Nano Lett.* 6 (2006) 1311–1317.
- [136] L. Dai, L. Zhang, *Nanoscale* 5 (2013) 971–976.
- [137] L. Zhang, L. Dong, B.J. Nelson, *Appl. Phys. Lett.* 92 (2008) 143110.
- [138] F. Cavallo, W. Sigle, O.G. Schmidt, *J. Appl. Phys.* 103 (2008) 116103.
- [139] S.V. Golod, V.Y. Prinz, P. Wägli, L. Zhang, O. Kirfel, E. Deckhardt, F. Glaus, C. David, D. Grützmacher, *Appl. Phys. Lett.* 84 (2004) 3391–3393.
- [140] Q. Guo, M. Zhang, Z. Xue, J. Zhang, G. Wang, D. Chen, Z. Mu, G. Huang, Y. Mei, Z. Di, X. Wang, *AIP Adv.* 5 (2015) 037115.
- [141] Q. Guo, G. Wang, D. Chen, G. Li, G. Huang, M. Zhang, X. Wang, Y. Mei, Z. Di, *Appl. Phys. Lett.* 110 (2017) 112104.
- [142] Z. Mu, M. Zhang, Z. Xue, G. Sun, Q. Guo, D. Chen, G. Huang, Y. Mei, P.K. Chu, Z. Di, X. Wang, *Appl. Phys. Lett.* 106 (2015) 174102.

- [143] R. Songmuang, C. Deneke, O.G. Schmidt, *Appl. Phys. Lett.* 89 (2006) 223109.
- [144] F. Cavallo, R. Songmuang, C. Ulrich, O.G. Schmidt, *Appl. Phys. Lett.* 90 (2007) 193120.
- [145] J. Deng, H. Ji, C. Yan, J. Zhang, W. Si, S. Baunack, S. Oswald, Y. Mei, O.G. Schmidt, *Angew. Chem. Int. Ed.* 52 (2013) 2326–2330.
- [146] C. Yan, W. Xi, W. Si, J. Deng, O.G. Schmidt, *Adv. Mater.* 25 (2013) 539–544.
- [147] D. Yu, F. Liu, *Nano Lett.* 7 (2007) 3046–3050.
- [148] I.D. Barcelos, L.A.B. Marcal, C. Deneke, L.G. Moura, R.G. Lacerda, A. Malachias, *RSC Adv.* 6 (2016) 103707–103713.
- [149] Z. Tian, L. Zhang, Y. Fang, B. Xu, S. Tang, N. Hu, Z. An, Z. Chen, Y. Mei, *Adv. Mater.* 29 (2017) 1604572–n/a.
- [150] G. Huang, J. Wang, Z. Liu, D. Zhou, Z. Tian, B. Xu, L. Li, Y. Mei, *Nanoscale* 9 (2017) 18590–18596.
- [151] J. Meng, G. Wang, X. Li, X. Lu, J. Zhang, H. Yu, W. Chen, L. Du, M. Liao, J. Zhao, P. Chen, J. Zhu, X. Bai, D. Shi, G. Zhang, *Small* 12 (2016) 3770–3774.
- [152] D.Y. Hwang, K.H. Choi, J.E. Park, D.H. Suh, *Nanoscale* 9 (2017) 503–508.
- [153] L. Dai, L. Zhang, L.X. Dong, W.Z. Shen, X.B. Zhang, Z.Z. Ye, B.J. Nelson, *Nanoscale* 3 (2011) 4301–4306.
- [154] Y.L. Shen, S. Suresh, I.A. Blech, *J. Appl. Phys.* 80 (1996) 1388–1398.
- [155] Y. Mei, S. Kiravittaya, S. Harazim, O.G. Schmidt, *Mater. Sci. Eng. R* 70 (2010) 209–224.
- [156] Y. Cui, *IEEE T. Electron Dev.* 63 (2016) 3372–3384.
- [157] Z. Chen, G. Huang, I. Trase, X. Han, Y. Mei, *Phys. Rev. Appl.* 5 (2016) 017001–017033.
- [158] W.-P. Huang, H.H. Cheng, A.I. Fedorchenko, A.-B. Wang, *Appl. Phys. Lett.* 91 (2007) 053103.
- [159] G.-E. Chang, C.-O. Chang, H.H. Cheng, *J. Appl. Phys.* 111 (2012) 034314.
- [160] A.I. Fedorchenko, H.H. Cheng, G. Sun, R.A. Soref, *Appl. Phys. Lett.* 96 (2010) 113104.
- [161] Y. Zhang, M. Yu, D.E. Savage, M.G. Lagally, R.H. Blick, F. Liu, *Appl. Phys. Lett.* 96 (2010) 111904.
- [162] A.I. Fedorchenko, A.-B. Wang, V.I. Mashanov, W.-P. Huang, H.H. Cheng, *Appl. Phys. Lett.* 89 (2006) 043119.
- [163] A. Malachias, Y. Mei, R.K. Annabattula, C. Deneke, P.R. Onck, O.G. Schmidt, *ACS Nano* 2 (2008) 1715–1721.
- [164] P. Cendula, A. Malachias, C. Deneke, S. Kiravittaya, O.G. Schmidt, *Nanoscale* 6 (2014) 14326–14335.
- [165] Y. Mei, S. Kiravittaya, M. Benyoucef, D.J. Thurmer, T. Zander, C. Deneke, F. Cavallo, A. Rastelli, O.G. Schmidt, *Nano Lett.* 7 (2007) 1676–1679.
- [166] P. Cendula, S. Kiravittaya, I. Mönch, J. Schumann, O.G. Schmidt, *Nano Lett.* 11 (2011) 236–240.
- [167] V.Y. Prinz, D. Grützmacher, A. Beyer, C. David, B. Ketterer, E. Deckardt, *Nanotechnology* 12 (2001) 399.
- [168] L. Zhang, L. Dong, D.J. Bell, B.J. Nelson, C. Schönenberger, D. Grützmacher, *Microelectron. Eng.* 83 (2006) 1237–1240.
- [169] K. Seongseop, K. Wonbae, C. Maenghyo, *Jpn. J. Appl. Phys.* 50 (2011) 070208.
- [170] L. Dai, W.Z. Shen, *J. Appl. Phys.* 106 (2009) 114314.
- [171] Y. Huang, H. Chen, J. Wu, X. Feng, *Soft Matter* 10 (2014) 2559–2566.
- [172] Y. Zhang, F. Zhang, Z. Yan, Q. Ma, X. Li, Y. Huang, J.A. Rogers, *Nat. Rev. Mater.* 2 (2017) 17019.
- [173] K. Zhang, Y.H. Jung, S. Mikkael, J.-H. Seo, M. Kim, H. Mi, H. Zhou, Z. Xia, W. Zhou, S. Gong, Z. Ma, *Nat. Commun.* 8 (2017) 1782.
- [174] D.-H. Kim, J.A. Rogers, *ACS Nano* 3 (2009) 498–501.
- [175] D.-H. Kim, J. Xiao, J. Song, Y. Huang, J.A. Rogers, *Adv. Mater.* 22 (2010) 2108–2124.
- [176] W.M. Choi, J. Song, D.-Y. Khang, H. Jiang, Y.Y. Huang, J.A. Rogers, *Nano Lett.* 7 (2007) 1655–1663.
- [177] F. Cavallo, K.T. Turner, M.G. Lagally, *Adv. Funct. Mater.* 24 (2014) 1730–1737.
- [178] J. Song, H. Jiang, W.M. Choi, D.Y. Khang, Y. Huang, J.A. Rogers, *J. Appl. Phys.* 103 (2008) 014303.
- [179] C.T. Koh, Z.J. Liu, D.-Y. Khang, J. Song, C. Lu, Y. Huang, J.A. Rogers, C.G. Koh, *Appl. Phys. Lett.* 91 (2007) 133113.
- [180] H. Jiang, D.-Y. Khang, J. Song, Y. Sun, Y. Huang, J.A. Rogers, *Proc. Natl. Acad. Sci. U. S. A.* 104 (2007) 15607–15612.
- [181] H. Jiang, Y. Sun, J.A. Rogers, Y. Huang, *Appl. Phys. Lett.* 90 (2007) 133119.
- [182] Y. Sun, J.A. Rogers, *J. Mater. Chem.* 17 (2007) 832–840.
- [183] Y. Ma, K.-I. Jang, L. Wang, H.N. Jung, J.W. Kwak, Y. Xue, H. Chen, Y. Yang, D. Shi, X. Feng, J.A. Rogers, Y. Huang, *Adv. Funct. Mater.* 26 (2016) 5345–5351.
- [184] D. van den Ende, J.-D. Kamminga, A. Boersma, T. Andritsch, P.G. Steeneken, *Adv. Mater.* 25 (2013) 3438–3442.
- [185] L. Sze-Hsien, L. Gih-Keong, *Smart Mater. Struct.* 23 (2014) 125021.
- [186] E.P. Chan, K.A. Page, S.H. Im, D.L. Patton, R. Huang, C.M. Stafford, *Soft Matter* 5 (2009) 4638–4641.
- [187] S.M. Woo, C.M. Gabardo, L. Soleymani, *Anal. Chem.* 86 (2014) 12341–12347.
- [188] F. Greco, L. Ventrelli, P. Dario, B. Mazzolai, V. Mattoli, *Int. J. Hydrogen Energy* 37 (2012) 17529–17539.
- [189] S.Y. Ryu, J. Xiao, W.I. Park, K.S. Son, Y.Y. Huang, U. Paik, J.A. Rogers, *Nano Lett.* 9 (2009) 3214–3219.
- [190] M.E. McConney, N.R. Glavin, A.T. Juhl, M.H. Check, M.F. Durstock, A.A. Voevodin, T.E. Shelton, J.E. Bultman, J. Hu, M.L. Jespersen, M.K. Gupta, R.D. Naguy, J.G. Colborn, A. Haque, P.T. Hagerty, R.E. Stevenson, C. Muratore, *J. Mater. Res.* 31 (2016) 967–974.
- [191] D.-Y. Khang, J. Xiao, C. Kocbas, S. MacLaren, T. Banks, H. Jiang, Y.Y. Huang, J.A. Rogers, *Nano Lett.* 8 (2008) 124–130.
- [192] J. Xiao, H. Jiang, D.Y. Khang, J. Wu, Y. Huang, J.A. Rogers, *J. Appl. Phys.* 104 (2008) 033543.
- [193] S.M. Harazim, P. Feng, S. Sanchez, C. Deneke, Y. Mei, O.G. Schmidt, *Nanoscale Res. Lett.* 6 (2011) 215.
- [194] M. Shrestha, G.-K. Lau, *Opt. Lett.* 41 (2016) 4433–4436.
- [195] Y. Wang, T. Ma, H. Yu, H. Jiang, *Appl. Phys. Lett.* 102 (2013) 041915.
- [196] S. Yang, C. Wang, H. Sahin, H. Chen, Y. Li, S.-S. Li, A. Suslu, F.M. Peeters, Q. Liu, J. Li, S. Tongay, *Nano Lett.* 15 (2015) 1660–1666.
- [197] X. Feng, B.D. Yang, Y. Liu, Y. Wang, C. Dagdeviren, Z. Liu, A. Carlson, J. Li, Y. Huang, J.A. Rogers, *ACS Nano* 5 (2011) 3326–3332.
- [198] H.-Y. Ong, M. Shrestha, G.-K. Lau, *Appl. Phys. Lett.* 107 (2015) 132902.
- [199] T. Ma, H. Liang, G. Chen, B. Poon, H. Jiang, H. Yu, *Opt. Express* 21 (2013) 11994–12001.
- [200] J. Tang, H. Guo, M. Chen, J. Yang, D. Tsoukalas, B. Zhang, J. Liu, C. Xue, W. Zhang, *Sens. Actuators B: Chem.* 218 (2015) 145–151.
- [201] T. Ohzono, M. Shimomura, *Phys. Rev. B* 69 (2004) 132202.
- [202] S.H. Chae, W.J. Yu, J.J. Bae, D.L. Duong, D. Perello, H.Y. Jeong, Q.H. Ta, T.H. Ly, Q. A. Vu, M. Yun, X. Duan, Y.H. Lee, *Nat. Mater.* 12 (2013) 403–409.
- [203] Y. Wang, R. Yang, Z. Shi, L. Zhang, D. Shi, E. Wang, G. Zhang, *ACS Nano* 5 (2011) 3645–3650.
- [204] C.-W. Chiang, G. Haider, W.-C. Tan, Y.-R. Liou, Y.-C. Lai, R. Ravindranath, H.-T. Chang, Y.-F. Chen, *ACS Appl. Mater. Inter.* 8 (2016) 466–471.
- [205] P. Kang, M.C. Wang, P.M. Knapp, S. Nam, *Adv. Mater.* 28 (2016) 4639–4645.
- [206] S. Deng, V. Berry, *Mater. Today* 19 (2016) 197–212.
- [207] A. Castellanos-Gomez, R. Roldán, E. Cappelluti, M. Buscema, F. Guinea, H.S.J. van der Zant, G.A. Steele, *Nano Lett.* 13 (2013) 5361–5366.
- [208] W. Michael Cai, L. Juyoung, K. Pilgyu, C. Jonghyun, K. Peter, Y. Keong, N. SungWoo, *2D Mater.* 4 (2017) 022002.
- [209] Y. Zhang, Z. Yan, K. Nan, D. Xiao, Y. Liu, H. Luan, H. Fu, X. Wang, Q. Yang, J. Wang, W. Ren, H. Si, F. Liu, L. Yang, H. Li, J. Wang, X. Guo, H. Luo, L. Wang, Y. Huang, J.A. Rogers, *Proc. Natl. Acad. Sci. U. S. A.* 112 (2015) 11757–11764.
- [210] J. Rogers, Y. Huang, O.G. Schmidt, D.H. Gracias, *MRS Bull.* 41 (2016) 123–129.
- [211] Y. Liu, Z. Yan, Q. Lin, X. Guo, M. Han, K. Nan, K.-C. Hwang, Y. Huang, Y. Zhang, J. A. Rogers, *Adv. Funct. Mater.* 26 (2016) 2909–2918.
- [212] Z. Yan, F. Zhang, J. Wang, F. Liu, X. Guo, K. Nan, Q. Lin, M. Gao, D. Xiao, Y. Shi, Y. Qiu, H. Luan, J.H. Kim, Y. Wang, H. Luo, M. Han, Y. Huang, Y. Zhang, J.A. Rogers, *Adv. Funct. Mater.* 26 (2016) 2629–2639.
- [213] Z. Yan, F. Zhang, F. Liu, M. Han, D. Ou, Y. Liu, Q. Lin, X. Guo, H. Fu, Z. Xie, M. Gao, Y. Huang, J. Kim, Y. Qiu, K. Nan, J. Kim, P. Gutruf, H. Luo, A. Zhao, K.-C. Hwang, Y. Huang, Y. Zhang, J.A. Rogers, *Sci. Adv.* 2 (2016) e1601014.
- [214] Y. Shi, F. Zhang, K. Nan, X. Wang, J. Wang, Y. Zhang, Y. Zhang, H. Luan, K.-C. Hwang, Y. Huang, J.A. Rogers, Y. Zhang, *Extreme Mech. Lett.* 11 (2017) 105–110.
- [215] Z. Yan, M. Han, Y. Yang, K. Nan, H. Luan, Y. Luo, Y. Zhang, Y. Huang, J.A. Rogers, *Extreme Mech. Lett.* 11 (2017) 96–104.
- [216] X. Ning, H. Wang, X. Yu, J.A.N.T. Soares, Z. Yan, K. Nan, G. Velarde, Y. Xue, R. Sun, Q. Dong, H. Luan, C.M. Lee, A. Chempakasseril, M. Han, Y. Wang, L. Li, Y. Huang, Y. Zhang, J.A. Rogers, *Adv. Funct. Mater.* 27 (2017) 1605914–1605922.
- [217] K. Nan, H. Luan, Z. Yan, X. Ning, Y. Wang, A. Wang, J. Wang, M. Han, M. Chang, K. Li, Y. Zhang, W. Huang, Y. Xue, Y. Huang, Y. Zhang, J.A. Rogers, *Adv. Funct. Mater.* 27 (2017) 1604281.
- [218] H. Fu, K. Nan, P. Froeter, W. Huang, Y. Liu, Y. Wang, J. Wang, Z. Yan, H. Luan, X. Guo, Y. Zhang, C. Jiang, L. Li, A.C. Dunn, X. Li, Y. Huang, Y. Zhang, J.A. Rogers, *Small* 13 (2017) 1700151.
- [219] Z. Song, C. Lv, M. Liang, V. Sanphuang, K. Wu, B. Chen, Z. Zhao, J. Bai, X. Wang, J. L. Volakis, L. Wang, X. He, Y. Yao, S. Tongay, H. Jiang, *Small* 12 (2016) 5401–5406.
- [220] X. Guo, H. Li, B. Yeop Ahn, E.B. Duoss, K.J. Hsia, J.A. Lewis, R.G. Nuzzo, *Proc. Natl. Acad. Sci. U. S. A.* 106 (2009) 20149–20154.
- [221] D. Grimm, R.B. Wilson, B. Teshome, S. Gorantla, M.H. Rummeli, T. Bublath, E. Zallo, G. Li, D.G. Cahill, O.G. Schmidt, *Nano Lett.* 14 (2014) 2387–2393.
- [222] G. Huang, S. Kiravittaya, V.A.B. Quiñones, M. Benyoucef, A. Rastelli, Y. Mei, O. G. Schmidt, *Appl. Phys. Lett.* 94 (2009) 141901.
- [223] T. Zander, C. Deneke, A. Malachias, C. Mickel, T.H. Metzger, O.G. Schmidt, *Appl. Phys. Lett.* 94 (2009) 053102.
- [224] D.-W. Oh, S. Kim, J.A. Rogers, D.G. Cahill, S. Sinha, *Adv. Mater.* 23 (2011) 5028–5033.
- [225] R. Songmuang, A. Rastelli, S. Mendach, O.G. Schmidt, *Appl. Phys. Lett.* 90 (2007) 091905.
- [226] J. Wang, T. Zhan, G. Huang, P.K. Chu, Y. Mei, *Laser Photonics Rev.* 8 (2014) 521–547.
- [227] X. Li, *Adv. Opt. Photonics* 3 (2011) 366–387.
- [228] S. Tang, Y. Fang, Z. Liu, L. Zhou, Y. Mei, *Lab Chip* 16 (2016) 182–187.
- [229] D. Han, Y. Fang, D. Du, G. Huang, T. Qiu, Y. Mei, *Nanoscale* 8 (2016) 9141–9145.
- [230] J. Zhang, J. Li, S. Tang, Y. Fang, J. Wang, G. Huang, R. Liu, L. Zheng, X. Cui, Y. Mei, *Sci. Rep.* 5 (2015) 15012.
- [231] J. Wang, E. Song, C. Yang, L. Zheng, Y. Mei, *Thin Solid Films* 627 (2017) 77–81.
- [232] G. Huang, Y. Mei, *J. Meter. Chem. C* 5 (2017) 2758–2770.
- [233] Y. Li, Y. Fang, J. Wang, L. Wang, S. Tang, C. Jiang, L. Zheng, Y. Mei, *Lab Chip* 16 (2016) 4406–4414.
- [234] X. Lin, Y. Fang, L. Zhu, J. Zhang, G. Huang, J. Wang, Y. Mei, *Adv. Opt. Mater.* 4 (2016) 936–942.
- [235] Z. Suo, E.Y. Ma, H. Gleskova, S. Wagner, *Appl. Phys. Lett.* 74 (1999) 1177–1179.
- [236] Z.Y. Huang, W. Hong, Z. Suo, *J. Mech. Phys. Solids* 53 (2005) 2101–2118.
- [237] C. Deneke, A. Malachias, S. Kiravittaya, M. Benyoucef, T.H. Metzger, O.G. Schmidt, *Appl. Phys. Lett.* 96 (2010) 143101.
- [238] A. Bernardi, A.R. Goñi, M.I. Alonso, F. Alsina, H. Scheel, P.O. Vaccaro, N. Saito, *J. Appl. Phys.* 99 (2006) 063512.

- [239] A. Malachias, C. Deneke, B. Krause, C. Mocuta, S. Kiravittaya, T.H. Metzger, O.G. Schmidt, *Phys. Rev. B* 79 (2009) 035301.
- [240] H. Jiang, Y. Sun, J.A. Rogers, Y. Huang, *Int. J. Solids Struct.* 45 (2008) 2014–2023.
- [241] J. Moon, E. Kim, S.K. Park, K. Lee, J.-W. Shin, D.-H. Cho, J. Lee, C.W. Joo, N.S. Cho, J.-H. Han, B.-G. Yu, S. Yoo, J.-I. Lee, *Org. Electron.* 26 (2015) 273–278.
- [242] X. Chen, B. Jia, Y. Zhang, M. Gu, *Light Sci. Appl.* 2 (2013) e92.
- [243] J.B. Kim, P. Kim, N.C. Pegard, S.J. Oh, C.R. Kagan, J.W. Fleischer, H.A. Stone, Y.-L. Loo, *Nat. Photonics* 6 (2012) 327–332.
- [244] A. Madani, S.M. Harazim, V.A. Bolaños Quiñones, M. Kleinert, A. Finn, E.S. Ghareh Naz, L. Ma, O.G. Schmidt, *Opt. Lett.* 42 (2017) 486–489.
- [245] S.M. Harazim, V.A. Bolaños Quiñones, S. Kiravittaya, S. Sanchez, O.G. Schmidt, *Lab Chip* 12 (2012) 2649–2655.
- [246] E.J. Smith, W. Xi, D. Makarov, I. Monch, S. Harazim, V.A. Bolaños Quiñones, C. K. Schmidt, Y. Mei, S. Sanchez, O.G. Schmidt, *Lab Chip* 12 (2012) 1917–1931.
- [247] A. Bernardi, S. Kiravittaya, A. Rastelli, R. Songmuang, D.J. Thurmer, M. Benyoucef, O.G. Schmidt, *Appl. Phys. Lett.* 93 (2008) 094106.
- [248] G. Huang, V.A. Bolaños Quiñones, F. Ding, S. Kiravittaya, Y. Mei, O.G. Schmidt, *ACS Nano* 4 (2010) 3123–3130.
- [249] V.A. Bolaños Quiñones, G. Huang, J.D. Plumhof, S. Kiravittaya, A. Rastelli, Y. Mei, O.G. Schmidt, *Opt. Lett.* 34 (2009) 2345–2347.
- [250] B. Xu, B. Zhang, L. Wang, G. Huang, Y. Mei, *Adv. Funct. Mater.* (2018), doi: <http://dx.doi.org/10.1002/adfm.201705872>.
- [251] Y. Mei, A.A. Solovev, S. Sanchez, O.G. Schmidt, *Chem. Soc. Rev.* 40 (2011) 2109–2119.
- [252] J. Li, B. Esteban-Fernández, W. de Ávila, L. Gao, J. Zhang, J. Wang, *Sci. Robot.* 2 (2017) eaam6431.
- [253] A.A. Solovev, Y. Mei, E. Bermúdez Ureña, G. Huang, O.G. Schmidt, *Small* 5 (2009) 1688–1692.
- [254] S. Sánchez, L. Soler, J. Katuri, *Angew. Chem. Int. Ed.* 54 (2015) 1414–1444.
- [255] L. Zhang, J.J. Abbott, L. Dong, B.E. Kratochvil, D. Bell, B.J. Nelson, *Appl. Phys. Lett.* 94 (2009) 064107.
- [256] L. Zhang, J.J. Abbott, L. Dong, K.E. Peyer, B.E. Kratochvil, H. Zhang, C. Bergeles, B.J. Nelson, *Nano Lett.* 9 (2009) 3663–3667.
- [257] J. Li, W. Liu, J. Wang, I. Rozen, S. He, C. Chen, H.G. Kim, H.-J. Lee, H.-B.-R. Lee, S.-H. Kwon, T. Li, L. Li, J. Wang, Y. Mei, *Adv. Funct. Mater.* 27 (2017) 1700598.
- [258] A.A. Solovev, W. Xi, D.H. Gracias, S.M. Harazim, C. Deneke, S. Sanchez, O.G. Schmidt, *ACS Nano* 6 (2012) 1751–1756.
- [259] W. Gao, S. Sattayasamitsathit, J. Orozco, J. Wang, *J. Am. Chem. Soc.* 133 (2011) 11862–11864.
- [260] D. Vilela, J. Parmar, Y. Zeng, Y. Zhao, S. Sánchez, *Nano Lett.* 16 (2016) 2860–2866.
- [261] S.M. Harazim, W. Xi, C.K. Schmidt, S. Sanchez, O.G. Schmidt, *J. Mater. Chem.* 22 (2012) 2878–2884.
- [262] S.E. Létant, B.R. Hart, A.W. van Buuren, L.J. Terminello, *Nat. Mater.* 2 (2003) 391.
- [263] S.-H. Wu, C.-Y. Mou, H.-P. Lin, *Chem. Soc. Rev.* 42 (2013) 3862–3875.
- [264] D. Vilela, A.C. Hortelao, R. Balderas-Xicohtencatl, M. Hirscher, K. Hahn, X. Ma, S. Sanchez, *Nanoscale* 9 (2017) 13990–13997.
- [265] L. Yin, A.B. Farimani, K. Min, N. Vishal, J. Lam, Y.K. Lee, N.R. Aluru, J.A. Rogers, *Adv. Mater.* 27 (2015) 1857–1864.
- [266] S.-K. Kang, G. Park, K. Kim, S.-W. Hwang, H. Cheng, J. Shin, S. Chung, M. Kim, L. Yin, J.C. Lee, K.-M. Lee, J.A. Rogers, *ACS Appl. Mater. Inter.* 7 (2015) 9297–9305.
- [267] G. Huang, Y. Mei, D.J. Thurmer, E. Coric, O.G. Schmidt, *Lab Chip* 9 (2009) 263–268.
- [268] M. Yu, Y. Huang, J. Ballweg, H. Shin, M. Huang, D.E. Savage, M.G. Lagally, E.W. Dent, R.H. Blick, J.C. Williams, *ACS Nano* 5 (2011) 2447–2457.
- [269] F. Cavallo, Y. Huang, E.W. Dent, J.C. Williams, M.G. Lagally, *ACS Nano* 8 (2014) 12219–12227.
- [270] B. Xu, Y. Mei, *Sci. Bull.* 62 (2017) 525–527.
- [271] D.W. Huttmacher, *Nat. Mater.* 9 (2010) 90–93.
- [272] K.A. Fitzgerald, M. Malhotra, C.M. Curtin, F.J.O. Brien, C.M.O. Driscoll, *J. Controlled Release* 215 (2015) 39–54.
- [273] J.-H. Seo, K. Zhang, M. Kim, D. Zhao, H. Yang, W. Zhou, Z. Ma, *Adv. Opt. Mater.* 4 (2016) 120–125.
- [274] G. Li, Q. Guo, Y. Fang, S. Tang, M. Liu, G. Huang, Y. Mei, *Phys. Status Solidi A* 214 (2017) 1700295.
- [275] E. Song, Q. Guo, G. Huang, B. Jia, Y. Mei, *ACS Appl. Mater. Inter.* 9 (2017) 12171–12175.
- [276] J. Yoon, A.J. Baca, S.-I. Park, P. Elvikis, J.B. Geddes, L. Li, R.H. Kim, J. Xiao, S. Wang, T.-H. Kim, M.J. Motala, B.Y. Ahn, E.B. Duoss, J.A. Lewis, R.G. Nuzzo, P.M. Ferreira, Y. Huang, A. Rockett, J.A. Rogers, *Nat. Mater.* 7 (2008) 907–915.
- [277] H. Yang, D. Zhao, S. Chuwongin, J.-H. Seo, W. Yang, Y. Shuai, J. Berggren, M. Hammar, Z. Ma, W. Zhou, *Nat. Photonics* 6 (2012) 615–620.
- [278] K.R. Catchpole, S. Pillai, *J. Lumin.* 121 (2006) 315–318.
- [279] Z. Liu, A. Masuda, T. Nagai, T. Miyazaki, M. Takano, M. Takano, H. Yoshigahara, K. Sakai, K. Asai, M. Kondo, *Sol. Energy Mater. Sol. Cells* 91 (2007) 1805–1810.
- [280] H. Wang, H. Zhen, S. Li, Y. Jing, G. Huang, Y. Mei, W. Lu, *Sci. Adv.* 2 (2016) e1600027.
- [281] H. Wang, S. Li, H. Zhen, X. Nie, G. Huang, Y. Mei, W. Lu, *J. Semicond.* 38 (2017) 054006.
- [282] F. Li, Z. Mi, *Opt. Express* 17 (2009) 19933–19939.
- [283] M.H.T. Dastjerdi, M. Djavid, Z. Mi, *Appl. Phys. Lett.* 106 (2015) 021114.
- [284] D. Grimm, C.C. Bof Bufon, C. Deneke, P. Atkinson, D.J. Thurmer, F. Schäffel, S. Gorantla, A. Bachmatiuk, O.G. Schmidt, *Nano Lett.* 13 (2013) 213–218.
- [285] W. Huang, X. Yu, P. Froeter, R. Xu, P. Ferreira, X. Li, *Nano Lett.* 12 (2012) 6283–6288.
- [286] X. Yu, W. Huang, M. Li, T.M. Comberiate, S. Gong, J.E. Schutt-Aine, X. Li, *Sci. Rep.* 5 (2015) 9661.
- [287] A. Madani, M. Kleinert, D. Stolerek, L. Zimmermann, L. Ma, O.G. Schmidt, *Opt. Lett.* 40 (2015) 3826–3829.
- [288] X. Yu, E. Arbabi, L.L. Goddard, X. Li, X. Chen, *Appl. Phys. Lett.* 107 (2015) 031102.
- [289] X. Su, Q. Wu, J. Li, X. Xiao, A. Lott, W. Lu, B.W. Sheldon, J. Wu, *Adv. Energy Mater.* 4 (2014) 1300882.
- [290] Y. Liu, S. Zhang, T. Zhu, *ChemElectroChem* 1 (2014) 706–713.
- [291] X.H. Liu, Y. Liu, A. Kushima, S. Zhang, T. Zhu, J. Li, J.Y. Huang, *Adv. Energy Mater.* 2 (2012) 722–741.
- [292] X. Wang, F. Fan, J. Wang, H. Wang, S. Tao, A. Yang, Y. Liu, H. Beng Chew, S.X. Mao, T. Zhu, S. Xia, *Nat. Commun.* 6 (2015) 8417.
- [293] Z. Zeng, N. Liu, Q. Zeng, S.W. Lee, W.L. Mao, Y. Cui, *Nano Energy* 22 (2016) 105–110.
- [294] S.W. Lee, H.-W. Lee, I. Ryu, W.D. Nix, H. Gao, Y. Cui, *Nat. Commun.* 6 (2015) 7533.
- [295] S.W. Lee, M.T. McDowell, L.A. Berla, W.D. Nix, Y. Cui, *Proc. Natl. Acad. Sci. U. S. A.* 109 (2012) 4080–4085.
- [296] X. Wang, Y. Chen, O.G. Schmidt, C. Yan, *Chem. Soc. Rev.* 45 (2016) 1308–1330.
- [297] J. Deng, H. Ji, C. Yan, J. Zhang, W. Si, S. Baunack, S. Oswald, Y. Mei, O.G. Schmidt, *Angew. Chem.* 125 (2013) 2382–2386.
- [298] X. Liu, J. Zhang, W. Si, L. Xi, B. Eichler, C. Yan, O.G. Schmidt, *ACS Nano* 9 (2015) 1198–1205.
- [299] C.C. Bof Bufon, J.D. Cojal González, D.J. Thurmer, D. Grimm, M. Bauer, O.G. Schmidt, *Nano Lett.* 10 (2010) 2506–2510.
- [300] F. Variola, F. Vetrone, L. Richert, P. Jedrzejowski, J.-H. Yi, S. Zalzal, S. Clair, A. Sarkissian, D.F. Perepichka, J.D. Wuest, F. Rosei, A. Nanci, *Small* 5 (2009) 996–1006.
- [301] C.K. Chan, X.F. Zhang, Y. Cui, *Nano Lett.* 8 (2008) 307–309.
- [302] M.-H. Park, Y. Cho, K. Kim, J. Kim, M. Liu, J. Cho, *Angew. Chem. Int. Ed.* 50 (2011) 9647–9650.
- [303] D.-J. Xue, S. Xin, Y. Yan, K.-C. Jiang, Y.-X. Yin, Y.-G. Guo, L.-J. Wan, *J. Am. Chem. Soc.* 134 (2012) 2512–2515.
- [304] L. Zhang, J. Deng, L. Liu, W. Si, S. Oswald, L. Xi, M. Kundu, G. Ma, T. Gemming, S. Baunack, F. Ding, C. Yan, O.G. Schmidt, *Adv. Mater.* 26 (2014) 4527–4532.
- [305] Y. Chen, C. Yan, O.G. Schmidt, *Adv. Energy Mater.* 3 (2013) 1269–1274.
- [306] E. Menard, R.G. Nuzzo, J.A. Rogers, *Appl. Phys. Lett.* 86 (2005) 093507.
- [307] L. Sun, G. Qin, J.-H. Seo, G.K. Celler, W. Zhou, Z. Ma, *Small* 6 (2010) 2553–2557.
- [308] J.-H. Seo, K. Zhang, M. Kim, W. Zhou, Z. Ma, *npj Flexible Electron.* 1 (2017) 1.
- [309] S. Dhar, D.M. Miller, N.M. Jokerst, *Opt. Express* 22 (2014) 5052–5059.
- [310] M. Dang, H.-C. Yuan, Z. Ma, J. Ma, G. Qin, *Appl. Phys. Lett.* 110 (2017) 253104.
- [311] Z. Xia, H. Song, M. Kim, M. Zhou, T.-H. Chang, D. Liu, X. Yin, K. Xiong, H. Mi, X. Wang, F. Xia, Z. Yu, Z. Ma, Q. Gan, *Sci. Adv.* 3 (2017) e1602783.
- [312] M. Kim, S.-C. Liu, T.J. Kim, J. Lee, J.-H. Seo, W. Zhou, Z. Ma, *Opt. Express* 24 (2016) 16894–16903.
- [313] X. Xu, H. Subbaraman, S. Chakravarty, A. Hosseini, J. Covey, Y. Yu, D. Kwong, Y. Zhang, W.-C. Lai, Y. Zou, N. Lu, R.T. Chen, *ACS Nano* 8 (2014) 12265–12271.
- [314] X. Xu, H. Subbaraman, A. Hosseini, C.-Y. Lin, D. Kwong, R.T. Chen, *Opt. Lett.* 37 (2012) 1020–1022.
- [315] Y. Chen, M. Li, *Opt. Lett.* 39 (2014) 3449–3452.
- [316] J. Hu, L. Li, H. Lin, P. Zhang, W. Zhou, Z. Ma, *Opt. Mater. Express* 3 (2013) 1313–1331.
- [317] L. Fan, L.T. Varghese, Y. Xuan, J. Wang, B. Niu, M. Qi, *Opt. Express* 20 (2012) 20564–20575.
- [318] Y. Chen, H. Li, M. Li, *Sci. Rep.* 2 (2012) 622.
- [319] W. Zhou, D. Zhao, Y.-C. Shuai, H. Yang, S. Chuwongin, A. Chadha, J.-H. Seo, K.X. Wang, V. Liu, Z. Ma, S. Fan, *Prog. Quant. Electron.* 38 (2014) 1–74.
- [320] M. Kim, J.-H. Seo, Z. Yu, W. Zhou, Z. Ma, *Appl. Phys. Lett.* 109 (2016) 051105.
- [321] G. Qin, K. Zuo, J.-H. Seo, Y. Xu, H.-C. Yuan, H. Liu, Z. Huang, J. Ma, Z. Ma, *Appl. Phys. Lett.* 106 (2015) 043504.
- [322] Z. Xia, K. Zhang, D. Liu, M. Zhou, T.-J. Kim, H. Zhang, M. Xue, J. Park, M. Morea, J. H. Ryu, T.-H. Chang, J. Kim, S. Gong, T.I. Kamins, Z. Yu, Z. Wang, J.S. Harris, Z. Ma, *Appl. Phys. Lett.* 111 (2017) 081109.
- [323] G. Qin, T. Cai, H.-C. Yuan, J.-H. Seo, J. Ma, Z. Ma, *Appl. Phys. Lett.* 104 (2014) 163501.
- [324] Y.H. Jung, H. Zhang, S.J. Cho, Z. Ma, *IEEE Trans. Electron. Dev.* 64 (2017) 1881–1893.
- [325] D.-H. Kim, J.-H. Ahn, W.M. Choi, H.-S. Kim, T.-H. Kim, J. Song, Y.Y. Huang, Z. Liu, C. Lu, J.A. Rogers, *Science* 320 (2008) 507–511.
- [326] D.-H. Kim, J. Song, W.M. Choi, H.-S. Kim, R.-H. Kim, Z. Liu, Y.Y. Huang, K.-C. Hwang, Y.-w. Zhang, J.A. Rogers, *Proc. Natl. Acad. Sci. U. S. A.* 105 (2008) 18675–18680.
- [327] H.C. Ko, G. Shin, S. Wang, M.P. Stoykovich, J.W. Lee, D.-H. Kim, J.S. Ha, Y. Huang, K.-C. Hwang, J.A. Rogers, *Small* 5 (2009) 2703–2709.
- [328] T. Sekitani, S. Iba, Y. Kato, Y. Noguchi, T. Someya, T. Sakurai, *Appl. Phys. Lett.* 87 (2005) 173502.
- [329] H.C. Ko, M.P. Stoykovich, J. Song, V. Malyarchuk, W.M. Choi, C.-J. Yu, J.B. Geddes, J. Xiao, S. Wang, Y. Huang, J.A. Rogers, *Nature* 454 (2008) 748–753.
- [330] J. Viventi, D.-H. Kim, J.D. Moss, Y.-S. Kim, J.A. Blanco, N. Annetta, A. Hicks, J. Xiao, Y. Huang, D.J. Callans, J.A. Rogers, B. Litt, *Sci. Transl. Med.* 2 (2010) 24ra22.
- [331] K.J. Yu, D. Kuzum, S.-W. Hwang, B.H. Kim, H. Juul, N.H. Kim, S.M. Won, K. Chiang, M. Trumpis, A.G. Richardson, H. Cheng, H. Fang, M. Thompson, H. Bink, D. Talos, K.J. Seo, H.N. Lee, S.-K. Kang, J.-H. Kim, J.Y. Lee, Y. Huang, F.E.

- Jensen, M.A. Dichter, T.H. Lucas, J. Viventi, B. Litt, J.A. Rogers, *Nat. Mater.* 15 (2016) 782–791.
- [332] S.-K. Kang, R.K.J. Murphy, S.-W. Hwang, S.M. Lee, D.V. Harburg, N.A. Krueger, J. Shin, P. Gamble, H. Cheng, S. Yu, Z. Liu, J.G. McCall, M. Stephen, H. Ying, J. Kim, G. Park, R.C. Webb, C.H. Lee, S. Chung, D.S. Wie, A.D. Gujar, B. Vemulapalli, A.H. Kim, K.-M. Lee, J. Cheng, Y. Huang, S.H. Lee, P.V. Braun, W.Z. Ray, J.A. Rogers, *Nature* 530 (2016) 71–76.
- [333] W. Gao, S. Emaminejad, H.Y.Y. Nyein, S. Challa, K. Chen, A. Peck, H.M. Fahad, H. Ota, H. Shiraki, D. Kiriya, D.-H. Lien, G.A. Brooks, R.W. Davis, A. Javey, *Nature* 529 (2016) 509–514.
- [334] D.-H. Kim, N. Lu, R. Ma, Y.-S. Kim, R.-H. Kim, S. Wang, J. Wu, S.M. Won, H. Tao, A. Islam, K.J. Yu, T.-i. Kim, R. Chowdhury, M. Ying, L. Xu, M. Li, H.-J. Chung, H. Keum, M. McCormick, P. Liu, Y.-W. Zhang, F.G. Omenetto, Y. Huang, T. Coleman, J.A. Rogers, *Science* 333 (2011) 838–843.
- [335] D.-H. Kim, J. Viventi, J.J. Amsden, J. Xiao, L. Vigeland, Y.-S. Kim, J.A. Blanco, B. Panilaitis, E.S. Frechette, D. Contreras, D.L. Kaplan, F.G. Omenetto, Y. Huang, K.-C. Hwang, M.R. Zakin, B. Litt, J.A. Rogers, *Nat. Mater.* 9 (2010) 511–517.
- [336] S.W. Hwang, H. Tao, D.H. Kim, H. Cheng, J.K. Song, E. Rill, M.A. Brenckle, B. Panilaitis, S.M. Won, Y.S. Kim, Y.M. Song, K.J. Yu, A. Ameen, R. Li, Y. Su, M. Yang, D.L. Kaplan, M.R. Zakin, M.J. Slepian, Y. Huang, F.G. Omenetto, J.A. Rogers, *Science* 337 (2012) 1640–1644.
- [337] P. Vogt, P. De Padova, C. Quaresima, J. Avila, E. Frantzeskakis, M.C. Asensio, A. Resta, B. Ealet, G. Le Lay, *Phys. Rev. Lett.* 108 (2012) 155501.
- [338] M.E. Dávila, L. Xian, S. Cahangirov, A. Rubio, G.L. Lay, *New J. Phys.* 16 (2014) 095002.
- [339] J.-H. Seo, T.-Y. Oh, J. Park, W. Zhou, B.-K. Ju, Z. Ma, *Adv. Funct. Mater.* 23 (2013) 3398–3403.
- [340] F. Cavallo, R. Rojas Delgado, M.M. Kelly, J.R. Sánchez Pérez, D.P. Schroeder, H.G. Xing, M.A. Eriksson, M.G. Lagally, *ACS Nano* 8 (2014) 10237–10245.
- [341] L. Wang, J. Jie, Z. Shao, Q. Zhang, X. Zhang, Y. Wang, Z. Sun, S.-T. Lee, *Adv. Funct. Mater.* 25 (2015) 2910–2919.
- [342] C.-C. Chen, M. Aykol, C.-C. Chang, A.F.J. Levi, S.B. Cronin, *Nano Lett.* 11 (2011) 1863–1867.
- [343] Y.-C. Lin, I. Bilgin, T. Ahmed, R. Chen, D. Pete, S. Kar, J.-X. Zhu, G. Gupta, A. Mohite, J. Yoo, *Nanoscale* 8 (2016) 18675–18681.
- [344] Q.H. Wang, K. Kalantar-Zadeh, A. Kis, J.N. Coleman, M.S. Strano, *Nat. Nanotechnol.* 7 (2012) 699–712.
- [345] X. Wang, Z. Cheng, K. Xu, H.K. Tsang, J.-B. Xu, *Nat. Photonics* 7 (2013) 888–891.
- [346] G. Wang, M. Zhang, Y. Zhu, G. Ding, D. Jiang, Q. Guo, S. Liu, X. Xie, P.K. Chu, Z. Di, X. Wang, *Sci. Rep.* 3 (2013) 2465.
- [347] S. Mikael, J.-H. Seo, D.-W. Park, M. Kim, H. Mi, A. Javadi, S. Gong, Z. Ma, *Extreme Mech. Lett.* 11 (2017) 77–83.